Investigating Periodic Density Structures in the Solar Wind's Elemental and Ionic Composition

by

Irena Gershkovich

A dissertation submitted in partial fulfillment
of the requirements for the degree of
Doctor of Philosophy
(Physics)
in The University of Michigan
2022

Doctoral Committee:

Professor Susan T. Lepri, Co-Chair
Professor Keith Riles, Co-Chair
Professor Enrico Landi
Professor James Liu
Research Astrophysicist Nicholeen Viall, NASA Goddard Space Flight Center

Irena Gershkovich

igershko@umich.edu

ORCID iD: 0000-0001-5600-9985

This effort is dedicated to those who provide dissent when it is needed most.

ACKNOWLEDGEMENTS

I would first like to thank my advisors: Susan Lepri and Nicholeen Viall. They have been instrumental to this work and the collaboration has been an excellent one for me. Simone Di Matteo has also been a tremendous asset. He has provided me with tools that will be valuable beyond this experience, enthusiastic feedback and support. Larry Kepko was crucial to the development of my first paper and I would like to thank him for his insightful feedback.

Thanks to Ryan Dewey for providing me with the early Solar Orbiter data and for always being willing to answer questions. I would also like to acknowledge some of the people that I worked with early on during this experience. Jim Raines has been welcoming and incredibly generous with this time. Ryan Barnhart is someone who always goes above and beyond the task at hand. Jason Gilbert inspired me with his extensive knowledge of space instrumentation and plasma measurement techniques.

Thank you to the staff of both the Physics as well as the Climate and Space Sciences and Engineering Departments. Thank you to my previous advisor and group for opening doors for me and changing how I see the world.

Thank you to NASA for funding this research. This work was supported by the NASA competed Heliophysics Internal Scientist Funding Model under the award number 80NSSC20K1063.

I'd like to thank my committee for their service and valuable feedback. Finally, I would like to thank my partner, who has always been there for me.

TABLE OF CONTENTS

CHAPTER

LIST OF FIGURES

Figure

LIST OF TABLES

Table

LIST OF ABBREVIATIONS

ACE Advanced Composition Explorer

AR Active Region

AU Astronomical Units

BPL Bending Power Law

CH Coronal Hole

ESA Electro-Static-Analyzer

FIP First Ionization Potential

FOV Field of View

HCS Heliospheric Current Sheet

HSO Heliophysics System Observatory

L1 Lagrange point 1

MCP Micro-Channel Plate

PSD Power Spectral Density

QS Quiet Sun

RTN Radial Tangential Normal

SIR Stream Interaction Region

SO Solar Orbiter

SSD Solid-State-Detector

SWICS Solar Wind Ion Composition Spectrometer

TOF Time-of-Flight

ABSTRACT

Mesoscale periodic density structures observed in the solar wind plasma serve as an important diagnostic tool for constraining the processes that govern the formation and release of the solar wind. The aim of this thesis is to investigate periodic density structures in the solar wind's elemental composition and charge states in order to understand how solar wind properties measured *in situ* can be linked to their source regions on the Sun and to the mechanisms that produced them. Previously, periodic density structures have been primarily observed *in situ* and in remote data as fluctuations in proton and electron density. Only two events of this type have been reported for the elemental and charge state composition (*Viall et al.*, 2009a; *Kepko et al.*, 2016). Composition measurements are particularly important in gaining an understanding of the origin of the solar wind, as the composition is frozen into the plasma in the Sun's atmosphere and does not evolve during advection. This work investigates the detailed evolution of four events containing periodic structures and presents the results of the first statistical study analyzing the periodic structures detected in the solar wind heavy ion abundances and charge states over the course of 14 years. We use a spectral analysis method specifically designed to extract periodic signals from astrophysical time series and apply it to the Advanced Composition Explorer's Solar Wind Ion Composition Spectrometer (ACE/SWICS) 12-minute native resolution data set, which is an extended data product that is at the temporal resolution limits of the instrument. Additionally, this work presents the results of characterizing preliminary data coming from the Solar Orbiter Heavy Ion Sensor (SO-HIS), a new *in situ* ion mass spectrometer, just coming online, that will measure heavy ions in the solar wind plasma at an unprecedented temporal resolution, and for the first time, observe the solar wind plasma within the inner heliosphere, at distances as close as 0.28 AU to the Sun. We find that periodic structures are present at statistically significant levels and that some periodicities occur more often than others, thus demonstrating the presence of a characteristic scale. The techniques presented here are relevant to future, higher-resolution studies of SO-HIS data throughout the instrument's primary and extended mission.

CHAPTER I

Introduction

In this work, we investigate the relationship between periodic density structures observed *in situ* in the composition of the solar wind and the source regions on the Sun from which these structures likely originate. We also examine the possible mechanisms involved in their release. This chapter provides relevant background material for understanding the methods, results and conclusions presented in later chapters. We first review the structure and properties of the Sun, then discuss the heliosphere and the nature of the solar wind. We introduce important proxies that allow us to link *in situ* observations of the composition of the solar wind to their source regions on the Sun: First Ionization Potential (FIP) and charge state abundances. These concepts are critical to the work as the FIP and charge state abundances of the solar wind are determined in the solar atmosphere and do not evolve. Different types of source regions on the Sun, introduced in this chapter, are known to differ in their FIP and charge state abundance levels. Thus, these properties are indicative of the type of source region on the Sun that produced an observed parcel of solar wind and the fundamental physical processes responsible. We discuss periodic density structures previously observed in the solar wind, provide an overview of the instrumentation and spectral analysis methods used to detect these structures and introduce a model for the mechanism of their release. Finally, we provide an overview of the thesis and give the motivation for each chapter.

1.1 The Sun

1.1.1 The Sun: Interior Structure and Energy

The Sun is a G-type (spectral type G-V) main-sequence star that contains approximately 99.85% of the solar system's mass. Every second, the Sun fuses 600 million tons of hydrogen into helium via the proton-proton chain fusion reaction, fusing 4 protons (hydrogen nuclei) to form one alpha particle: two protons and two neutrons bound together to form a helium nucleus. The Sun's core, a region extending from the center of the Sun to $\sim 0.25\ R_\odot$ (solar radii), produces the vast majority of the Sun's heat through fusion. The rest of the Sun is heated by the transfer of this heat through its successive layers, depicted in Figure 1.1. The radiative zone is adjacent to the core and extends out to $\sim 0.7\ R_\odot$. The energy produced in the core is transferred via radiation through this zone and then via convection through the convection zone in the region between ~ 0.7 and $1\ R_\odot$. The energy eventually reaches the photosphere and escapes as sunlight and the kinetic energy of particles. The light takes approximately 8 minutes to reach the Earth and provides almost all of the Earth's energy input.

The Sun is composed of a gaseous plasma and undergoes differential rotation that varies as a function of latitude. The rate of rotation is fastest at the equator and decreases towards the poles, with an average rotation period of approximately 28 days.

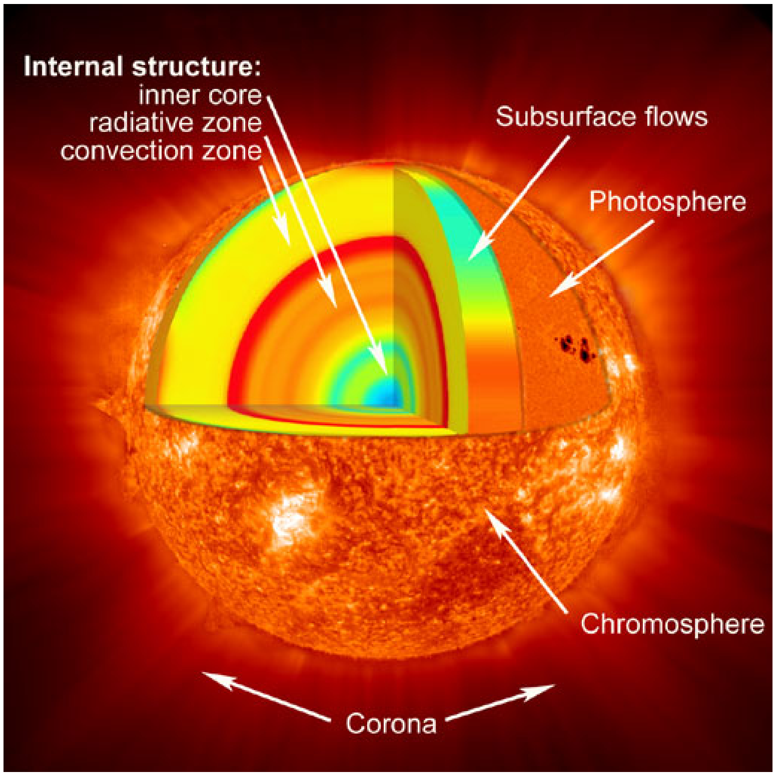

Figure 1.1: Anatomy of the Sun's interior and atmosphere. Graphic credited to NASA.

1.1.2 The Solar Atmosphere

The atmosphere of the Sun begins at the photosphere, which is the optical layer of the Sun from which photons escape. This layer is followed by a thin transition layer, then by the chromosphere and ends at the corona. The optical surface of the Sun is about 6,000 degrees Fahrenheit, but its outer atmosphere, the corona, is more than three orders of magnitude hotter (hotter than 1 MK). The corona is highly structured at many different scales and has been observed for thousands of years during total solar eclipses, during which the moon completely blocks the photosphere making the structure of the corona visible, as shown in Figure 1.2 for the 20 March 2015 eclipse observed from Svalbard, Norway (*Viall et al.*, 2020). It is interesting to note that it was only in the last centuries that we've realized that the corona belongs to the Sun and not to the Moon.

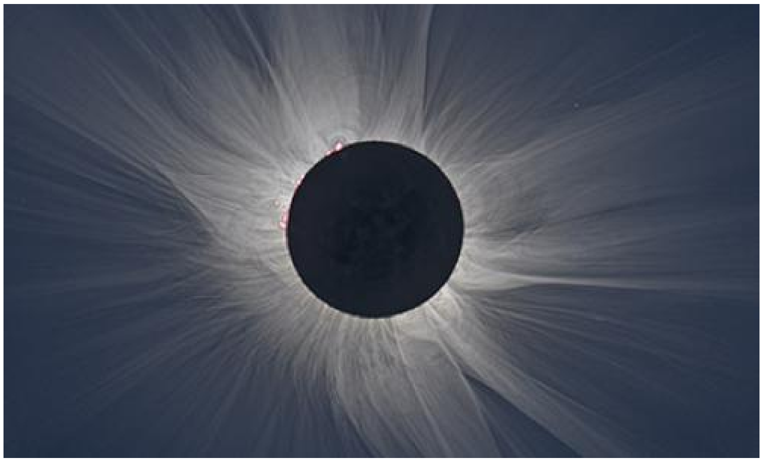

Figure 1.2: Total solar eclipse viewed in white light from Earth. Photo credited to S. Habbal, M. Druckmüller and P. Aniol.

The structures in the solar atmosphere can be broadly categorized as: Active Region (AR), Quiet Sun (QS) regions and Coronal Hole (CH) regions *Viall and Borovsky* (2020). Coronal holes are primarily open magnetic field regions on the Sun where the plasma can enter the solar wind directly from the chromosphere. These regions are determined by remote measurements, with AR regions being the hottest and densest, associated with the strongest magnetic field concentrations, producing the highest EUV and X-ray emissions, and CH regions being the coolest and dimmest. QS regions fall somewhere in between in both density and temperature. The temperature, density and emission properties of these regions have been reported and reviewed in numerous previous publications (*Viall and Borovsky*, 2020; *Viall et al.*, 2021a; *Rouillard et al.*, 2021; *Peres and Vaiana*, 1990). Figure 1.3 shows a conceptual diagram of these regions. The lines emanating from the Sun represent magnetic fields and their polarities are marked on the Sun's surface. These three regions can also be differentiated by their ion and elemental composition as summarized in Section 1.3 (*Laming*, 2015; *Rouillard et al.*, 2021). CH plasma only exhibits a slight enhancement of elements with low first ionization potential (FIP) relative to those elements with higher FIP. QS regions exhibit a higher enhancement and AR regions exhibit the most pronounced relative enhancement of low-FIP elements. We use these known properties to reason about where and how a particular parcel of solar wind plasma originated. The FIP and charge state abundances are particularly important tracers of solar source regions and processes as they do not evolve en route to the point of observation (as discussed in Section 1.3).

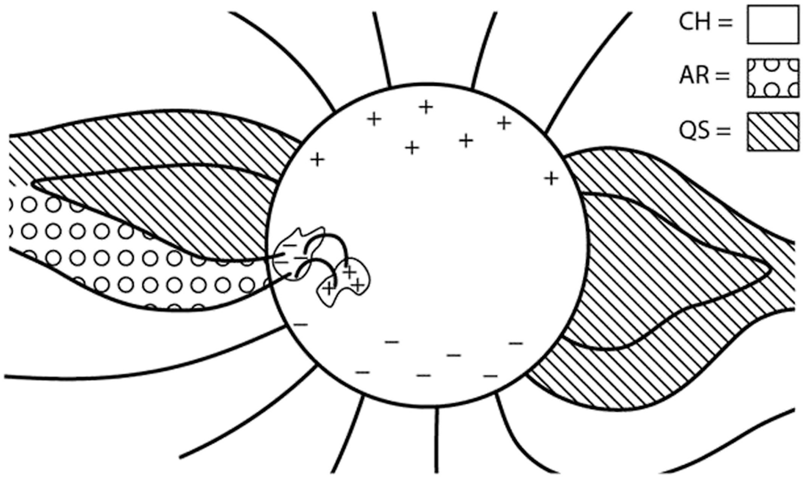

Figure 1.3: Conceptual diagram of the different source region categories on the Sun. Figure from *Viall et al.* (2021b).

1.1.3 The Solar Cycle and the Solar Dynamo

The sunspot cycle is an almost periodic 11-year variation in solar activity as measured by the average number of observed sunspots on the solar surface. Sunspots are dark, relatively cool regions on the Sun, caused by disturbances in the solar magnetic field. During a period of this cycle, the number and size of observed sunspots, solar radiation levels, levels of ejected material, solar flares and coronal loops vary together from solar minimum to solar maximum and back again. Solar flares and coronal mass ejections (CMEs) are prevalent during solar maximum and are called transients. Solar flares are localized eruptions of intense electromagnetic radiation and CMEs are large expulsions of plasma and magnetic field from the Sun's corona.

The solar dynamo is the physical mechanism that generates the magnetic field within the Sun. That magnetic field emerges through the photosphere, much of it extending through the different layers of the solar atmosphere. On some regions of the Sun, the magnetic field closes through the corona, while on other regions, one end is rooted in the photosphere, while the other end emanates out into the solar system with the solar wind (discussed in the next section). During solar minimum, the Sun's magnetic field is stable and resembles a dipole, stretched outwards at the equator, whereas during solar maximum it exhibits more complexity, corresponding to more intense solar activity. Hinode X-Ray Telescope (XRT) images of the Sun and the corresponding smoothed average sunspot number are shown in Figure 1.4 for most of solar cycle 24 as it approaches its 2019 solar minimum.

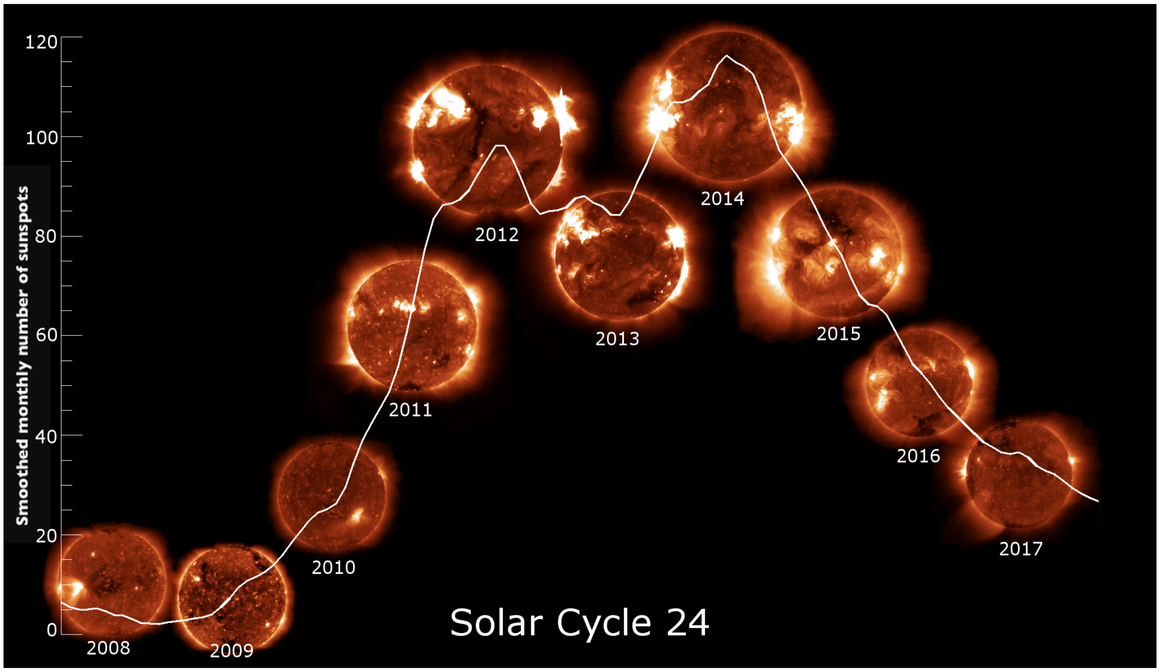

Figure 1.4: X-ray images of the Sun superimposed over smoothed monthly sunspot number plot (solar cycle 24). Graphic credited to Hinode XRT collaboration, Patricia Jibben.

The Sun's magnetic field has two poles, fundamentally like a bar magnet, but highly dynamic. Electric currents inside the Sun are at the heart of the solar dynamo which generates this field. The magnetic field reverses every 11 years at the peak of the solar activity cycle (solar maximum). Ground observations of solar activity span centuries, and those activities are reflected in the Sun's appearance as well as related terrestrial phenomena such as the aurora borealis, or the northern lights.

1.2 The Heliosphere and the Solar System

The Sun emits a constant flow of charged particles, primarily protons, electrons and alpha particles. This flow of particles constitutes a plasma which expands, carrying with it the solar magnetic fields, to form the heliosphere — a bubble encompassing the solar system in the vastness of the interstellar medium (ISM). The plasma is referred to as the solar wind and fills interplanetary space within the heliosphere.

The heliosphere is shaped like an elongated wind sock and moves with the Sun through interstellar space. Its structure is depicted in Figure 1.5, with key features labeled. The solar wind advects outwards to distances billions of kilometers from the Sun until it reaches the termination shock. At this point, its speed is reduced abruptly and becomes subsonic as it begins to fall under the influence of interstellar wind. The heliosphere is the bubble carved out by the solar wind and extends far beyond the planetary orbits in the solar system. The outer region of the heliosphere, the heliosheath, is the region just beyond the termination shock where the solar wind piles up, becoming denser and hotter, as it approaches the opposing wind in interstellar space. The boundary between the heliosphere and the interstellar wind is termed the heliopause; this is where the pressures of the two interacting winds are balanced. As the heliosphere moves through the interstellar wind, a bow shock is formed. Analogously, a similar structure is formed as the solar wind meets and is forced to flow around planetary magnetospheres, as shown in Figure 1.6, significantly contributing to space weather events. The heliosphere has an enormous impact on civilization. It protects the Earth from intergalactic cosmic rays and forms the medium through which space weather events, such as transients released from the solar corona, propagate.

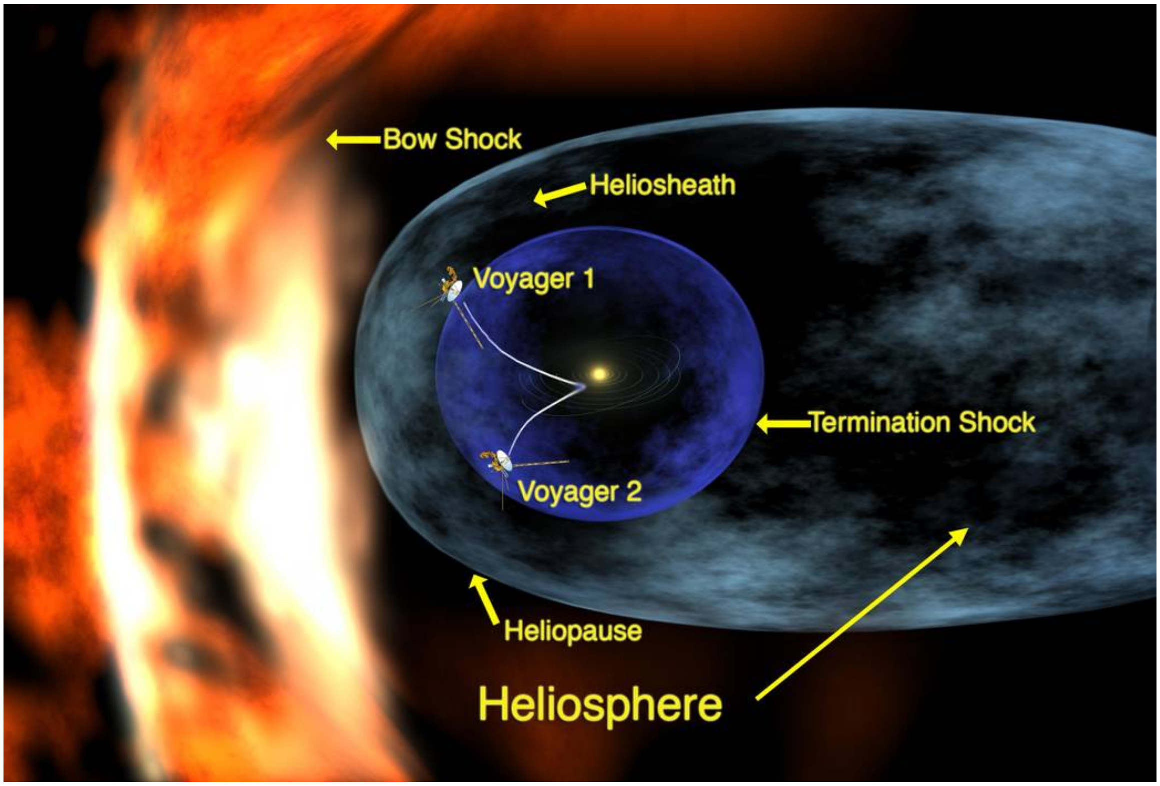

Figure 1.5: Artist's concept of the the heliosphere with major features labeled. Graphic credited to NASA.

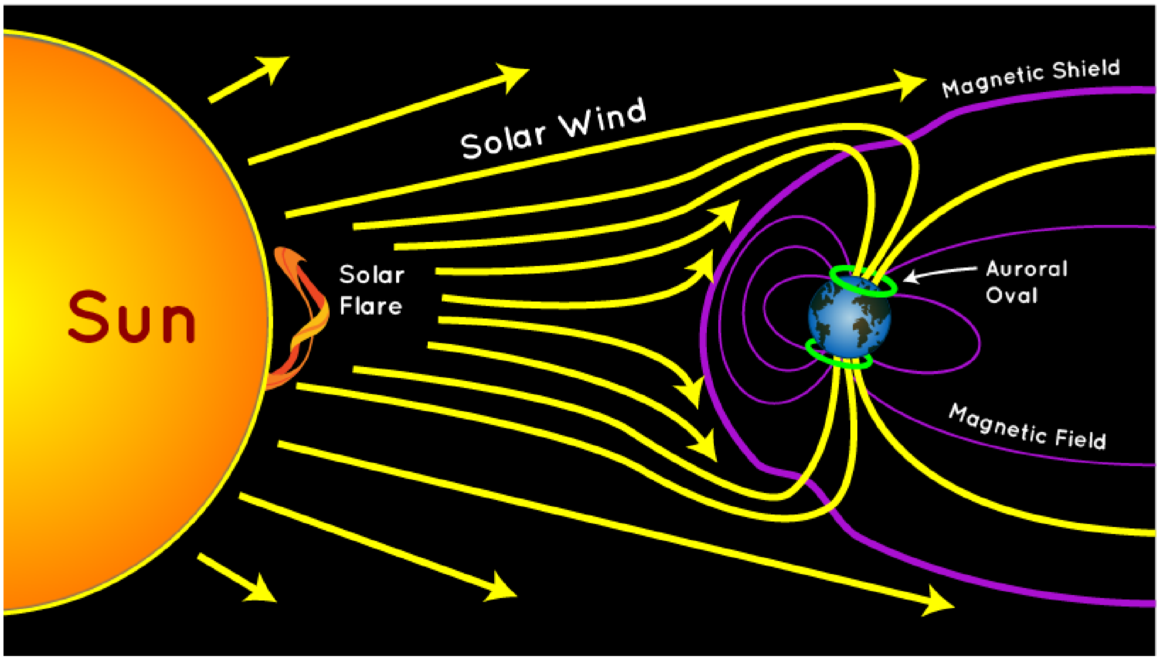

Figure 1.6: Earth's magnetosphere with the solar wind impinging upon it. The yellow arrows represent solar wind flow. Graphic credited to NASA.

1.3 The Solar Wind

The solar wind is characterized by varying solar wind speed, density, temperature, and ion composition. The states, or types, of solar wind that are observed in the heliosphere by spacecraft can provide clues to understanding the processes that govern the formation of the wind and affect its propagation through the heliosphere. These properties also help link *in situ* plasma measurements to the type of source region on the Sun that they correspond to. The solar wind plasma is composed primarily of protons, electrons and alpha particles but also contains trace amounts of heavier ions (*Bame et al.*, 1975). Measurements show that the solar wind density $n(r)$, outside the corona, up to a distance of several Astronomical Units (AU) decreases as $n(r) \propto r^{-2}$. At 1 AU, the proton density typically falls in the range of $\sim 3\ cm^{-3} - 10\ cm^{-3}$ and the plasma temperature, T, ranges from $\sim 10^5$ and $10^6\ K$ (*Baumjohann and Treumann*, 2012).

1.3.1 Fast and Slow Solar Wind

The solar wind can be categorized into two major types: the slow wind with bulk speeds typically less than 500 km/s and the fast wind with bulk speeds typically in the range of 500–800 km/s. The slow solar wind tends to originate from closed magnetic loops and is associated with lower-latitude regions on the Sun (during solar minimum) and AR as well as QS regions. The fast solar wind, on the other hand, tends to emerge from open magnetic field regions on the Sun called coronal holes (CH regions), which are located at the poles during solar minimum. Plasma in open flux regions is also released from small flux loops, but due to the high concentration of open flux, the loops will tend to open before the plasma is heated or fractionated substantially. Furthermore, the slow wind can be differentiated from the fast wind as it is denser, more variable in its properties, enhanced in heavy ions with low FIP and contains higher charge states (*Geiss et al.*, 1995; *Viall and Borovsky*, 2020; *Lepri et al.*, 2013).

Rather than referring to these wind types as fast and slow, it is sometimes more practical to refer to them as coronal hole (originating from CH regions) and streamer wind (origination from AR and QS regions). Due to the Sun's rotation and magnetic field, discussed in the next section, coronal hole and streamer wind often interact, forming a stream interaction region with higher plasma number densities due to the formation of a compression region, as shown in Figure 1.7. More observations of the solar wind revealed more complexity and it became clear that the historical bi-modal categorization of slow and fast wind is an oversimplification (*Zurbuchen et al.*, 2002; *Stakhiv et al.*, 2015; *Roberts et al.*, 2020; *Viall and Borovsky*, 2020). However, it can be a useful framework for discussing how solar wind observed *in situ* can be related to source regions and processes occurring in the solar atmosphere.

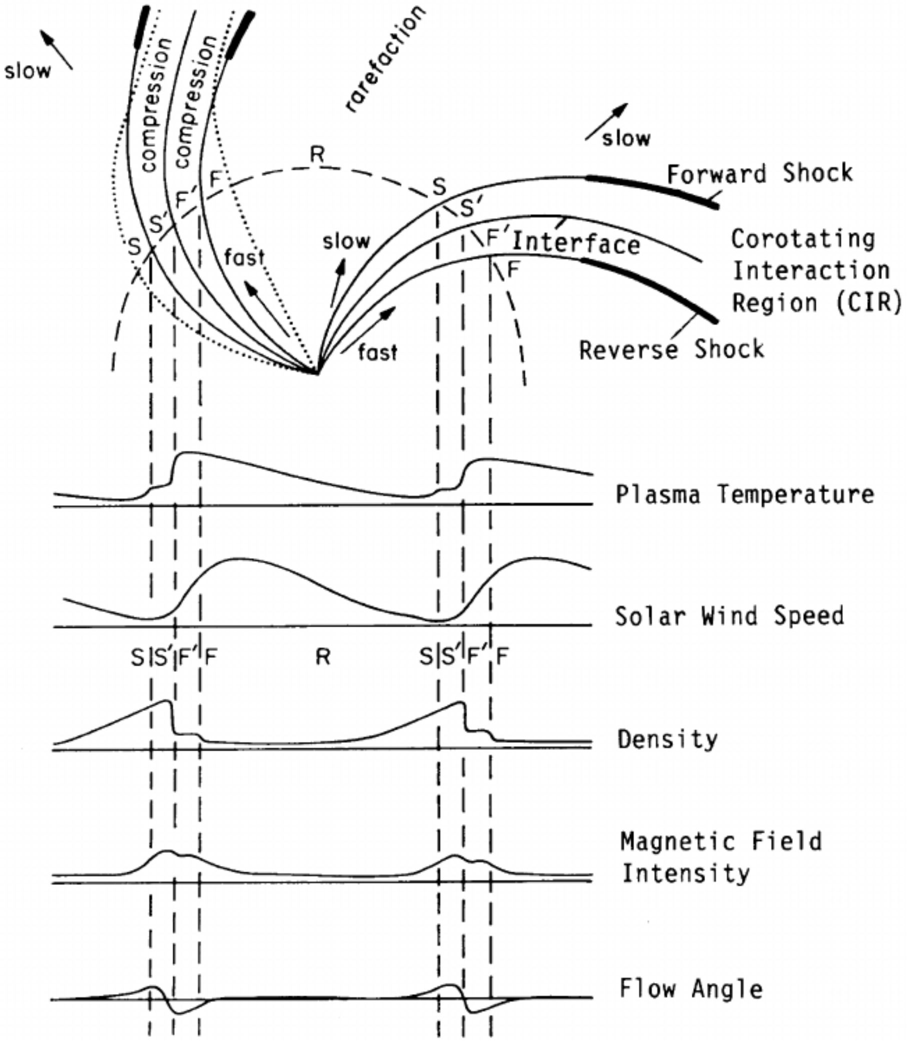

Figure 1.7: Diagram of two stream interaction regions rotating with the Sun and the corresponding plasma and magnetic field signatures. Figure from *Crooker et al.* (1999).

1.3.2 Charge States in the Solar Wind

The charge state abundances, or ionic composition, observed *in situ* by spacecraft in the heliosphere, are a powerful diagnostic of the physical processes occurring in the Sun and its atmosphere. This is because the rapid expansion of the solar wind causes the plasma to become so tenuous that the ionization and recombination rates become insignificant within a few solar radii from the Sun, depending on the ion. At this point, the charge states are said to be "frozen-in" to the solar wind (*Hundhausen et al.*, 1968). Charge-state ratios, such as O^{7+}/O^{6+} and C^{6+}/C^{4+}, are a proxy for coronal electron temperature and ion and electron densities within the local environment and tend to be enhanced in streamer solar wind (*Gloeckler et al.*, 2003; *Stakhiv et al.*, 2015; *Landi et al.*, 2011). Figure 1.8 shows the freeze-in temperatures for the O and C charge-state ratios and the distance (in units of $R_\odot$) at which each reaches equilibrium. Figure 1.9 shows Ulysses/SWICS measurements of daily averaged charge spectra for Fe, C, O and Si. The "North" and "South" labels indicate averaged measurements taken over the poles (corresponding to fast, coronal hole wind) and the "Max" and "Min" labels indicate averaged measurements taken at lower latitudes (corresponding to slow, streamer wind). *Von Steiger et al.* (2000) provides further details on the selection criteria that define these categories.

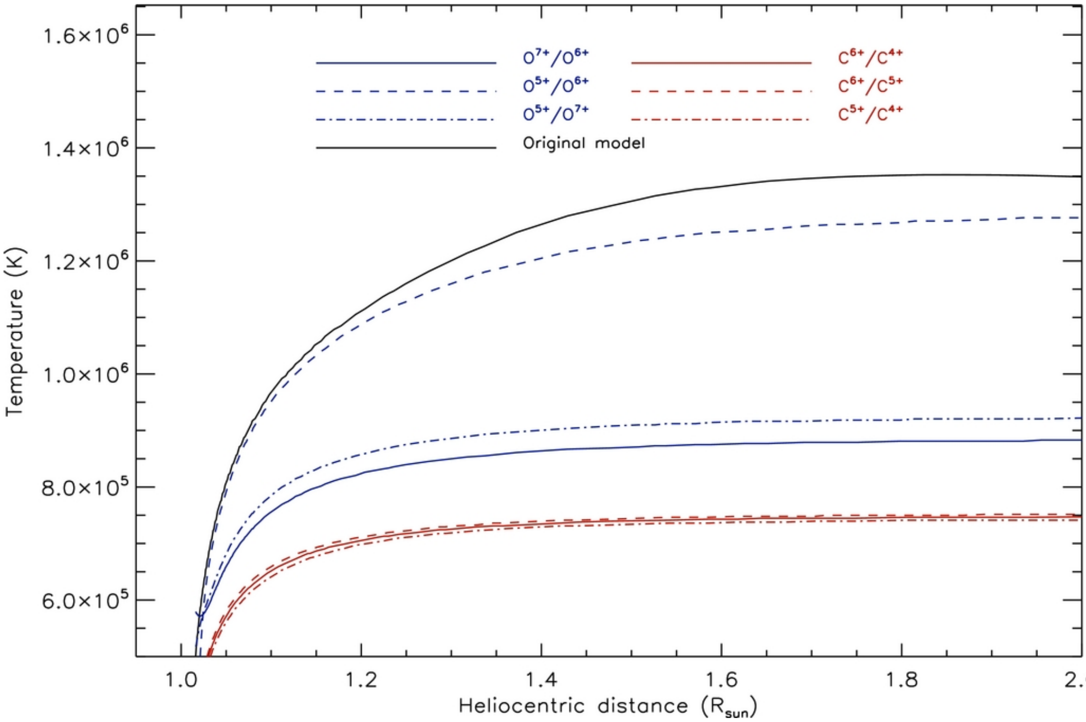

Figure 1.8: Temperature for the O and C charge state ratios as a function of distance from the limb (predicted). Figure from *Landi et al.* (2011).

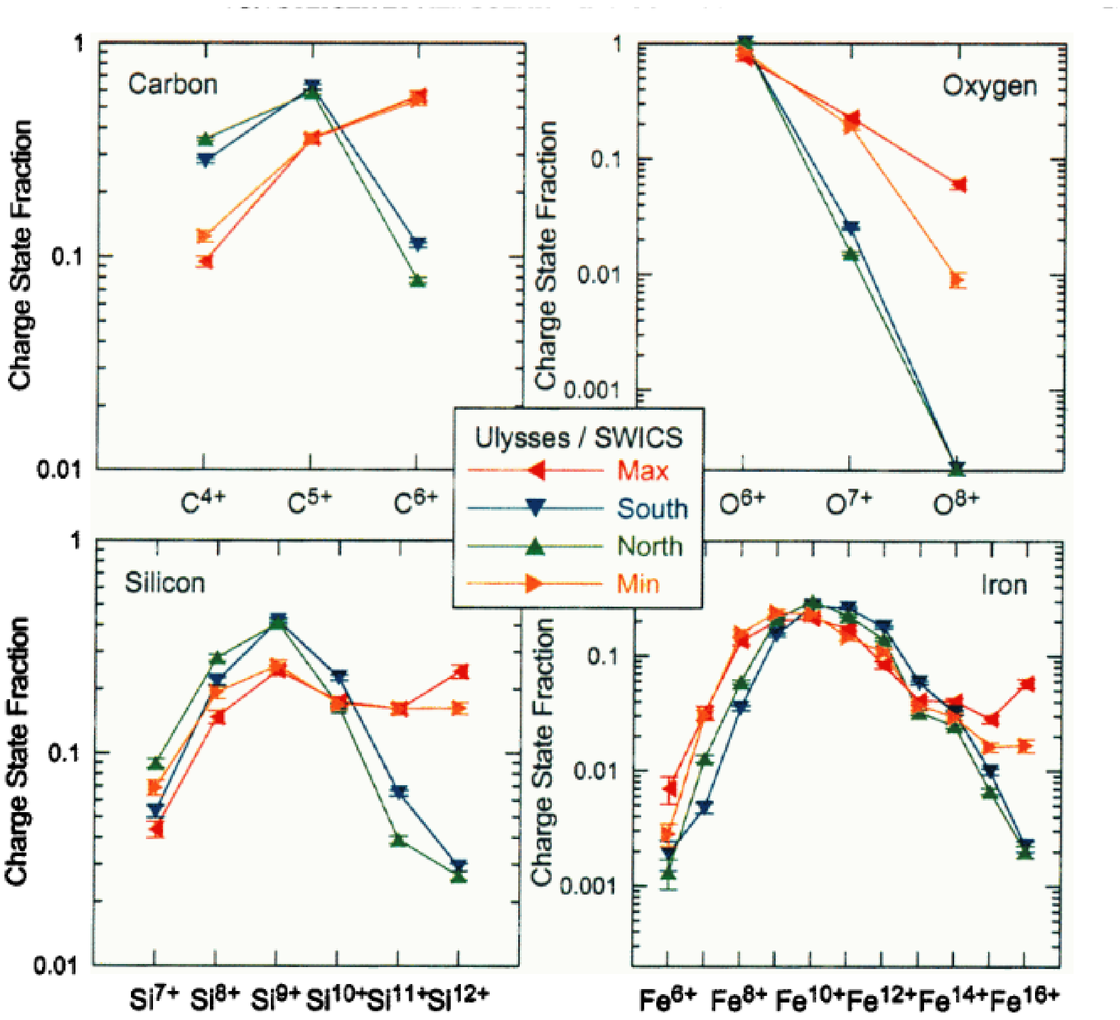

Figure 1.9: Charge state spectra of C, O, Si and Fe for average coronal hole and streamer solar wind measurements observed by the Ulysses/SWICS instrument. Figure from *Von Steiger et al.* (2000).

1.3.3 The FIP Effect

Early solar UV and X-ray spectroscopy observations showed that Mg, Fe, and Si abundances were significantly elevated in the corona compared to the levels observed in the photosphere (*Pottasch*, 1963). These elements all have a FIP of less than 10 eV and their enhanced abundances in the corona relative to the their photospheric levels is referred to as the "FIP effect". High FIP elements, such as He, O and Ne, are much less enhanced and are sometimes even depleted in the corona (*Laming*, 2015). The effect has been studied through several modes of observation, namely spectroscopy (*Pottasch*, 1963; *Feldman*, 1992; *Feldman and Laming*, 2000; *Feldman and Widing*, 2003; *Saba*, 1995) and *in situ* measurements (*Meyer*, 1985a,b; *Zurbuchen et al.*, 1999; *Von Steiger et al.*, 2000). These synergistic observations resulted in key discoveries that greatly advanced our understanding of the relationship between the properties of the solar wind, observed *in situ*, and the structures and regions on the Sun from which the wind originates. The spectroscopic observations showed the composition of closed loops in the corona to resemble the abundances observed in the slow, streamer wind (*Laming*, 2015). *In situ* observations from Ulysses, the first mission to fly over the solar poles, demonstrated that FIP fractionation varied with solar wind speed. Coronal holes were shown to have similar, photospheric-like abundances to the fast solar wind originating from them. The streamer wind, emanating from closed loops, showed elevated low-FIP abundances similar to the slow streamer wind. Coronal and solar wind abundances are reported as ratios with respect to O.

Typically, streamer wind tends to exhibit low-FIP abundance ratios that are elevated by a factor of 2–5 relative to their photospheric values. Figure 1.10 shows plots of remote and *in situ* FIP biases for key elements. Elements with intermediate FIP (such as C, P and S) can behave similarly to either low-FIP or high-FIP elements, depending on the details of the fractionation process and, likely, whether it occurs in open or closed magnetic field regions (*Laming et al.*, 2019). The FIP effect is determined in the chromosphere, where neutral particles exist. Species are ionized according to their FIP and accelerated by electromagnetic forces based on their ionization and mass, resulting in the observed fractionation. Like charge state abundances, FIP elemental abundances are determined near the Sun and do not evolve as they advect through the heliosphere. Thus, they are also excellent diagnostic tools for relating *in situ* observations to their sources in the solar atmosphere.

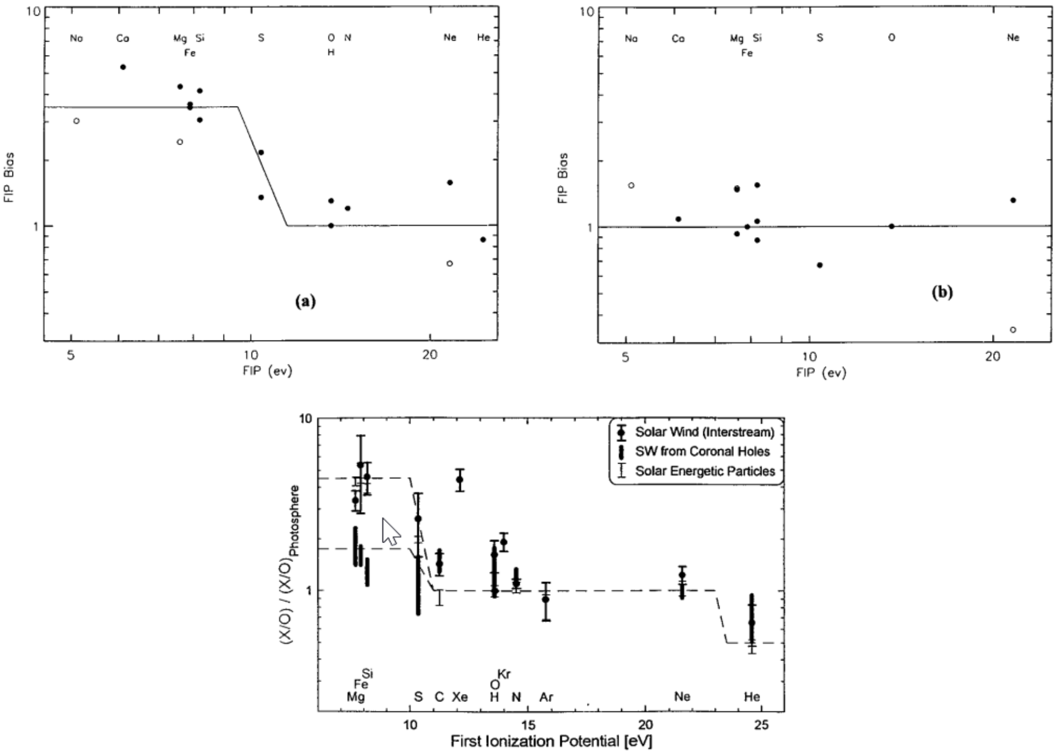

Figure 1.10: Remote and *in situ* measurements of FIP bias in streamer and coronal hole winds. **Top Left:** Abundance variations in quiet coronal regions. **Top Right:** Abundance variations in coronal hole regions. **Bottom:** Abundance variations in the solar wind, observed *in situ*. For all plots, abundances are relative to photospheric levels and normalized to O. Figure compiled from *Feldman* (1998); *Von Steiger et al.* (1997).

1.3.4 Solar Rotation and its Effects on the Solar Wind and the Interplanetary Magnetic Field

The opposite magnetic field polarities of the north and south solar poles create a current sheet, nominally, near the solar equator during solar minimum. Due to the fact that the magnetic axis is offset from the rotational axis of the Sun by $\sim 7°$, the Heliospheric Current Sheet (HCS) oscillates up and down as the Sun rotates (as shown in Figure 1.11), thus exposing the Earth, as well planetary orbits on the ecliptic, to solar wind from both the northern and southern hemispheres of the Sun. The HCS is shown in light and dark green, depending on whether it dips below or rises above the ecliptic plane, respectively. These periods of positive (away from the Sun) and negative (towards the Sun) polarities that the Earth experiences are known as magnetic sectors. The Sun is shown in orange and the blue and red regions above and below the HCS indicate the polarity of the magnetic field. The yellow region represents the outward flow of the solar wind.

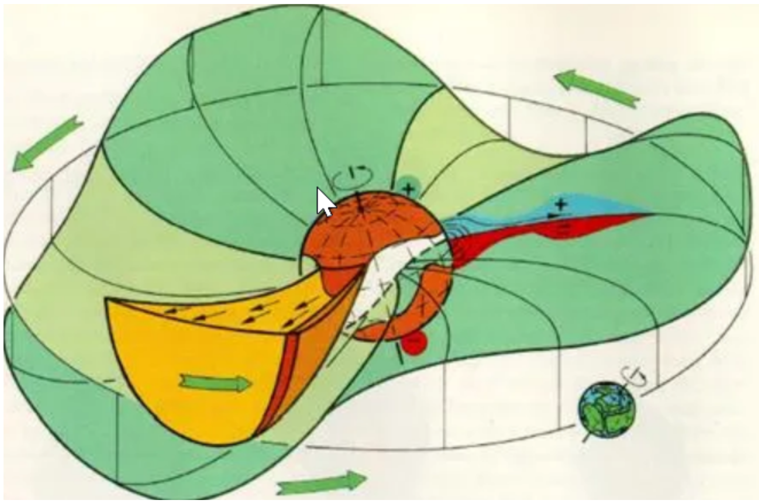

Figure 1.11: The Heliospheric Current Sheet (HCS) passing the earth in the plane of the ecliptic. Figure from *Heber and Potgieter* (2006).

1.4 Mesoscale Periodic Density Structures in the Solar Wind

The solar wind is not laminar but rather highly structured at a variety of scales (*Viall et al.*, 2021b; *Verscharen et al.*, 2019). On mesoscales – scales that are larger than kinetic scales but smaller than the largest structures in the solar wind (∼10–10000 Mm or, alternatively, on timescales ranging from seconds to several hours) – some structures enter the solar wind directly during their formation in the solar atmosphere while others evolve during propagation. For *in situ* measurements, the temporal scale is related to the frequency and the spatial scale as $f = 1/\Delta T = V_{SW}/L$. Here, ΔT is the time measured between successive periodic structures, V_{SW} is the solar wind speed and L is the spatial scale associated with the structures. Large-scale structures, such as CMEs and stream interaction regions, in the heliosphere are injected by the Sun, whereas mesoscale structures can either be injected during formation or evolve en route to the point of observation. Structures that form in the Sun and survive to their detection can provide crucial clues to the conditions and processes that led to their formation. Mesoscale periodic density structures are a subset of mesoscale structures and can provide these crucial insights as well as drive the dynamics of planetary magnetospheres (*Di Matteo et al.*, 2022) and shape the medium through which space weather events propagate. Figure 1.12 shows a conceptual diagram that summarizes the types of structures present in the solar wind and how their properties, and the modes of detection/study, overlap.

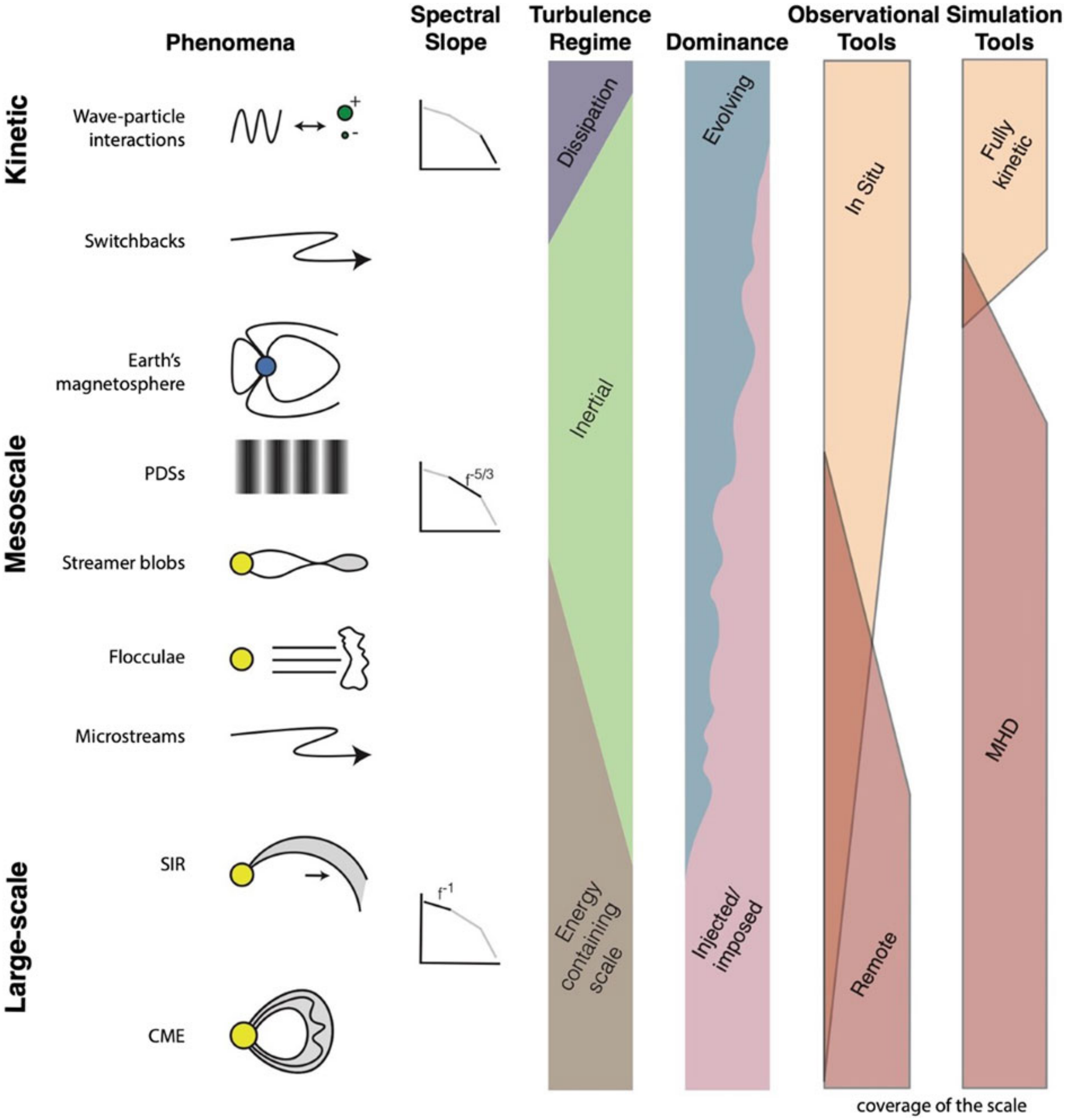

Figure 1.12: Kinetic, "meso" and large scale structures in the solar wind and their overlapping characteristics. Figure from *Viall et al.* (2021b).

Since the initial discovery of periodic density structures in the solar wind, there have been efforts to characterize them and to identify their source. *Viall et al.* (2008), *Viall et al.* (2009a) and *Kepko et al.* (2020) report statistically significant bands of frequencies in solar wind proton density measurements in *in situ* measurements at 1 AU. These studies demonstrated that a characteristic scale is present in the occurrence distributions of these structures, such that certain frequencies occur more often than others, and are therefore not simply attributable to turbulence.

Periodic density structures in the solar wind's elemental composition and charge state abundances are particularly useful in relating *in situ* observations to their sources on the Sun's surface. This is due to the fact that variations in composition form in the solar atmosphere and cannot evolve as they advect through the heliosphere to the point of observation, thus preserving information about the local conditions that led to their formation. This serves as an important diagnostic tool as there is not yet a well-understood one-to-one mapping between observed features in the corona and *in situ* observations in the heliosphere on mesoscales. Observations of periodic density structures in the solar wind's composition have been reported in event studies (*Kepko et al.*, 2016; *Viall et al.*, 2009b; *Gershkovich et al.*, 2022). Statistical studies of periodic density structures found in the solar wind's elemental and charge state composition are presented, for the first time, in this work.

1.5 Periodic Reconnection at Helmet Streamer Tips

While there are ideas as to how periodic fluctuations could be created in the Sun (*Réville et al.*, 2020; *Pylaev et al.*, 2017), many more detailed events are needed to thoroughly investigate those possibilities. *Réville et al.* (2020) reports on magnetohydrodynamic simulations of the solar wind and corona performed in order to model plasma outflows surrounding the HCS. Their work is able to explain long ($\sim$ 10-20 hour) and short ($\sim$ 1–2 hour, or 0.3 to 0.15 mHz) periodic density structures observed in the solar wind. *Réville et al.* (2020) suggest that periodic density structures could be associated with flux ropes (structures of twisted magnetic fields, threaded along an axis) being released from the tips of helmet streamers (closed coronal structures which connect field regions of opposite polarity) with the release of flux ropes being controlled by a flow-modified tearing mode at the HCS. *Pylaev et al.* (2017) also proposes quasi-periodic magnetic reconnection in helmet streamers and suggests that perturbations of the coronal base in the form of jets and explosive events generate acoustic pulses, which propagate upwards and leave the wake behind oscillating at the coronal cut-off frequency. The shocks may trigger periodic magnetic reconnection in helmet streamers, where field lines of opposite polarities merge and may, in this way, generate periodic density structures in the solar wind plasma. Their work predicts 80–90 minute (or ∼0.2 mHz) periodicities. Figure 1.13 shows a conceptual illustration of this process.

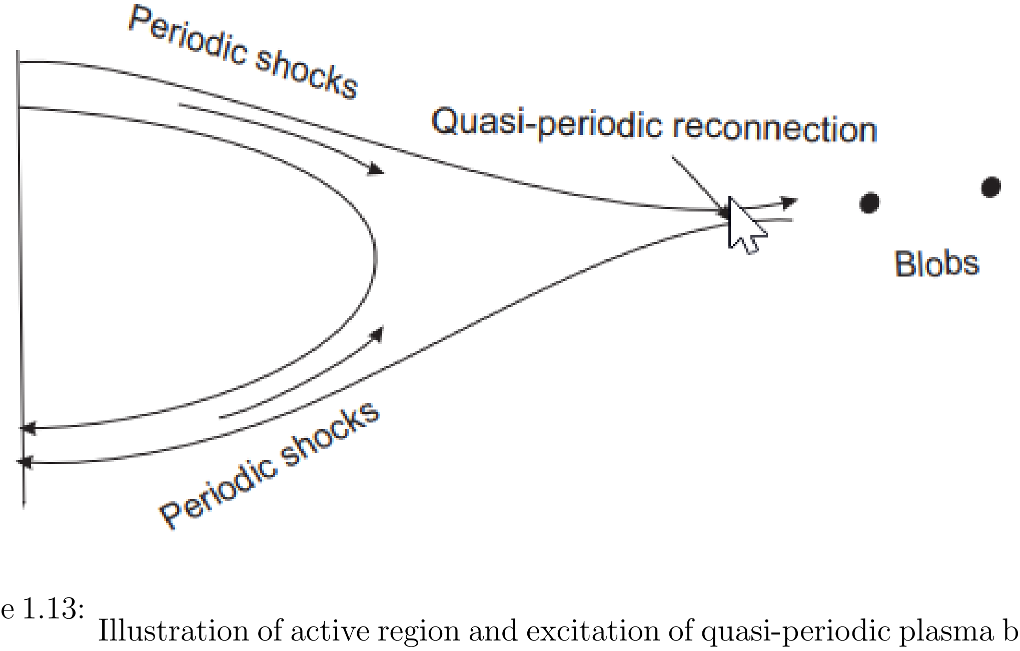

Figure 1.13: Illustration of active region and excitation of quasi-periodic plasma blobs due to recurrent shocks. Figure from *Pylaev et al.* (2017).

1.6 Interchange Reconnection

Interchange reconnection (*Fisk*, 2003; *Antiochos et al.*, 2011; *Crooker et al.*, 2002) between closed magnetic field regions and open magnetic fields is one possible explanation for how mesoscale periodic structures enter the solar wind (*Kepko et al.*, 2016; *Viall et al.*, 2009b; *Réville et al.*, 2020; *Di Matteo et al.*, 2019; *Viall and Vourlidas*, 2015b; *Higginson and Lynch*, 2018). This model explains the observed variations in composition well. However, the mechanisms that drive the periodicity are not yet clear and further event studies and modeling advances are needed in order to identify these mechanisms.

Figure 1.14 is a diagram showing how this process could potentially work. Throughout this work, we use variations in elemental and charge state abundances to reason about how *in situ* observations can be traced back to their source structures and mechanisms, primarily interchange reconnection, at the Sun.

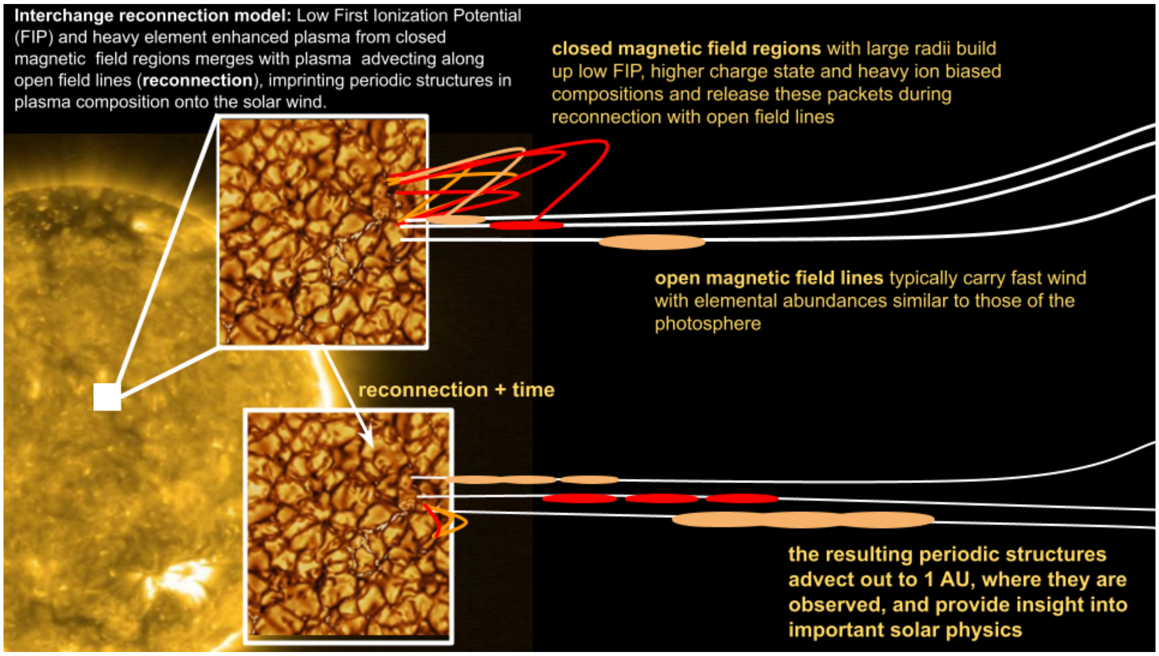

Interchange reconnection model: Low First Ionization Potential (FIP) and heavy element enhanced plasma from closed magnetic field regions merges with plasma advecting along open field lines (**reconnection**), imprinting periodic structures in plasma composition onto the solar wind.

closed magnetic field regions with large radii build up low FIP, higher charge state and heavy ion biased compositions and release these packets during reconnection with open field lines

open magnetic field lines typically carry fast wind with elemental abundances similar to those of the photosphere

the resulting periodic structures advect out to 1 AU, where they are observed, and provide insight into important solar physics

Figure 1.14: Illustration of interchange reconnection between closed magnetic loops and field lines open to the heliosphere as a potential mechanism for imprinting periodic density structures onto the solar wind.

1.7 Space Plasma Instrumentation

Figure 1.15 shows the Heliophysics System Observatory (HSO). It employs the entire fleet of solar, heliospheric, geophysical and planetary spacecraft to provide a distributed system of observatories that measure the space environment at different temporal and spatial scales, as well through different modes of observation. In this work, supporting observations from many of these missions are relevant, however we focus directly on data from *in situ* plasma spectrometers on board the Advanced Composition Explorer (ACE) and Solar Orbiter (SO) spacecraft.

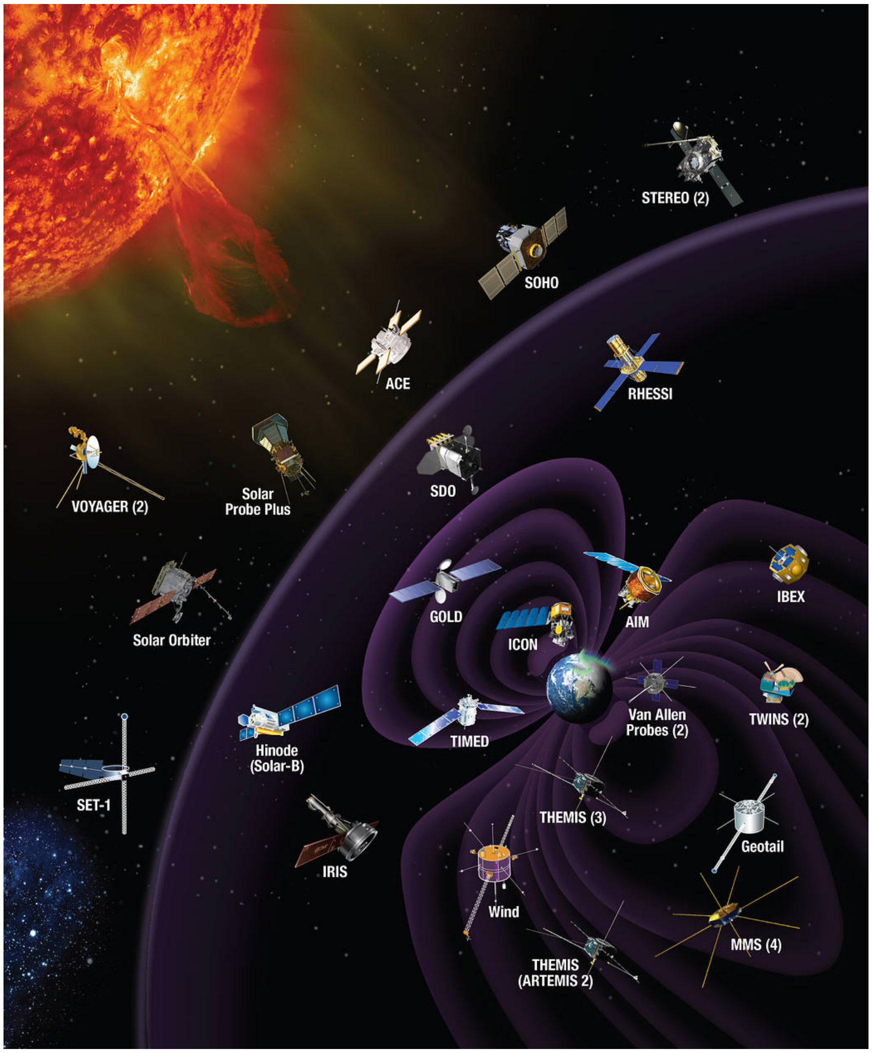

Figure 1.15: Heliophysics System Observatory (HSO). Graphic credited to NASA.

Direct, or *in situ*, measurements of space plasma ions have provided invaluable clues to the processes that govern the formation, release and acceleration of the solar wind. The instruments that allow us to extract useful information about plasma composition usually contain a filter at their entrance, called an Electro-Static-Analyzer (ESA), that feature electrode shapes and potentials that allow only ions of the selected kinetic energy per charge E/q to pass through to the interior of the instrument to be measured. These ESAs have a finite resolution ($\Delta E/q$) such that there is, in practice, a range of values that enter the instrument for a given E/q setting. Figure 1.16 shows a schematic diagram of the Solar Wind Ion Composition Spectrometer (SWICS) on board the ACE spacecraft.

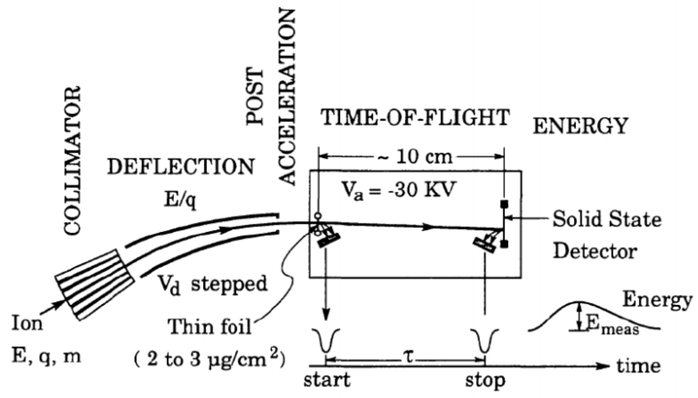

Figure 1.16: Schematic diagram of the ACE/SWICS instrument. Figure from *Tracy* (2016). Previously adapted from *Gloeckler et al.* (1992).

The operating principles, applied specifically to ACE/SWICS though relevant to other plasma spectrometers which contain an energy sensor, are summarized as follows:

1. Ions with a specific mass, charge and kinetic energy enter through the collimator.

2. The ESA filters the ions based on their energy per charge E/q, stepping through

the full range of E/q steps according to the science requirements and specifications of the instrument.

3. Ions are “post-accelerated” by a high potential drop (30 kV for SWICS) before entering the Time-of-Flight (TOF) and energy measurement system. They are post accelerated so that their energy can be measured by a Solid-State-Detector (SSD).
4. The particle’s speed is determined by measuring the time (τ) that it takes to travel between the start and stop Micro-Channel Plate (MCP) detectors, with a separation distance (d).
5. Finally, the residual energy is measured by the SSD.

From measurements of τ, the time of flight, and E_{meas}, the energy measured by the SSD, and knowing the E/q that the instrument is set to accept along with the post-acceleration voltage V_a, we can compute the ion’s mass (m), charge (q) and incident energy (E) as shown:

$$\begin{aligned} m &= 2(\tau/d)^2(E_{meas}/\alpha) \\ m/q &= 2(\tau/d)^2(V_a + E'/q) \approx 2(\tau/d)^2 V_a \\ q &= (E_{meas}/\alpha)/(V_a + E'/q) \approx (E_{meas}/\alpha)/V_a \\ E &= q(E/q) \end{aligned} \tag{1.1}$$

E' is to account for the energy loss that each ion experiences as it passes through a thin foil (*Ipavich et al.*, 1982) in order to trigger the start detector, and α (< 1) is the nuclear defect in the SSD (*Ipavich et al.*, 1978). The thin foil’s function is to eject an electron when the ion passes through it; this electron is what triggers the start detector.

1.8 Spectral Analysis of Astrophysical Time Series

1.8.1 Overview

This work uses a spectral analysis method (*Di Matteo et al.*, 2021) specifically aimed at extracting periodic fluctuations from physical time series characterized by a red-colored Power Spectral Density (PSD) – for which power decreases as frequency increases. We give a high-level overview of the relevant aspects here. The method employs the adaptive multitaper technique (*Thomson*, 1982) to evaluate the PSD of the time series and provides different options for determining the background PSD. We do this in order to reliably extract statistically significant enhancements in the spectral power at discrete frequencies and call this the "amplitude" test as it is used to detect enhancements in the spectrum of a certain amplitude above the background fit. Additionally, the method provides a harmonic F-test, which is a statistical test highly responsive to monochromatic and phase coherent components in the time series, based on a complex-valued regression technique used to characterize signal phase and amplitude (*Di Matteo et al.*, 2021; *Thomson*, 1982).

When possible, we use a combination of both the amplitude and harmonic F-test (in support of the amplitude test) to extract and verify periodic structures in the ACE/SWICS 12-minute data. While both the amplitude and the F-test produce false positives, signals that are identified by both tests independently are unlikely to be false and are associated with true physical signals (*Mann and Lees*, 1996; *Protassov et al.*, 2002; *Viall et al.*, 2008; **?**; *Vaughan*, 2010; *Di Matteo et al.*, 2021). We require all signals to pass at minimum the amplitude test at a 90% confidence level, thus expecting a false positive rate of 10%. This is a standard confidence threshold, extensively tested with Monte Carlo simulations (*Di Matteo et al.*, 2021), that balances the trade-offs between the potential of false positives and the possibility of missing a physical signal. The significance of any enhancements are evaluated relative to the power (amplitude test) and for phase coherence (harmonic F-test).

A modular, highly adaptable IDL implementation of this method, described in this subsection, is freely available (*Di Matteo et al.*, 2020) and is used to analyze each 24-hour segment in the study after they have been prepared and validated as described in each chapter.

1.8.2 Background Estimation and the Amplitude Test

The amplitude test involves calculating the spectra, smoothing the spectra, estimating a background fit, and finally, identifying statistically significant peaks relative to this background. This procedure is performed independently for each validated segment, thus we do not need to rely on the assumption that all intervals were the result of the exact same dynamic process. The background estimation relies on the multitaper method (MTM), which is used to convolve multiple orthogonal Slepian tapers with the data segment in order to provide multiple independent estimates of the spectra (*Thomson*, 1982). For this analysis, we smooth the raw spectra with logarithmically spaced bins in order to provide a smoothed estimate of the spectral background (*Papadakis and Lawrence*, 1993; *Di Matteo et al.*, 2021). We then fit the smoothed spectra to a Bending Power Law (BPL):

$$S(f) = N \frac{f^{-\beta}}{1 + (\frac{f}{f_b})^{\gamma-\beta}} \tag{1.2}$$

Here, N is the normalization factor, β is the spectral slope index at low frequencies, γ is the spectral slope index at high frequencies and f_b is the frequency at which the bend occurs. For very low values of f_b, the BPL collapses into a straight power law with a spectral slope of $-\gamma$. We use the BPL background assumption, first suggested by *Vaughan* (2010), as it has been shown to be a better fit at both lower and higher frequencies, for solar wind segments, than other background assumptions, such as the AR(1) (lag one autoregressive process) assumption used previously (*Mann and*

Lees, 1996; *Viall et al.*, 2008; *Kepko et al.*, 2020; *Di Matteo et al.*, 2021). However, Monte Carlo simulations performed using the BPL background assumption show that the MTM method flattens the background estimate at very low frequencies (*Di Matteo et al.*, 2021). This is not a region of interest for identifying mesoscale periodic structures in the solar wind and does not the affect the results at higher frequencies.

A major challenge of estimating the background for space physics time series is their variability. Even when the physical processes responsible for the creation of the PSD is known, individual segments may not always produce a PSD of that type. The power spectrum of solar wind time series depends on the type of wind that we are analyzing; this is particularly true with regards to the composition. For example, the spectral slope of solar wind parameters evolves with increasing distance from the Sun for velocity and magnetic field and is also impacted by discontinuities and anisotropies (*Roberts*, 2010; *Di Matteo et al.*, 2021). Classification of different solar wind streams is difficult, so we instead rely on fitting each segment individually.

1.8.3 Harmonic F-test

The amplitude test requires that a signal have strong power relative to the background (as defined by the selected confidence level), but does not test the discrete nature of the enhancement. The harmonic F-test is used in conjunction with the amplitude test in order to reduce false positives. The F-test tests for phase coherent signal but not for the power contained in those signals and is independent from the background fit (*Mann and Lees*, 1996). We put more emphasis on the results of the amplitude test because it extracts signals with a distinct amount of power above the red-colored background PSD of astrophysical time series (*Inglis et al.*, 2015), which is not assured by the F-test alone.

1.9 Thesis Overview

The science questions that this thesis addresses are focused on gaining an understanding of how the solar wind is formed and how, as well as from what source regions on the Sun's surface, it is released. Chapter II has been published in The Astrophysical Journal as (*Gershkovich et al.*, 2022).

The primary science questions that Chapter II addresses are:

1. What do periodic structures observed *in situ* in the solar wind's elemental and charge-state composition tell us about the regions on the Sun from which they originate and how they form?

2. Do *in situ* observations of periodic structures in solar wind composition support interchange reconnection as the mechanism responsible for the release of these solar wind plasma parcels?

In this chapter, we examine four 24-hour events during which mesoscale periodic structures were observed in the solar wind's elemental composition and charge-state ratios. We validate the ACE/SWICS Mg/O, Fe/O, C/O, He/O, O^{7+}/O^{6+} and C^{6+}/C^{4+} 12-minute time series data and examine it within the context of spectral analysis. We compare the periodicities observed for low-FIP, intermediate-FIP, high-FIP and charge-state ratios to determine if the results are consistent with interchange reconnection being the underlying mechanism responsible for the observed structures. These are among the first studies of periodic density structures observed in the heavy ion composition and they put important constraints on the mechanisms governing the formation and release of the solar wind.

The primary science questions that Chapter III addresses are:

1. Are periodic density structures present at statistically significant levels in the solar wind's heavy ion composition data?

2. Is there a characteristic scale that is prevalent?

3. Does the number or value of results depend on solar activity?

4. Is there a FIP or charge-state dependency evident in the results?

We validate 14 years (1998-2011) of ACE/SWICS data and examine 24-hour windows for periodic density structures. For the first time, we present occurrence distributions for Mg/O, Fe/O, Si/O, C/O, S/O, He/O, O^{7+}/O^{6+} and C^{6+}/C^{4+} density structures and report statistically significant frequency bands for each ratio as well as any characteristic frequencies that occur as enhancements relative to the smoothed distributions. We evaluate the results as a function of average yearly sunspot number and explore how they depend on FIP and charge state.

Chapter IV addresses the same questions as does Chapter II but also aims to determine if there is a relationship between orbital distance and the periodic structures observed in the data set using new data from the Solar Orbiter Heavy Ion Sensor (SO-HIS) spectrometer. This data set is preliminary and limited due to the fact that the instrument is still in the process of coming online and being tuned. A portion of this chapter is dedicated to characterizing it. We validate and examine 33 24-hour long windows for periodicities as the Solar Orbiter spacecraft travels from an orbital distance of 0.92 AU to an orbital distance of 0.46 AU from the Sun. We plot the spectral analysis results as a function distance and report on the patterns that emerge.

Chapter V summarizes the results and conclusions from each study and presents motivation and plans for future work.

CHAPTER II

Periodic Structures Observed in Measurements of Elemental and Ionic Composition in situ at L1

The contents of this chapter have been previously published in The Astrophysical Journal (*Gershkovich et al.*, 2022).

2.1 Background

Historically, the solar wind has been classified into two main categories: the slow wind and the fast wind. This categorization was based on *in situ* measurements of plasma speed and temperature as well as ionic and elemental composition, without direct information about the sources from which the solar wind originated. Compared to fast solar wind ($V_{sw} > 500\ km/s$), known to originate from coronal holes, the slow solar wind ($V_{sw} < 500\ km/s$) tends to be denser, hotter, and more variable in its properties. In addition, the slow wind is characterized by higher ionic charge states and stronger enhancements of elements with low first ionization potential (FIP) relative to their photospheric abundances (*Geiss et al.*, 1995; *Viall and Borovsky*, 2020; *Lepri et al.*, 2013). The question of the origin of the slow solar wind is still a major outstanding question in heliophysics, with leading theories indicating it can be released from large closed coronal magnetic loops or open fields at the boundaries of coronal holes near active regions (ARs) and quiet Sun (QS) regions (*Viall and Borovsky*, 2020). The elemental abundances found in the slow solar wind are similar to those remotely observed on large coronal loops and are often enhanced by a factor of 2-5 relative to photospheric levels (*Feldman and Widing*, 2003; *Laming*, 2015; *Laming et al.*, 2019). In contrast, the elemental abundances of the fast solar wind are more photospheric in nature, reflecting their direct release from coronal holes (*Geiss et al.*, 1995; *Von Steiger et al.*, 2000; *Laming*, 2015; *Stakhiv et al.*, 2016; *Brooks et al.*, 2020). As more observations over longer baselines and across spatial and temporal scales revealed more complexity, it became clear that the historical categorization of slow and fast wind is an oversimplification (*Zurbuchen et al.*, 2002; *Stakhiv et al.*, 2015; *Roberts et al.*, 2020; *Viall and Borovsky*, 2020). However, the variations observed in distinct parcels of solar wind can be related to different source regions, acceleration and release mechanisms, and processes back at the Sun.

The solar wind charge states, or ionic composition, used interchangeably throughout this chapter, are determined in the low corona where ionization and recombination processes occur and reflect the electron temperature and ion and electron densities in the local environment. Once the plasma has expanded out far enough that the interaction cross sections become too low to influence the plasma, the charge states of individual ions freeze-in and remain unchanged as they flow out into the heliosphere in the solar wind ((*Gloeckler et al.*, 2003; *Landi et al.*, 2012; *Gilly and Cranmer*, 2020)). The Oxygen (O) charge state ratio O^{7+}/O^{6+} and the Carbon (C) charge state ratio C^{6+}/C^{4+} can be used as proxy for coronal electron temperature to provide insight into the sources of the wind. We use these charge state ratios specifically because they are composed of ions that are prevalent in the solar wind and, therefore, they have been studied extensively and shown to be good proxies for solar wind speed and type (*Gloeckler et al.*, 2003; *Stakhiv et al.*, 2015; *Landi et al.*, 2011).

Elemental abundances of solar wind ions are influenced by fractionation before they flow out into the solar wind. The FIP effect, which fractionates ions based on their first ionization potential, is determined in the chromosphere, where neutral atoms exist and are differentially ionized and accelerated upward by electromagnetic forces depending on their FIP (*Laming*, 2015; *Laming et al.*, 2019). Low First Ionization Potential (FIP) elements, such as Magnesium (Mg) and Iron (Fe), with a FIP of 10 eV or lower, are measured to be enhanced relative to higher FIP elements such as O in the corona (compared to their photospheric values) and are also used to discriminate between solar wind source regions. This is often referred to as the FIP effect and it is substantially more pronounced in some solar source regions than others, as we describe below.

In this chapter, we identify and examine periodic density structures in the solar wind, observed in heavy ion signatures, with the intent of studying the origin and processes that release the slow solar wind into the heliosphere. In Section 2.2, we provide a review of periodic structures previously observed in the solar wind and discuss how we greatly expand upon all past reports of *in-situ* heavy ion composition variations measured in the solar wind. In Section 2.3, we describe the methodology that we use to validate data, select events and identify periodic enhancements using a spectral analysis method specifically designed for extracting periodic signals from astrophysical time series. We focus on high time resolution (12-minute) composition data from the Solar Wind Ion Composition Spectrometer (SWICS) onboard the Advanced Composition Explorer (ACE) which enables us to examine finer spatial and temporal structures. In Section 3.3, we present four events during which periodic variations of heavy ion abundances and charge states were observed *in situ*. We focus on one event as a detailed case study and then examine the results of all four events, taken together, in order to compare and contrast their defining properties. In Section 3.4 we discuss the meaning of our results and how the events examined in this paper exhibit behavior that doesn't neatly fit into the historical bi-modal solar wind classification, but instead exhibit more subtlety. In Section 3.5, we summarize our work and the implications for our findings. The variations in the solar wind composition that is exhibited in all events were formed in the solar atmosphere as the composition cannot evolve en route to Lagrange point 1 (L1). The differences observed between events highlight the complex nature of the formation processes involved. We draw upon previous research to show that the results are consistent with interchange reconnection being the process responsible for the formation of these structures. We suggest that future work focus on conducting larger statistical studies of the ACE/SWICS data set and also applying the techniques given here to new data sets from higher resolution instruments such as Solar Orbiter's Heavy Ion Sensor(HIS).

2.2 Mesoscale Periodic Structures in the Solar Wind

Decades of *in-situ* observations have revealed that the solar wind is not laminar, but rather highly structured at many different scales (*Viall et al.*, 2021b; *Verscharen et al.*, 2019). On mesoscales, scales that are smaller than the largest structures in the solar wind but larger than kinetic scales, some structures enter the solar wind directly from the solar atmosphere during their formation while others evolve during propagation. The structures that originate in the solar atmosphere and survive to their detection can retain signatures of the processes that form the solar wind. Mesoscale structures in the solar wind not only provide information about the formation of the solar wind in general, but also are important because they can drive dynamics of magnetospheres (*Di Matteo et al.*, 2022) and they form the medium through which larger space weather events propagate. *Viall et al.* (2021b) provides a comprehensive review of mesoscales, including periodic density structures, observed throughout the heliosphere. They have been observed at scales as small as several minutes (or approximately one hundred Mm), and as large as several hours (or several thousand Mm). References are many, but include measurements *in situ* in and around L1, *in* *situ* in Helios data, remotely in STEREO COR2 and remotely STEREO HI1 data (*Kepko and Spence*, 2003; *Kepko et al.*, 2002a; *Viall et al.*, 2008, 2009a, 2010; *Viall and Vourlidas*, 2015a; *Kepko and Viall*, 2019; *Kepko et al.*, 2016, 2020; *Di Matteo et al.*, 2019).

Periodic mesoscale structures in proton density at Lagrange point 1 (L1) have been studied statistically and shown to preferentially exhibit characteristic frequencies, ruling out turbulence as the formation mechanism (*Viall et al.*, 2008; *Kepko et al.*, 2020). A frequency band centered around ∼0.6 mHz was one such characteristic scale observed in slow solar wind. Similar structures in electron density have also been verified to originate directly from the corona by comparison of the *in situ* observations to periodic structures seen in white light images (*Viall et al.*, 2010; *Viall and Vourlidas*, 2015a). Periodic mesoscale structures in alpha and proton densities and the alpha-to-proton ratio have been shown to exist by *Viall et al.* (2009a). However, only one periodic structure event has been reported using the elemental composition of the solar wind in the ACE/SWICS data (*Kepko et al.*, 2016). Here, we expand on previous studies and explore four such events, looking at variations in elemental composition and charge state, using the 12-minute high-resolution SWICS data set, to explore how the structures could have formed. We test whether these events originate in the Sun by examining trends and structure in these elemental composition and charge state variations. Our purpose is to identify periodic mesoscale structures for which we have composition data of sufficient quality (adequate counts) and quantity such that we can determine that the periodic mesoscale structures were formed in (or in other words, their source is in) the solar atmosphere. We then link these to general regions and formation mechanisms on the Sun.

2.3 Methodology

2.3.1 Time Series Data: Preparation for Spectral Analysis

Each of the four events nominally spans a total of 72 hours and is divided into three 24-hour windows. In practice, some windows that we run spectral analysis on were shorter due to the amount of continuous heavy-ion data that we were able to validate. However, we do examine and show the full 24-hour windows when describing general trends in solar wind properties and composition. The middle 24-hour window of each event satisfies the requirement of having significant counts and continuity in the heavy ion data. There are potentially many such segments in the data set, however these events were chosen to be validated iteratively, as shown for Fe in the 2.4.1 section, and to be explored in detail, prior to examining them for periodicity. The 24 hours before and after are examined in order to provide context about the surrounding solar wind. Each consecutive 24-hour window in each of the four 72-hour events is independently examined for periodicity. Subsection 2.4.1 provides further information about what defines an event.

We require all signals to pass at minimum the amplitude test at a 90% confidence level, thus expecting a false positive rate of 10%. Prior to running the spectral analysis procedure described in 1.8, the 24-hour-long time series data are first prepared by validation, de-spiking, and re-sampling routines in order to account for any data gaps, uneven sampling and outliers. This is necessary for all spectral analysis; it would violate the assumptions of spectral analysis if the data are not re-sampled to a common time step. The validation step, the criteria for which are specified in this subsection, ensures that there is continuity and counts adequate for running spectral analysis on a given window. We choose a 24-hour period to analyze as this provides us with enough data points (120 points) to run spectral analysis with sufficient spectral resolution. The data are de-spiked by removing outliers that exceed a 5σ threshold above a rolling window averaged version of the time series using twelve data points. The data are then re-sampled to a 12-minute time step and split into windows that are between 18 and 24 hours long, depending on the quality and continuity of the heavy-ion number density data which are limited by low counts at this time resolution. In this data set, the other elements typically have much higher accumulated counts over the 12-minute native sampling period of the SWICS instrument.

The percentage of missing data points must be less than a threshold value of 20% for each 24-hour window. The number of allowed consecutive missing data points must be less than a threshold value of three. Additionally, we require visual inspection to ensure that the time series does not exhibit unexpected features that could interfere with spectral analysis beyond the criteria we have explicitly stated. We give an example of the Fe data validation for an event in Section 2.4.1. We perform this validation for each element, for all 24-hour time windows that we analyze.

2.3.2 Instrument Description and Limitations

The ACE spacecraft orbits around L1; on board is the SWICS instrument, which is a plasma spectrometer designed for measuring heavy ions identical to the SWICS spectrometer flown on the Ulysses mission (*Gloeckler et al.*, 1992, 1998). The SWICS instrument is a triple coincidence time-of-flight mass spectrometer that employs an electro-static analyzer (ESA) at its entrance to select ions with specific energy-per-charge along with a time-of-flight telescope with integrated micro-channel plates (MCPs) and solid-state detectors (SSDs). The time-of-flight telescope, paired with the ESA, enables measurements of both the ion's energy and time-of-flight for the explicit calculation of its mass, charge and speed, providing the most robust measurement possible within the instrument's resolution limits. The ACE/SWICS data has been used extensively and the instrument, as well as the data processing techniques, have been described in detail (*Gloeckler et al.*, 1992, 1998; *Von Steiger et al.*, 2000;

Shearer et al., 2014). While most prior studies with ACE/SWICS have focused on data summed to a 2-hour time resolution, here we use the native 12-minute time resolution data in order to study smaller structures in the solar wind (as was done by *Kepko et al.* (2016)). Since this pushes the statistical limits for some less abundant ions such as Fe and Mg, we rely on the statistical uncertainties in the count rates to limit our selection to intervals with sufficient counts. In Section 2.4.1, we discuss the validation of the Iron data in detail in order to demonstrate the techniques used to validate all elements that we consider in this analysis. ACE/SWICS has operated continuously since 1998.

2.3.3 Event Definition Criteria

Apart from the data validation criteria stated above, we require that each event satisfy the following:

1. The three-day window does not contain a Interplanetary Coronal Mass Ejection (ICME). This was confirmed by using the Richardson & Cane ICME list (*Richardson and Cane*, 2010).

2. At least two elemental composition ratios (out of He/O, C/O, Mg/O and Fe/O) can be validated, according to the criteria stated above, on the central 24-hour window of the 72-hour total event.

3. At least one elemental composition ratio (out of He/O, C/O, Mg/O and Fe/O) contains a statistically significant periodic structure, as determined by the spectral analysis methodology described above, during one of the three 24-hour windows comprising the event.

Again, our aim is to identify periodic mesoscale structures for which we have composition data of sufficient quality and quantity so that we can determine that the periodic mesoscale structures were formed in (or in other words, their source is in) the solar atmosphere. A periodic variation in either elemental composition and/or ionic charge state indicates that the periodic mesoscale structures were formed in the solar atmosphere, and not formed en route as the solar wind advects. Comparing and contrasting the spectral analysis results for high-FIP (He/O), intermediate-FIP (C/O) and low-FIP (Mg/O and Fe/O) elemental composition ratios, as well as examining charge-state ratios, allows us to put constraints on the solar atmospheric processes that led to the formation of these structures.

2.4 Results

2.4.1 Event Study

We begin by showing an event covering the central 24-hour period on 4 March 2002 (1), which includes validated Fe data. We name the 24-hour period used to initially identify the event the "central" time period, the 24-hours prior the "beginning" and the 24-hours after the "ending". We show and analyze the "beginning" and "ending" segments in order to provide context and show days before and after the "central" period, thus characterizing the surrounding solar wind.

Figure 2.1 shows the plasma diagnostic time series for this event. The gray region, and the dashed black lines, mark the boundaries of the central 24-hour window. From top to bottom panel, the time series shown are: the 272 eV electron pitch angle distribution function value, proton number density, solar wind bulk speed, solar wind bulk temperature, magnetic field magnitude, and vector components of the magnetic field in the Radial Tangential Normal (RTN) spacecraft-centered coordinate system (radial in blue, normal in green and tangential in orange). This event takes place within a Stream Interaction Region (SIR): the increase in the proton density (panel a), the positive gradient in solar wind speed throughout the gray central period (panel b), and the increase in the magnetic field magnitude (panel d) are characteristic of a faster wind overtaking slower wind and the creation of a compression region at the interface (*Richardson*, 2018). The 272 eV electron pitch angle distribution measured by the ACE SWEPAM instrument for this event indicates a Heliospheric Current Sheet (HCS) crossing, evident in the 180° change in the electron pitch angle, beginning at around 2002-03-03 21:00:00.

Figure 2.2 shows the behavior of the solar wind elemental and ion composition during the 72 hours of the event. The average elemental abundances observed in fast and slow wind, following *Geiss et al.* (1995); *Von Steiger et al.* (2000), are overplotted in blue and red, respectively. The typical abundance for C/O is the same for fast and slow winds and is shown in purple for that composition ratio. From the top panel to the bottom, we show the elemental composition ratios Fe/O, Mg/O, C/O and He/O and the charge state ratios C^{6+}/C^{4+} and O^{7+}/O^{6+}. We plot the individual components that contribute to each ratio in order to show how each element or ion contributes to the variation of the elemental or charge state ratio that it is a part of. For example, in the central gray region of panel a), we can see that the Fe and O time series vary similarly, but not identically, during the first half of the segment and then diverge during the second half. This is reflected in the variation of the Fe/O time series by a dip during the latter half of the central segment. The component time series are shown in blue and green and are normalized such that their maximum value corresponds to the maximum value of the overall ratio time series.

The data plotted are validated according to the specifications described in Section 2.3. The elements that constitute the ratios are composed and validated separately, in order to determine which charge states are to be included, so a validated O data point will not necessarily be validated for Fe. Both elements are required to be validated in order to validate the ratio. Later in this section, we show the process and results of validating the Fe data (prior to incorporating it into the Fe/O ratio) for the central segment of this event in order to demonstrate the process used to validate all elemental time series.

Figure 2.2 shows the relative abundance of low-FIP elements (Mg/O and Fe/O) drop by a factor of 2 over the course of the 72-hour window. The Mg/O ratio in Figure 2.2b drops abruptly at the interface between the beginning and central segments and remains at the 0.1 level during the central and ending segments. Charge state ratios (panels e and f) drop by a factor of 5, fairly abruptly, similarly to the Mg/O ratio. The Fe/O ratio in panel a) drops slowly throughout the central region and then remains at 0.08 during the ending time period. There is a drop in C/O and He/O and a rise in proton density at around 2002-03-03 21:00:00, corresponding to the HCS crossing. Note that this rise in proton density also corresponds to the front edge of the ramp-up in velocity, which is a classic signature of the compression region of a stream interaction.

Figure 2.3 shows spectral analysis results for the elemental composition and charge state ratios during the central 24-hour segment of the event. The y-axis shows the power in panels d-f and j-l and the F-test value in panels a-c and g-i. The x-axis shows the frequency in mHz. The F-test results (panels a-c and g-i) are marked by red triangles and are shown as peaks rising above the dashed red 90% confidence threshold line. As stated in Section 2.3, we only consider F-test values that correspond to a concurrent amplitude test result to be valid. Panels d-f and j-l show the raw PSD (black solid line), the PSD background fit (red solid line), the 90% above background confidence curve (red dashed curve) and the results: purple circle for peaks that pass the amplitude test and black "x" for peaks that pass the amplitude test and the harmonic F-test. Note that all elemental composition ratios with statistically significant results during this event exhibit periodic structures at around 0.5 – 0.6 mHz.

Table 2.1 summarizes the periodic structures associated with this event for each elemental composition (Fe/O, Mg/O, C/O and He/O) and charge state (C^{6+}/C^{4+} and

O^{7+}/O^{6+}) ratio during the three 24-hour segments. The result columns indicate “low counts” if the counts accumulated by the instrument, per its 12-minute measurement, were insufficient for spectral analysis and “None” if periodic structures were entirely absent from that segment of data. The tests that each selected signal passed are listed in parenthesis after it; “amp” for the amplitude test and “F-test” for the harmonic F-test. Several signals listed in the table pass both tests. Though we identified the event based on the count rates in Fe and the presence of a periodicity in the central 24-hour time window, periodic structures appear throughout all 72 hours of the event.

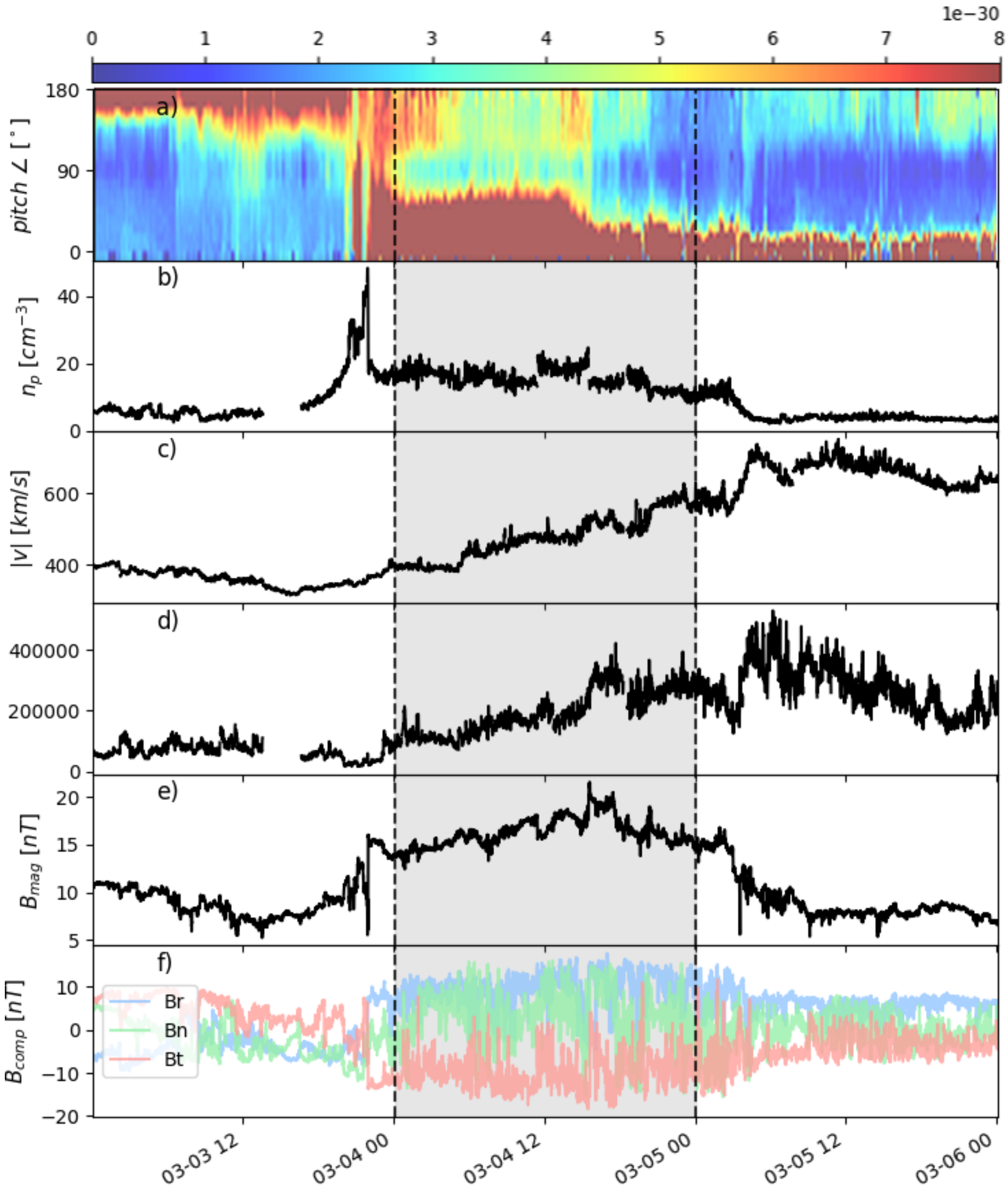

Figure 2.1: Plasma diagnostic time series plotted for the 4 March 2002 (1) ACE/SWICS event. The region bracketed by dashed black lines is the central 24-hour segment for the event, selected for its Fe data quality, in terms of instrument counts and segment continuity.

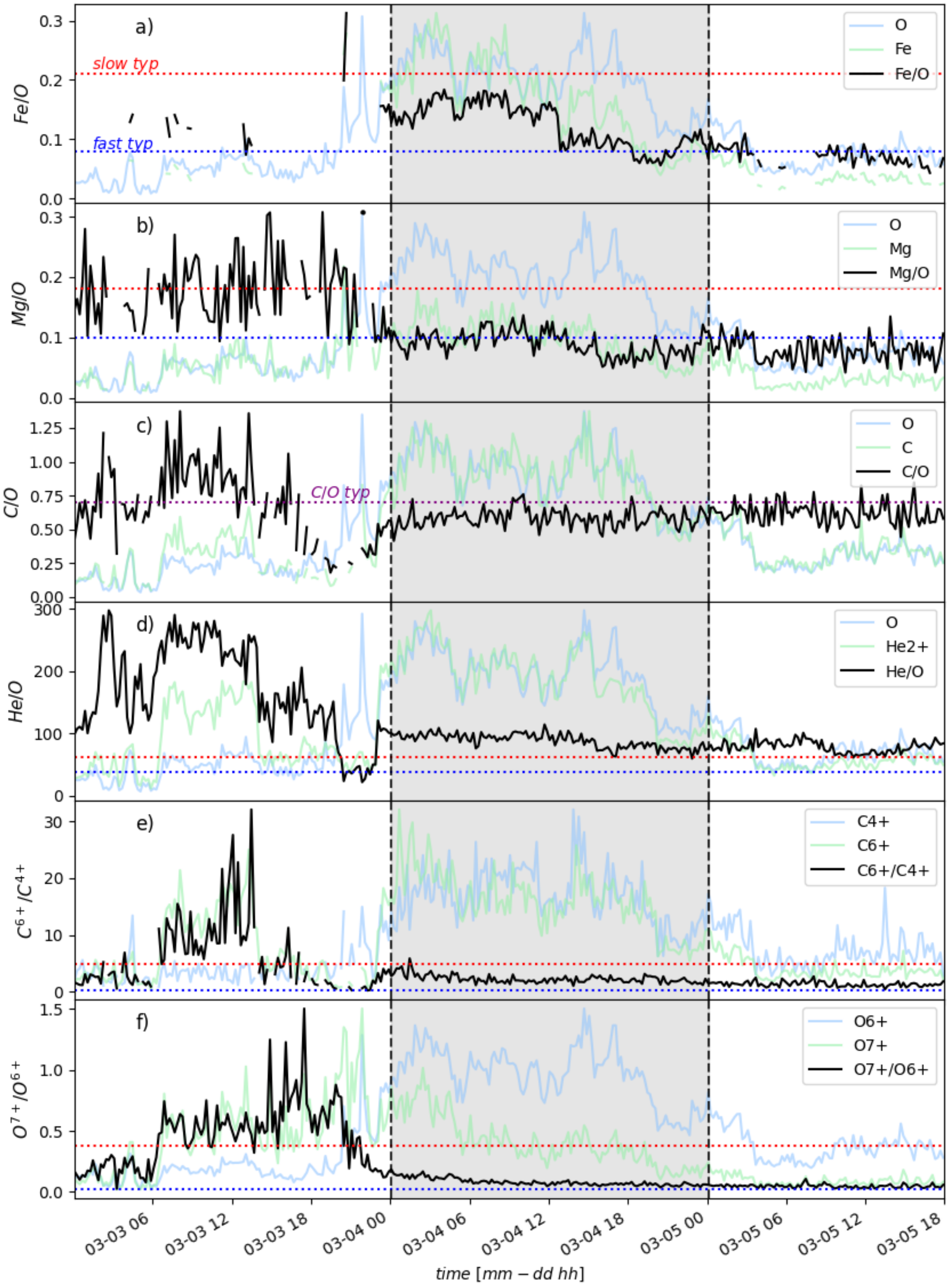

Figure 2.2: Elemental composition and charge state ratio time series for the 4 March 2002 (1) ACE/SWICS event are shown in black. Time series showing the variation of the component elements that contribute to each ratio are normalized relative to the maximum of the ratio time series and shown as blue and green traces.

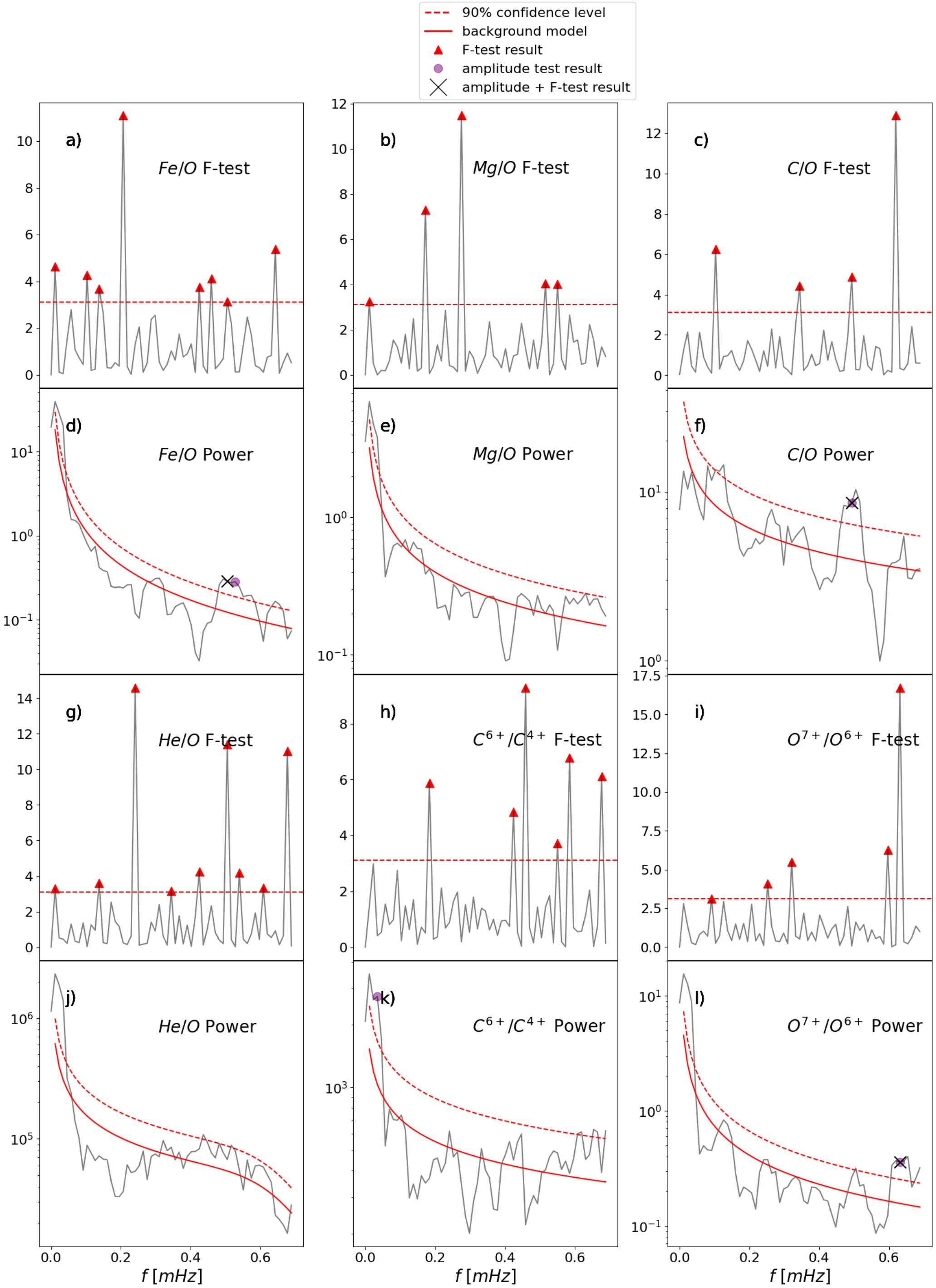

Figure 2.3: Spectral analysis results for all elemental composition and charge state ratios. These results correspond to the "central" time window of the 4 March 2002 (1) ACE/SWICS event.

	beginning	central	ending
Fe/O	low counts	0.51 mHz (amp + F-test)	low counts
Mg/O	low counts	None	0.51 mHz (amp + F-test)
C/O	low counts	0.49 mHz (amp + F-test)	None
He/O	low counts	None	0.05 mHz, 0.6 mHz (amp)
C^{6+}/C^{4+}	low counts	0.03 mHz (amp + F-test)	0.37 mHz (amp + F-test)
O^{7+}/O^{6+}	0.64 mHz (amp)	0.64 mHz (amp + F-test)	None

Table 2.1: Summary of periodic structures observed during the 4 March 2002 (1) ACE/SWICS event. The labels "low counts" and "None" indicate that the accumulated counts were insufficient for that ratio in that segment or that there were no periodic structures detected with 90% confidence, respectively. Note that results occurring at very low frequencies (below ∼0.1 mHz) are not robustly determined for 24-hour segments using our spectral analysis technique and may be false positives (*Di Matteo et al.*, 2021).

Recall that Fe is the element for which we have the most sparsely validated data, as it is least abundant. Table 2.2 shows a manual parameter scan of the different Fe charge states used to validate the ∼0.5 mHz peak in the Fe data. The values shown correspond to the central 24-hour segment in this event. This step is performed for all heavy elements, prior to incorporating them into the elemental composition ratios, in order to determine which charge states need to be included for the element. For example, Fe^{10+} is typically the dominant Fe charge state, in terms of abundance and number of counts, but there are others in the data set (see Figure 2.4). Table 2.2 is meant to answer the questions: How does missing data in the time series of a given element impact the spectral analysis results? How does adding in data that have been validated at a lower minimum count threshold impact the spectral analysis results? The counts here refer to the number of counts accumulated over the native 12-minute cycle of the SWICS detector, which comprise the data point. Including additional charge states only changes the harmonic F-test result, as shown in the table. Looking across the first to the second and third validation columns, as more charge states are included in the elemental abundance, the ∼0.5 mHz peak goes from only passing the amplitude test to passing the F-test as well. This shows that while the details of the spectral analysis for Fe change some as we adjust the validation criteria, the periodicity at approximately ~0.5 mHz is stable and largely insensitive to these adjustments. The Fe panel in Figure 2.4 shows the charge states that were included in the Fe/O composition ratio after this validation was performed on the Fe data. The Fe element time series is shown as a black dashed line and is validated and incorporated into the Fe/O composition ratio. This figure also shows the construction of all of the elemental time series considered for this event (Mg, C, O He and Fe). Each charge state is shown in a different color, as indicated in the legend for each panel. The black dotted line in each panel is the sum of the highlighted charge states — the overall element time series. Several charge states tend to dominate the behavior of each element time series and analyses similar to what is presented here for Fe were performed when validating the Mg, O and C data to ensure that the spectral analysis results were robust.

	50 cts minimum	16 cts minimum	0 cts minimum
Fe^{8+}	0% valid	81% valid	95% valid
Fe^{9+}	65% valid	100% valid	100% valid
Fe^{10+}	89% valid	100% valid	100% valid
Fe^{11+}	77% valid	100% valid	100% valid
Fe^{12+}	53% valid	99% valid	100% valid
Fe^{13+}	0% valid	72% valid	100% valid
Fe^{14+}	0% valid	44% valid	98% valid
Fe amplitude	0.54 mHz	0.53 mHz	0.53 mHz
Fe amplitude + F-test	None	0.51, 0.57 mHz	0.51, 0.56 mHz

Table 2.2: Results of validating Fe data for the central segment of the 4 March 2002 (1) ACE/SWICS event. The minimum counts threshold for the 12-minute data is relaxed allowing for more charge states to be included and for a larger percentage of the data to be validated (% valid). The counts here refer to the number of counts accumulated over the native 12-minute cycle of the SWICS detector. Spectral analysis results match when relaxing validation criteria and including additional charge states. Here, the ~0.5 mHz peak is strongly evident, despite variation in how charge states are combined or the data validation thresholds used.

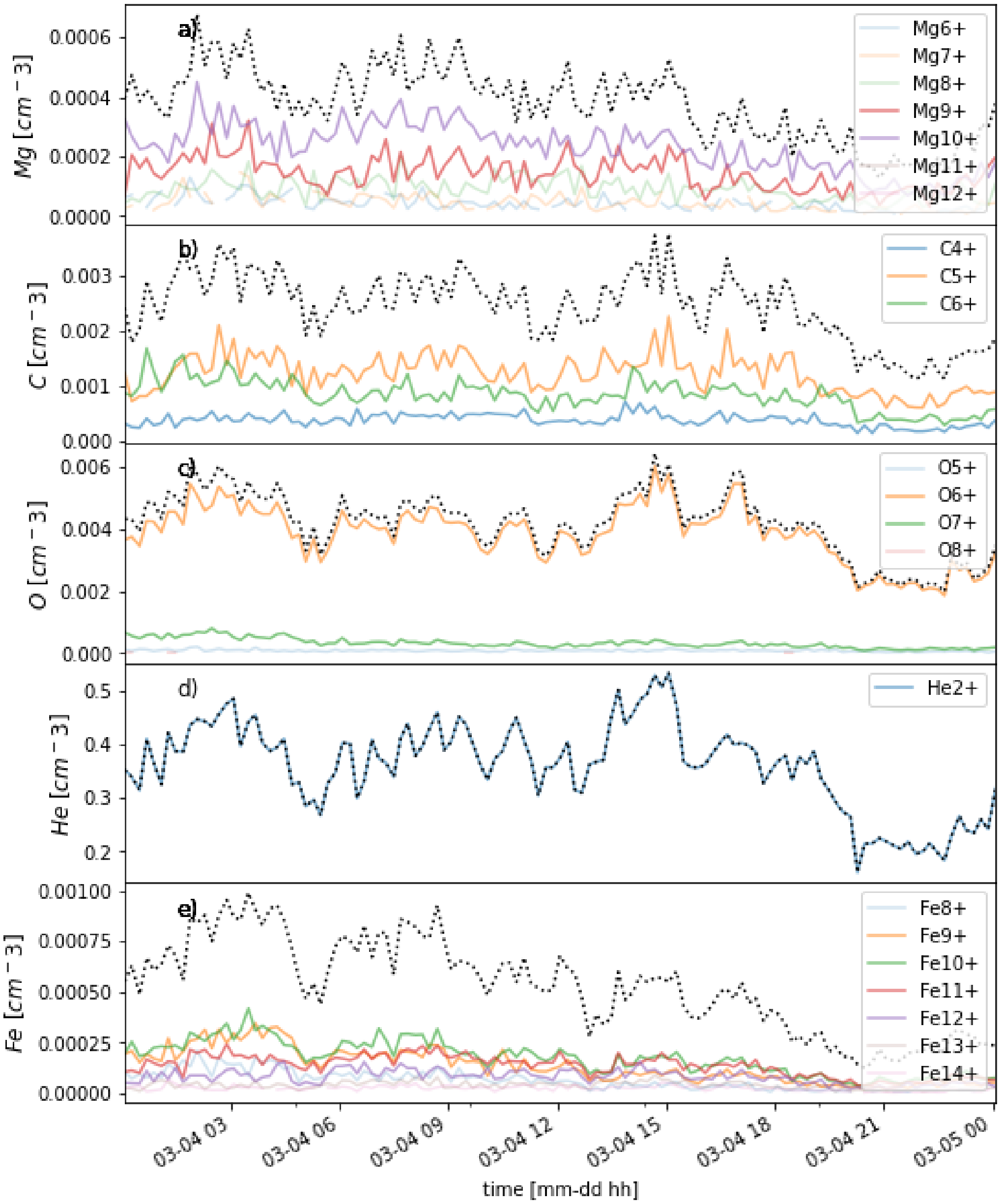

Figure 2.4: Charge state selection for the elemental composition ratio data of the 4 March 2002 (1) ACE/SWICS event. The x-axis shows time, in three-hour intervals. The y-axis shows the number density per cubic centimeter. Charge state number density time series that were included in the X/O spectral analysis run are indicated as brighter traces. The dashed line is the sum of the highlighted charge states: the overall X element time series.

2.4.2 Combined Event Analysis

We identified three additional time intervals that met the data validation thresholds and exhibited mesoscale periodic fluctuations of elemental composition and charge state ratios, namely: 27 July 2005 (2), 4 January 2004 (3), and 23 February 2004 (4). Figure 2.5 summarizes the periodic structures observed across all time segments and all four events. The black vertical dashed line marks the Nyquist frequency, determined by the SWICS sampling rate. The x-axis shows frequency in mHz. Significant discrete periodicities are marked with solid circles in colors corresponding to each event, for each 24-hour segment in the event: beginning, central and ending. Lines representing these segment types are stacked vertically for all elemental and charge state ratios. The events are labeled by the start date of their central segment and also numbered. The "o" markers on the right side of the dashed line indicate an absence of periodic structure for the segment and the "x" indicates that the segment could not be sufficiently validated due to low instrument counts. The chart shows that there are periodic structures not only during the central 24 hours of an event, but often during the 24 hours before and after as well.

For some events, the 4 March 2002 (1) event for example, the dots are aligned vertically, indicating that similar periodic structures were observed for several ratios and/or beginning, central and ending time segments. The meaning of this will be discussed in the next section. On the other hand, the detected frequencies are sometimes different for different elements and ratios, as the figure also shows. Sometimes the same periodicity persists for several 24-hour segments and sometimes it evolves. The data from each of the four events selected for this study were prepared for spectral analysis and analyzed according to the techniques described in Section 2.3 and demonstrated in Section 2.4.1.

In this section, we also show the results of a superposed epoch analysis that we performed in order to compare the evolution of the events over longer timescales than

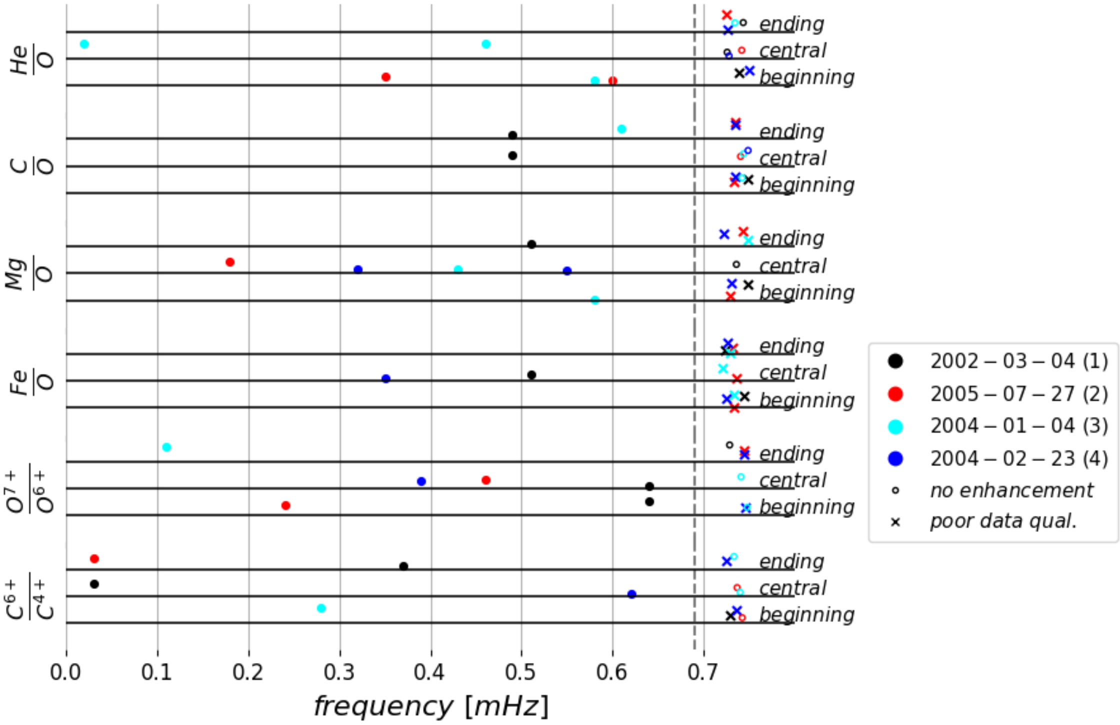

Figure 2.5: Summary of periodic structures observed in the ACE/SWICS event studies. Beginning, central and ending 24-hour time segments are processed for each elemental composition and charge state ratio. We have included analysis of the 24 hours prior to and after the central window in order to provide context. The dashed line marks the Nyquist frequency, which is determined by the SWICS sampling rate. Several events, such as the 4 March 2002 (1) event, show multiple ratios with similar periodic structure.

the periodicities examined. Specifically, we test whether the elemental composition and charge-state ratios evolve across the 72-hour window analyzed for each event. Figure 2.6 shows the overall behavior of the charge state and elemental composition ratios. Since we are focused on the overall trends for this part of the analysis, we used the SWICS 2-hour averaged composition data, for which a high percentage of the data points are validated due to higher integrated instrument counts. The segments shown here are each 24 hours long and contain the 18 - 24 hour long segments used in the spectral analysis of the high-resolution data set. Each event is labeled by the start date of the central segment, numbered and shown in a different color. The 4 March 2002 (1) event examined in the previous section is shown here in blue. The fast and slow wind average abundance values, following *Geiss et al.* (1995); *Von Steiger et al.* (2000), are overplotted here as blue and red dotted lines, respectively. The C/O observed abundance levels are the same for fast and slow solar wind types and this level is indicated by a dotted purple line in panel b). The mean value of the four event time series is plotted as a dashed black line. The x-axis shows the index of each data point, with zero marking the beginning of the central 24-hour period. The average value of each elemental composition and charge state ratio, μ, is indicated for each of the three time segments on the plot.

Similarly to what we observed in the event study, we see the Mg/O ratio, for event 1 and event 2, drop from close to a typical slow wind to a typical fast wind value. This happens pretty abruptly at the start of the central gray region. The charge state ratios, O^{7+}/O^{6+} and C^{6+}/C^{4+} in panels e and f, follow a similar trend for these two events. As in the event study, the Fe/O in panel d) transitions slowly and most of the transition happens in the gray central 24-hour segment. Note that the range spanned by the ratios in the two 2004 events, shown in red and purple, is less than the full fast to slow wind range.

Figure 2.7 shows the bulk plasma parameters, using the ACE/SWICS 2-hour resolution data, for the four events: a) proton density, b) solar wind speed, c) proton temperature and d) the magnitude of the magnetic field. The x-axis shows time in hours. The gray region marks the central 24-hour period of the events and begins at hour zero. Two of the events, the 4 March 2002 (1) event plotted in blue and the 27 July 2005 (2) event plotted in green, are stream interaction regions with high densities in the compression region. Evidence for the stream interaction can be seen in Figure 2.7: the sharp rise in the proton density near the start of the gray central period (panel a), slow rise in the solar wind speed throughout the central period (panel b) and an increase in the magnitude of the magnetic field in the central period of the event (panel d). Though our event definition criteria was not for that particular type of wind *per se*, very dense wind tends to have high count rates for the heavier elements which makes it possible for us to validate sparse data such as the Fe and Mg data.

Figure 2.8 shows the 272 eV electron distribution function by pitch angle for the full 72 hour duration of each event. The events are again labeled by the start date of their central 24-hour segment, are numbered and appear in their own panels. The y-axes in each panel show the pitch angle in degrees and the color bar indicates the magnitude of the distribution function. The x-axis shows time and the central 24-hour segment is bracketed by dashed black lines. The 4 March 2002 (1) event and the 27 July 2005 (2) event coincide with a HCS crossing, as can be seen in Figure 2.8 where the electron pitch angle changes by 180° for these two events near the start of their central segments. The He/O and C/O time series for these events, plotted in Figure 2.6 as purple and green traces, show large dips at times corresponding to the HCS crossing. Note, these two events are also SIRs. To summarize, event 4 March 2002 (1) and event 27 July 2005 (2) both exhibited large compositional trends across the 72 hours, were SIRs, and contained HCS crossings. Event 4 January 2004 (3) and event 23 February 2004 (4) had no long-term trends in the changes of composition or speed and were not associated with the HCS.

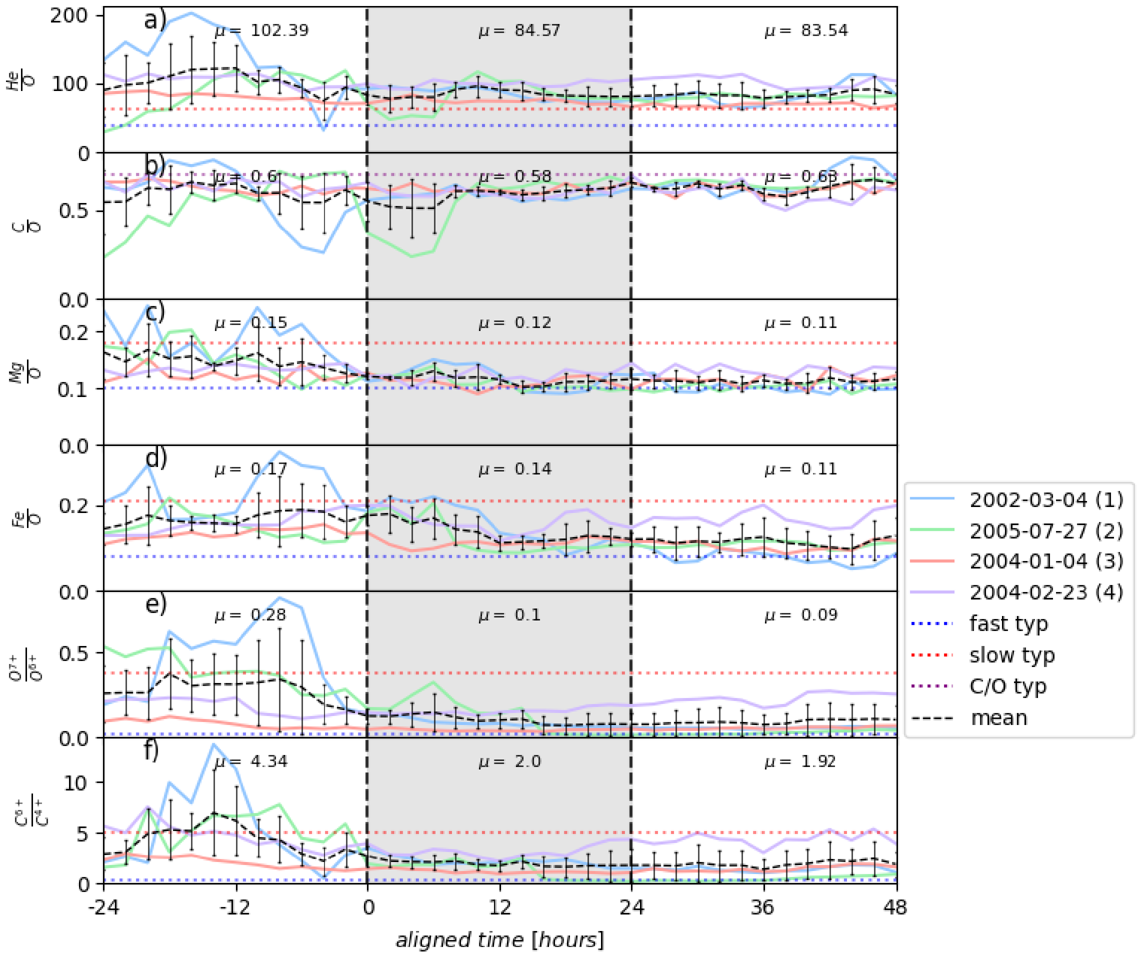

Figure 2.6: Superposed epoch analysis plots showing the overall evolution of the elemental composition and charge state ratios throughout each ACE/SWICS event. The gray segment marks the 24-hour central time window, for which there was the highest rate of validated heavy ion data, and the white regions before and after show the behavior of each time series in the 24-hour windows preceding and following it, provided for context. The central period begins at hour zero. The x-axis shows time, aligned for all events, in hours. The mean value of all events during each 24-hour segment, μ, is computed and marked on the plot.

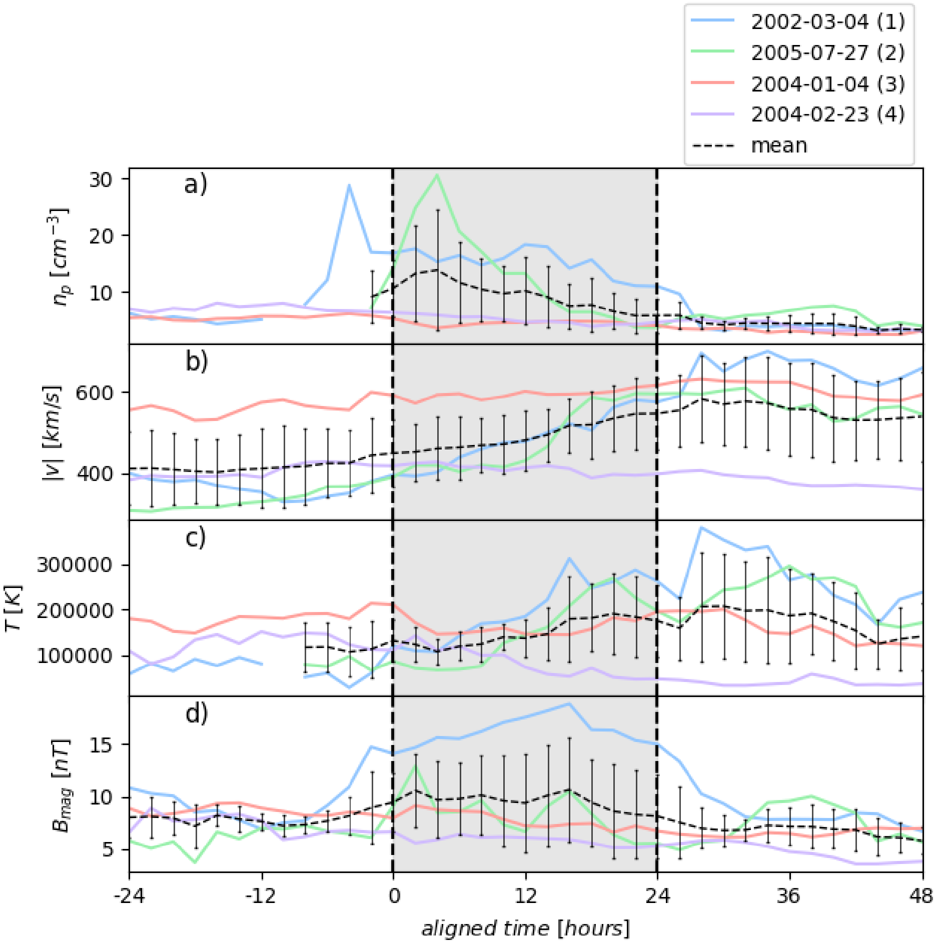

Figure 2.7: Superposed epoch analysis plots showing the overall evolution of the plasma diagnostic quantities throughout each ACE/SWICS event. The x-axis shows time, aligned for all events, in hours. The gray region marks the central 24-hour period of the events and begins at hour zero. The mean for all three events is shown as a black dashed line. Error bars indicating 1σ deviation from the mean are shown.

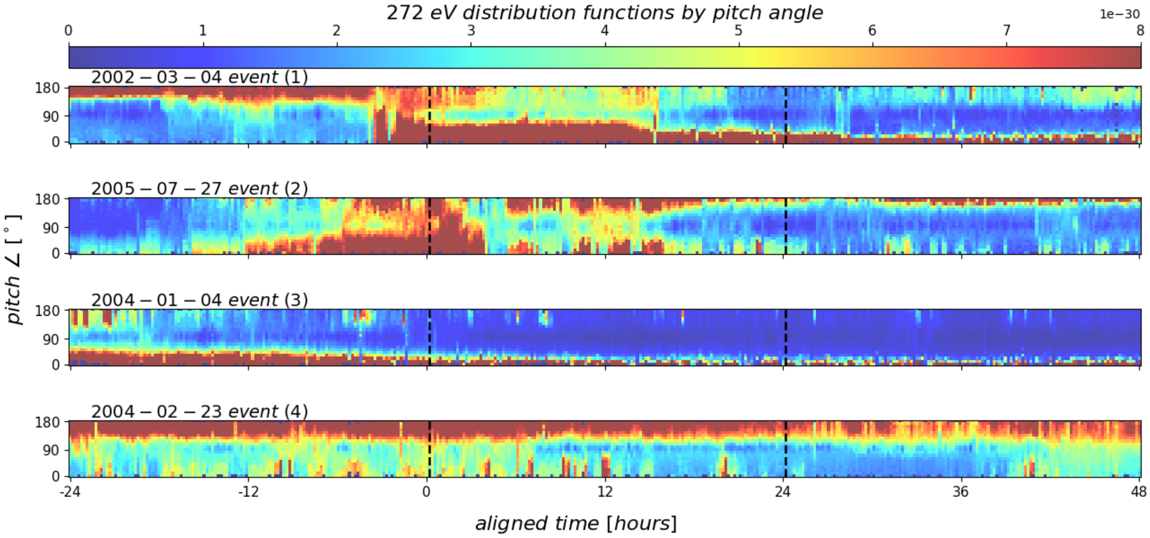

Figure 2.8: The 272 eV electron pitch angle distributions for each ACE/SWICS event. The black dashed lines mark the start and end of the central 24-hour time segment within each event. The aligned time in hours is shown on the x-axis and the y-axis indicates the pitch angle in degrees. The color bar indicates the value of the electron distribution function for each pitch angle and time. HCS crossings occur near the beginning of the central 24-hour period for the 4 March 2002 (1) and 27 July 2005 (2) events, as can be seen in the 180° change in the pitch angle.

2.5 Discussion

We have analyzed and presented here four 72-hour event windows that contain periodic structures in the elemental composition and charge state of the solar wind. These observations greatly expand upon previous work on mesoscale periodic structures in the solar wind; there has only been one other event analyzed using charge states and heavy ion data (*Kepko et al.*, 2016), which also required the use of the SWICS intrument's 12-minute native resolution in order to observe variations on "meso" scales. Here, we add four events to this list and incorporate additional elemental composition and charge state ratios into the analysis that go beyond what was available for the event in *Kepko et al.* (2016). Specifically, by looking at low-FIP elemental composition ratios as well as the O and C charge state ratios, we have been able to make observations that give insight to the possible mechanisms underlying the formation of these structures. We also examine high-FIP (He/O) and intermediate-FIP (C/O) ratios in order to compare and contrast.

The limiting factor in this analysis was the low count accumulations that the ACE/SWICS instrument could attain for the Fe and Mg number densities at the 12-minute native sampling rate. These data are particularly important in observing the behavior of the relative abundances of the low-FIP elements across the periodic events. Both the Mg/O and Fe/O composition ratios are low-FIP ratios, thus monitoring them indicates that if their abundances are elevated the source is likely to be a typical AR or QS region rather than a typical CH type location. Comparing the behavior of these ratios to the behavior of high-FIP elemental composition ratios such as He/O, intermediate-FIP composition ratios such as C/O and charge state ratios provide information about the likely solar wind interactions, such as interchange reconnection, occurring at the Sun. Combining charge states, validating and preparing these data for spectral analysis required parameter scans, manual visual inspection and some judgement calls. The need to perform spectral analysis places a stringent requirement on the data that one can use. We require 24 hours of nearly continuous data, since validating a significantly shorter time segment is not sufficient to compute robust spectra with the necessary spectral resolution. The data that could be validated by these means determined event selection and had important implications for the density of the plasma observed.

Two of the events presented here were SIRs, likely because their increased density enabled higher count rates and thus easier to validate Fe and Mg data. Selection criteria aside, these are an interesting class of events to consider as the observed periodicities in elemental composition and charge state capture real information about processes occurring in the Sun. These two events also occurred near a HCS crossing, which is in line with the previous work reporting periodic structure in the C/O ratio occurring near a HCS crossing (*Kepko et al.*, 2016) and consistent with the observation of periodic structures on these scales observed in and around helmet streamer tips and also associated with the HCS (*Viall et al.*, 2010; *Viall and Vourlidas*, 2015a).

The structures found in all four events, observed *in situ*, are indicators of elemental and ion composition variations being imprinted onto the solar wind from the solar atmosphere. The magnetic field variations during the periods we present here do not exhibit a one-to-one correlation to the variations in elemental composition and charge state. Therefore, we can rule out Kelvin-Helmholtz instability across the stream interface or other boundary wave phenomena (*Crooker et al.*, 1996) as being the underlying mechanism of formation. We performed a superposed epoch analysis in order to determine whether there were commonalities across the 72-hour event studies but found that there were not, aside from the presence of periodic structures. Nevertheless, plotting the four events together on one plot was a good way to compare and contrast their properties. For the 4 March 2002 (1) and 27 July 2005 (2) events, we see similarities: a slower wind with an enhanced abundance of low-FIP elements and high charge state in the beginning segment is overtaken by a faster wind with less of an enhanced abundance of low-FIP elements and lower charge states. The 4 January 2004 (3) and 23 February 2004 (4) events show fairly steady solar wind speeds, the former being fast and the latter remaining slow throughout the 72 hours. The 4 January 2004 (3) event exhibits a similar three-day trend to the SIR events, though smaller in amplitude. The 23 February 2004 (4) event does not exhibit a three-day trend in either direction with regard to the elemental and ion composition. These events highlight the fact that the solar wind types are characterized by a complex combination of their composition signatures as well as their speeds. This has been reported by *Zurbuchen et al.* (2002) and what we see in these four events is consistent with the report. Solar wind categorization cannot be considered to be strictly binary (*Zurbuchen et al.*, 2002; *Stakhiv et al.*, 2015; *Roberts et al.*, 2020).

As noted earlier, a HCS crossing occurs at the beginning of the central window in two of the events: 4 March 2002 (1) and 27 July 2005 (2). At these times, a drop in the He/O composition ratio is observed. This is in line with He depletions previously reported near the HCS (*Borrini et al.*, 1981; *Suess et al.*, 2009). The behaviour of the He/O ratio also exemplifies a wind elemental composition that is complex and non-binary. The 4 March 2002 (1) event exhibits a high He/O ratio that decreases in the central and ending segments. The other three events do not exhibit strong trends in He across the three days. In all four cases, the abundance is higher than the slow streamer wind levels from *Geiss et al.* (1995); *Von Steiger et al.* (2000) for the entire 72-hour duration. Neither of the SIR events (events 1 and 2) follow the speed-He abundance correlation found for long-term averages by *Kasper et al.* (2007).

We examine the events in the context of what is known about the composition of different types of source regions of the solar atmosphere and how they interact. Interchange reconnection (*Fisk*, 2003; *Antiochos et al.*, 2011; *Crooker et al.*, 2002) between closed magnetic field regions and open magnetic field lines is one possible explanation for how periodic structures enter the solar wind (*Kepko et al.*, 2016; *Viall* *et al.*, 2009b; *Réville et al.*, 2020; *Di Matteo et al.*, 2019; *Viall and Vourlidas*, 2015b; *Higginson and Lynch*, 2018). The S-Web model (*Antiochos et al.*, 2011) predicts that interchange reconnection occurs at the magnetic open-closed boundary, the boundary between closed loops and magnetic field lines open to the heliosphere, which is consistent with what we observe. In the interchange reconnection model, low-FIP enhanced and high charge state enhanced plasma builds up in the closed magnetic field regions. Additionally, gravitational settling in large closed magnetic field loops may cause heavier ions to be depleted. Gravitational settling makes the observations mass dependent due to heavy ions sinking to the bottom and lighter elements escaping first. An in-depth treatment of this topic can be found in *Endeve et al.* (2005). If these closed loop regions periodically reconnect with open field lines, they could create the observed periodic changes in the elemental and ionic composition. Similar observations were reported by *Kepko et al.* (2016). While there are ideas as to how periodicities could be created at the Sun (*Réville et al.*, 2020; *Pylaev et al.*, 2017), many more events are needed to thoroughly investigate those mechanisms.

Figure 2.5 shows that several elemental composition and/or charge state ratios exhibit similar behavior in the frequency domain during a given event. In the 27 July 2005 (2) event, the low-FIP Mg/O ratio and O^{7+}/O^{6+} charge state ratio exhibit comparable periodicities at approximately 0.2 mHz. The 23 February 2004 (4) event shows similar, though slightly shifted, periodic structures in the Fe/O, Mg/O, and O^{7+}/O^{6+} ratios all occurring within the 0.3 – 0.4 mHz range. The fact that the low-FIP elemental composition and charge state ratios behave similarly during these events is consistent with periodic interchange reconnection being the underlying mechanism, occurring at the corona and periodically releasing closed-field plasma into the heliosphere (*Kepko et al.*, 2016; *Sanchez-Diaz et al.*, 2019a).

The 4 March 2002 (1) event shows very similar periodic structures in the Fe/O, Mg/O and C/O composition ratios. The 4 January 2004 (3) event shows comparable structures for the Mg/O, C/O and He/O ratios. These events feature more complex interactions than do events 2 and 4. We expect the Fe/O and Mg/O ratios to behave similarly as both Fe and Mg are heavy, low-FIP elements.

The behavior of the He/O composition ratio, if governed by the FIP effect only, might be expected to differ from the behavior of low-FIP ratios such as Mg/O during the 4 January 2004 (3) event. Recall that He is a very high-FIP element. However, He abundances are well known to be only partially explained by the FIP effect, and gravitational settling is likely to be playing a role as well (*Laming*, 2015). He abundances are modulated by the large-scale global coronal magnetic field topology (*Moses et al.*, 2020), including the presence or absence of active regions (*Kasper et al.*, 2007).

The fact that the C/O ratio behaves similarly to the low-FIP ratios in events 1 and 3 may be explained by the fact that C is an intermediate-FIP element with a FIP of just over 10 eV – it follows the behavior of high-FIP elements when fractionation occurs in closed-field loops but can behave like the low-FIP elements if fractionation occurs at the origin of an open-field area (*Laming et al.*, 2019). The *in situ* solar wind is a mixture of plasma that originates from both closed- and open-field regions and the nature of the mixture depends on the details of the reconnection event. Due to this, the C/O ratio may match the behavior of low-FIP elemental composition ratios as seen in Figure 2.5 for the 4 March 2002 (1) and 4 January 2004 (3) events. The variation in composition, produced by processes in the solar atmosphere, is the commonality among all four events. The different manifestations of these variations highlight the complex, multi-step processes involved in the formation of these mesoscale structures.

2.6 Summary

Four events containing mesoscale periodic structure in the solar wind's elemental composition and charge state were extracted from the ACE/SWICS 12-minute data set, validated, analyzed and examined within the context of spectral analysis. The common feature among all four events is the temporal variation in composition. Such variation can only have been produced in the solar atmosphere and therefore provides important constraints on the formation mechanisms responsible. The differences in the variations observed highlight the complexity of the multi-step processes involved in the creation of these mesoscale structures.

The events were selected based on the quality of the Mg and Fe number density data, which typically accumulate low counts at the 12-minute ACE/SWICS native resolution, in order to test whether the presence and value of periodicities is dependent on the FIP of the element or the charge state ratio. The results showed that events 4 March 2002 (1) and 27 July 2005 (2) occurred during a HCS crossing and were SIRs, with the expected drop in the He/O ratio. The 4 January 2004 (3) event did exhibit the same general trend of decreasing low-FIP abundance and charge-state as did the two SIRs and HCS events over the 72 hours examined, but the 23 February 2004 (4) event did not exhibit much of an overall trend in elemental and ion composition throughout the time span of the event.

The periodic structures observed in these events also captured interesting relationships as described and discussed in Sections 3.3 and 3.4 and summarized here. In the 27 July 2005 (2) and 23 February 2004 (4) events, for example, we see one or more low-FIP ratios and a charge state ratio behave comparably in terms of the periodic signals observed, suggesting that interchange reconnection may be the process responsible for these structures. In the 4 March 2002 (1) event, the low-FIP ratios (Mg/O and Fe/O) contain a similar periodic structure as does C/O. The 4 January 2004 (3) event shows the Mg/O, He/O and C/O composition ratios containing closely-matched periodic structures. This suggests a more complex interaction for the He/O and C/O ratios than a simple picture where all closed loops have low-FIP enhanced ratios that are constant in time, but these interactions can also be explained by the interchange reconnection model as detailed in Section 3.4.

We have greatly expanded upon all previous work reported about periodic structures in solar wind elemental composition and charge state (*Kepko et al.*, 2016). The techniques presented here can be directly applied to data from new, higher-resolution instruments, such as Solar Orbiter's Heavy Ion Sensor (HIS) with its 90-second resolution composition data, in order to extract greater insight into the source mechanisms as well as to determine the spatial and temporal nature of the variation involved. While the event identification in this study was limited by our strict requirement on Mg and Fe count rates, periodic structures in C, O, their charge state ratios, and He/O appear to be common in the ACE/SWICS 12-minute data set. Future work will be to expand upon these four events and to compute statistics on the periodic mesoscale structures identified in the entire 14 years of the validated ACE/SWICS 12-minute data.

CHAPTER III

Distributions of Mesoscale Periodic Structures in the Composition of the Solar Wind

3.1 Background

In this chapter we present the results of a statistical study of periodic variations that have previously been observed in the ionic and elemental composition of the solar wind (*Kepko et al.*, 2016; *Viall et al.*, 2009a; *Gershkovich et al.*, 2022). Composition is a particularly important tracer of solar wind formation as variations in the elemental composition and charge state are established in the solar atmosphere and do not evolve en route to the point of observation. This is due to processes occurring in different regions on the Sun producing different elemental and ion fractionation that are preserved as the plasma is expelled at supersonic speeds (*Ogilvie et al.*, 1980), resulting in the collision-less nature of the solar wind beyond the freeze-in radius of $\sim 1.1 - 4\ R_s$, depending on the element (*Hundhausen et al.*, 1968).

In situ observations of the solar wind have shown that it is not laminar but instead highly structured at a variety of scales (*Viall et al.*, 2021b; *Verscharen et al.*, 2019). These scales range from 1–2 minute magnetic holes (*Winterhalter et al.*, 1994) to very large-scale structures such as coronal mass ejections and stream interaction regions (*Kilpua et al.*, 2017; *Richardson*, 2018). On mesoscales, scales that are larger than kinetic scales but smaller than the largest structures in the solar wind (∼10–10000 Mm or, alternatively, on timescales of several minutes to several hours), some structures enter the solar wind during formation in the solar atmospheres while others evolve during propagation through the heliosphere. The structures that enter the solar wind directly at the Sun and persist until they are measured retain key information about the processes that form the solar wind. Mesoscale structures not only capture signatures of solar wind formation but are also significant because they can drive magnetosphere dynamics (*Di Matteo et al.*, 2022) and shape the medium through which large space weather events propagate. Structures at these scales have been observed in Solar Terrestrial Relations Observatory (STEREO) white light remote images down to the resolution of the instrument (*DeForest et al.*, 2018; *Viall and Vourlidas*, 2015a). Magnetic flux rope structures as small as 50 Mm (*Murphy et al.*, 2020) have been detected *in situ* and structures in plasma density have been observed at scales ranging from 50 and 2,000 Mm (*Stansby and Horbury*, 2018). Mesoscale structures have also been identified in combinations of plasma and magnetic signatures (*Borovsky*, 2008; *Di Matteo et al.*, 2019; *Rouillard et al.*, 2010, 2020; *Sanchez-Diaz et al.*, 2019b).

Quasi-periodic proton density structures (PDSs) are a subset of mesoscale solar wind structures. These were first discovered in event studies that showed a direct relationship between mHz range magnetic oscillations in the magnetosphere (several minute to several hour temporal scales) and discrete frequencies in the upstream solar wind density (*Kepko et al.*, 2002b; *Kepko and Spence*, 2003). Multiple event studies have shown that there are direct links between periodic structures observed in solar wind proton number density and periodicities in the magnetosphere in radar (*Fenrich and Waters*, 2008), ionospheric (*Dyrud et al.*, 2008) and ground magnetometer (*Villante et al.*, 2007; *Villante and Tiberi*, 2016) data at frequencies ranging from ∼0.2 mHz to ∼4 mHz. *Viall et al.* (2009a) found similar statistically significant frequencies, ranging from ∼0.5 mHz to ∼4 mHz, observed in 11 years of Wind proton density data, measured near Lagrange point 1 (L1), as well as in dayside Geostationary Operational Environmental Satellites (GOES) magnetometer data.

Since the initial discovery of periodic density structures in the solar wind, there have been efforts to categorize them and to identify their source. *Viall et al.* (2008), *Viall et al.* (2009a) and *Kepko et al.* (2020) reported statistically significant bands of periodic structures in solar wind proton density measurements. These structures exhibit a characteristic scale such that certain periodicities occur more than others during the observational period and therefore cannot simply be attributed to turbulence. Several lines of evidence indicate that periodic variations carry signatures of the solar wind formation processes. *In situ* measurements of composition, magnetic field and strahl (the direction of electron flow relative to the direction of the magnetic field) variations point to magnetic reconnection events that could only have originated at the Sun during solar wind release and acceleration (*Kepko et al.*, 2016; *Di Matteo et al.*, 2019; *Viall et al.*, 2009a). Anisotropic temperature changes were found within PDSs that are not observed near L1 in Helios data by *Di Matteo et al.* (2019). These were consistent with formation in the solar atmosphere and temperature isotropization in transit. PDSs identified in STEREO/Sun Earth Connection Coronal and Heliospheric Investigation (SECCHI) white light image data are found at distances as close to the Sun as 2.5 R_s and are observed to be accelerating with the surrounding solar wind (*DeForest et al.*, 2016, 2018; *Viall and Vourlidas*, 2015a; *Viall et al.*, 2010). *Rouillard et al.* (2020) tracked large streamer blobs containing approximately hour-long structures from STEREO/SECCHI to their arrival at the Parker Solar Probe, thus linking periodic structures observed in images to *in situ* observations. The above findings show that the solar wind is often formed and released via quasi-periodic mesoscale density structures and highlights the importance of extending the statistical studies of such structures to properties of the solar wind such as its composition.

In this Chapter, we move beyond statistical studies of proton density structures to studies of periodic density structures observed in the charge state and elemental composition of the solar wind, measured at L1 by the Solar Wind Ion Composition Spectrometer aboard the Advanced Composition Explorer spacecraft (ACE/SWICS) at its native 12-minute resolution. For the first time, we provide occurrence distributions of statistically significant frequencies found in the relative abundances of elements with low first ionization potential (FIP), intermediate-FIP, high-FIP as well as in the charge state. These are particularly relevant as the elemental composition and charge state are determined in the solar atmosphere and do not evolve, thus providing important constraints on the processes that govern solar wind formation. Our distributions cover a frequency range between ∼0.1 mHz to ∼0.7 mHz, near the lower bound of the periodic proton density structures identified by previous studies at L1 due to the longer 12-minute native resolution of the ACE/SWICS instrument. This study covers a time span of 14 years (1998–2011) and explores the impact of solar cycle dependencies on the periodicities identified. We find statistically significant periodic enhancements in the composition data and that these enhancements occur more at some frequencies than others, thus exhibiting a characteristic scale.

3.2 Methodology

We validate and prepare 14 years (1998-2011) of ACE/SWICS heavy ion composition time series data in order to conduct a statistical study of the mesoscale periodic structures that it contains. Fundamentally, we use a similar spectral analysis technique to what was used for statistical studies of proton density structures (*Kepko et al.*, 2020; *Viall et al.*, 2008) and for event studies of periodic structures found in heavy ion abundance data (*Gershkovich et al.*, 2022). We analyze charge state abundance ratios (O^{7+}/O^{6+} and C^{6+}/C^{4+}), low-FIP (Fe/O, Mg/O and Si/O), intermediate-FIP (C/O and S/O) and high-FIP (He/O) relative abundance values in order to compare and contrast their distributions of mesoscale periodic structure occurrences. The 14-year data set is partitioned into non-overlapping 24-hour nominal segment lengths. Each 24-hour window is prepared according to the criteria given below and examined for periodicity independently. Furthermore, we split the resulting frequency occurrence distributions into groups by solar activity (with years selected for high, medium and low average sunspot number) in order to determine the effect of solar activity on the number (normalized to the number of validated for that category) and values of the periodic structures identified.

We require that all signals in the statistical study pass both the amplitude test and the harmonic F-test at a 90% confidence level in order to ensure robust results. Section 1.8 provides an overview of the spectral analysis procedure performed.

Before running the spectral analysis procedure on each 24-hour window, the time series segment is prepared by validation, despiking and re-sampling routines. This is done in order to account for missing data, uneven sampling and outliers. The re-sampling and removal of outliers are necessary as time series must be sampled to a common time-step under the assumptions of spectral analysis and outliers can cause ringing in the spectra. We chose 24-hour window lengths in order to ensure that there are enough data points (nominally 120) to run spectral analysis with sufficient spectral resolution. The segments are de-spiked by removing outliers that exceed a 5σ threshold above a rolling window averaged version of the time series using a window size of twelve data points. All data segments were re-sampled to a 12-minute time-step prior to performing the spectral analysis as in (*Gershkovich et al.*, 2022).

We have set the following minimum requirements on the time series in order to make sure that each segment analyzed for periodicity has sufficient continuity and counts: 1) We require that the percentage of missing data points must not exceed 20% for each segment. 2) The number of allowed adjacent missing data points must be less than 3. 3) We require a minimum of 25 ACE/SWICS instrument counts for each data point in the time series to be validated. These criteria must be met for all segments and ratios included in the study.

3.3 Results

3.3.1 Distributions: Statistical Significance and Characteristic Scale

We prepared and ran all segments of the 1998–2011 ACE/SWICS data according to the analysis procedure described in Section 3.2. Figures 3.1 – 3.4 show the resulting occurrence distributions for the charge state, low-FIP, intermediate-FIP and high-FIP ratios with a bin width of $3f_{Ray}$, the maximum resolution of this method with 3 applied tapers. These distributions are computed with the data for all categories of solar activity (the full data set). Each ratio is shown in its own panel within each figure. The dotted horizontal line in each panel indicates the expected false positive rate of the combined amplitude test and harmonic F-test for that distribution, with each test passed at the 90% confidence level. The extreme low and high frequency ranges shaded in red on each plot indicate frequency bins prone to false positives according to Monte-Carlo simulations based on the bending power law (BPL) background assumption (*Di Matteo et al.*, 2021) and are therefore not considered as statistically significant results. The error bars on the distributions are estimated by bootstrapping (*Efron and Tibshirani*, 1994) and indicate a 2σ deviation. Statistically significant frequencies are labeled in black with their numerical values in units of mHz; these are required to rise $\geq 2\sigma$ above the line designating the expected false positives rate of the spectral analysis method. The black curve in each panel is the kernel density estimation (KDE) to the distribution computed using a Gaussian Kernel and "Scott's Rule" (*Scott*, 2015) as the method for selecting the bandwidth parameter. Points that rise 1σ above the KDE estimator are marked with a blue "x" and considered to indicate that a characteristic scale is present, meaning that certain frequencies are enhanced relative to the overall distribution shape.

Figure 3.1 shows an all-year distribution for He/O that rises at an increasing rate with frequency. The statistically significant frequency band (i.e., frequencies rising 2σ above the false positives rate) ranges from $\sim$0.4–0.6 mHz (corresponding to approximately 30-minute periodicities). The 0.61 mHz enhancement is considered to be a characteristic scale in this distribution. Figure 3.2 shows distributions for C/O and S/O, the intermediate-FIP abundances. The S/O ratio has too few results to be considered robust as it has bootstrapped 2σ error bars that are comparable in size to the number of occurrences in each bin, though the 0.27 mHz signal may be substantial. The C/O distribution rises steadily, in an almost linear way with frequency. It has a broader range of statistically significant frequencies than the He/O distribution, spanning almost the entire frequency range in consideration: $\sim$0.1–0.6 mHz. Figure 3.3 shows the Mg/O, Fe/O and Si/O low-FIP distributions which, like the C/O intermediate-FIP distribution, also seem to rise linearly with frequency. Mg/O and Si/O have a wide, continuous range of significant frequencies ($\sim$0.2–0.6 mHz) while the significant frequencies of the Fe/O distribution are separated into three distinct bands at $\sim$0.3, 0.4 and 0.6 mHz. The charge-state ratios, shown in Figure 3.4, have similar shapes to the low-FIP and intermediate-FIP distributions and a similar range of statistically significant frequencies. The oxygen charge-state distribution is very similar to the low-FIP ratio distributions in both shape and bin counts. The carbon charge-state ratio distribution is sparse and the bootstrapped 2σ error bars indicate a high degree of uncertainty.

It can be seen that all abundance ratios with adequate statistics contain significant frequencies ranges that rise well above the expected false positives rate of our method. A characteristic scale or scales can be seen for Fe/O, Mg/O, C/O, He/O O^{7+}/O^{6+} as blue dots indicating enhancements of 1σ of the bootstrapped distribution above the

KDE curve for the distribution. The 0.5-0.6 mHz range tends to exhibit the most common enhancement for all abundance ratios.

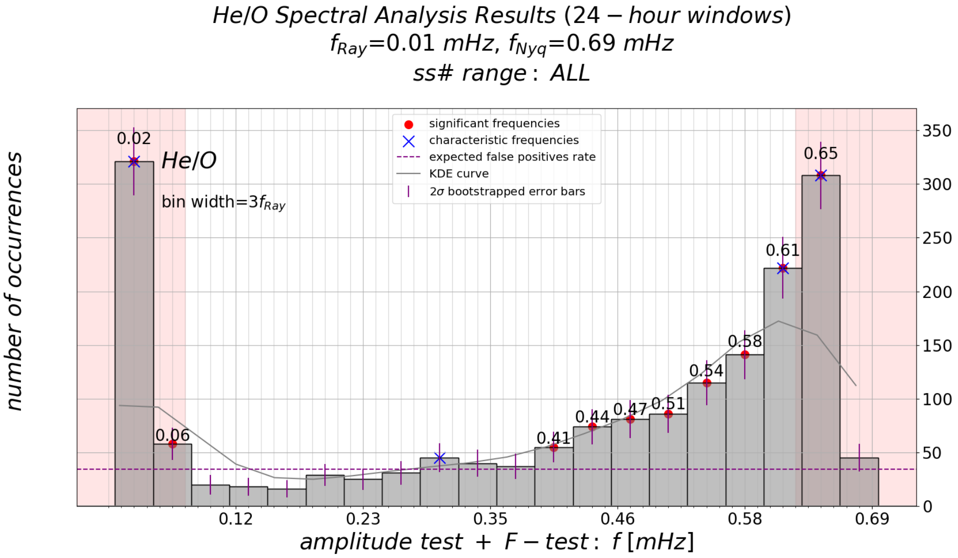

Figure 3.1: Periodic density structure occurrence distribution for the high-FIP He/O abundance ratio. Error bars showing 2σ of the bootstrapped distribution are plotted as solid, purple vertical lines. The occurrence distribution is shown in gray and the expected false-positives rate for the method is shown as a dotted, purple horizontal line. Significant frequencies are defined to rise $\geq 2\sigma$ above the expected false-positives rate. These are marked on the plot by a red dot and the numerical value of the corresponding bin center. Characteristic frequencies are defined to rise $\geq 1\sigma$ above the gray KDE curve and are marked with a blue "x". The extreme low and high frequency ranges shaded in red on each plot indicate frequency bins prone to false positives, according to Monte-Carlo simulations (*Di Matteo et al.*, 2021), and are therefore not considered as statistically significant results.

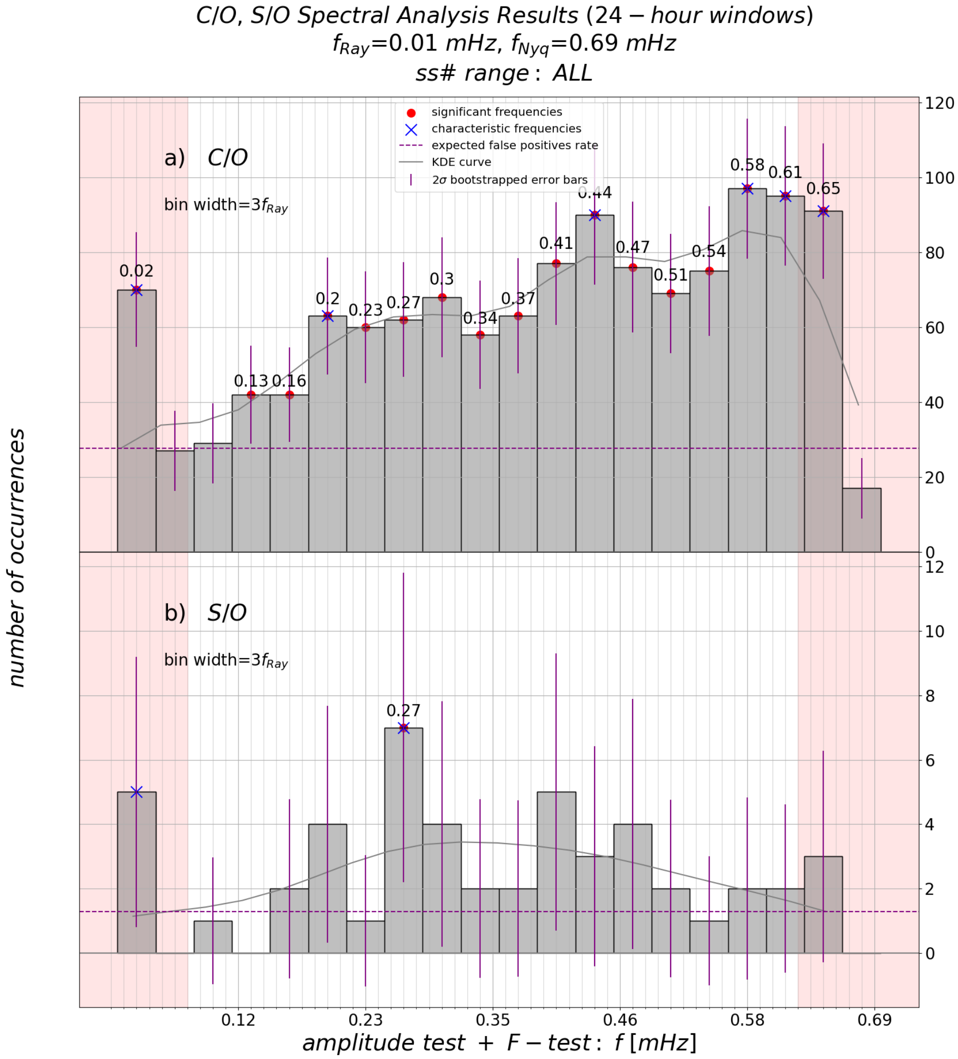

Figure 3.2: Periodic density structure occurrence distributions for the intermediate-FIP composition ratios (C/O and S/O). Error bars showing 2σ of the bootstrapped distributions are plotted as solid, purple vertical lines. The occurrence distributions are shown in gray and the expected false-positives rate for the method is shown as a dotted, purple horizontal line. Significant frequencies are defined to rise $\geq 2\sigma$ above the expected false-positives rate. These are marked on the plot by a red dot and the numerical value of the corresponding bin center. Characteristic frequencies are defined to rise $\geq 1\sigma$ above the gray KDE curve and are marked with a blue "x". The extreme low and high frequency ranges, shaded in red on each plot, indicate frequency bins prone to false positives, according to Monte-Carlo simulations (*Di Matteo et al.*, 2021), and are therefore not considered as statistically significant results.

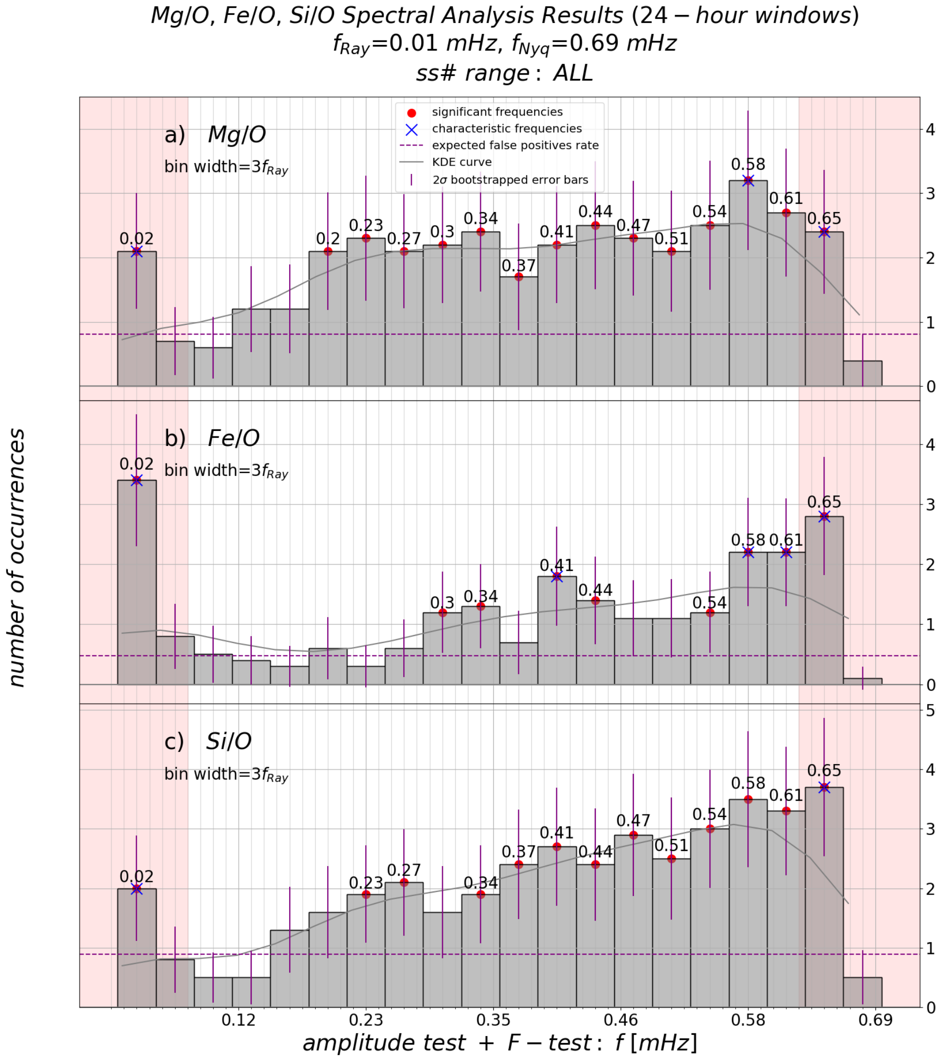

Figure 3.3: Periodic density structure occurrence distributions for the low-FIP composition ratios (Mg/O, Fe/O and Si/O). Error bars showing 2σ of the bootstrapped distributions are plotted as solid, purple vertical lines. The occurrence distributions are shown in gray and the expected false-positives rate for the method is shown as a dotted, purple horizontal line. Significant frequencies are defined to rise $\geq 2\sigma$ above the expected false-positives rate. These are marked on the plot by a red dot and the numerical value of the corresponding bin center. Characteristic frequencies are defined to rise $\geq 1\sigma$ above the gray KDE curve and are marked with a blue "x". The extreme low and high frequency ranges, shaded in red on each plot, indicate frequency bins prone to false positives, according to Monte-Carlo simulations (*Di Matteo et al.*, 2021), and are therefore not considered as statistically significant results.

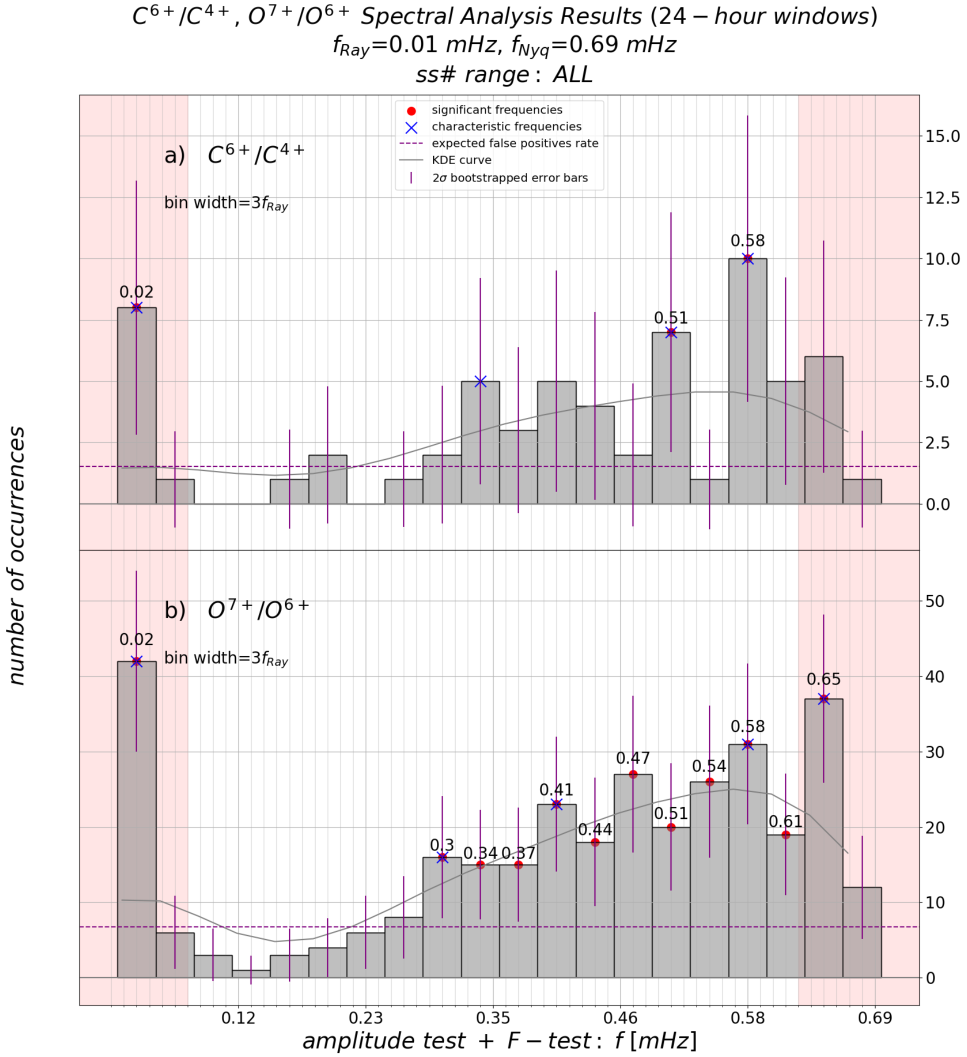

Figure 3.4: Periodic density structure occurrence distributions for the charge-state ratios (C^{6+}/C^{4+} and O^{7+}/O^{6+}). Error bars showing 2σ of the bootstrapped distributions are plotted as solid, purple vertical lines. The occurrence distributions are shown in gray and the expected false-positives rate for the method is shown as a dotted, purple horizontal line. Significant frequencies are defined to rise $\geq 2\sigma$ above the expected false-positives rate. These are marked on the plot by a red dot and the numerical value of the corresponding bin center. Characteristic frequencies are defined to rise $\geq 1\sigma$ above the gray KDE curve and are marked with a blue "x". The extreme low and high frequency ranges, shaded in red on each plot, indicate frequency bins prone to false positives, according to Monte-Carlo simulations (*Di Matteo et al.*, 2021), and are therefore not considered as statistically significant results.

3.3.2 Dependence on Solar Activity

Figure 3.5 shows the average sunspot number for the 14 years of the study. For the purposes of this analysis, we categorize the solar activity by grouping years with low (years 2005–2010), medium (years 1998, 2003, 2004, 2011) and high (years 1999–2002) average sunspot number and analyzing them together. We also look at the group of all years and analyze the full 14-year data set. Figure 3.6 shows the fraction of validated segments that contained one or more results for each ratio analyzed. The error bars represent 1 standard deviation and were generated from the bootstrapped distributions. This plot shows that the fraction of validated windows containing significant frequencies is fairly consistent for low, medium and high solar activity levels (as measured by the average sunspot number for a given year) as has been reported for protons (*Kepko et al.*, 2020; *Viall et al.*, 2008). From top panel to bottom panel we show the result rate for the high-FIP ratio (He/O) in panel a), the intermediate-FIP ratios (S/O and C/O) in panel b), low-FIP ratios (Mg/O, Si/O and Fe/O) in panel c), and charge-state ratios (C^{6+}/C^{4+} and O^{7+}/O^{6+}) in panel d). The y-axis in each panel shows the fraction of validated windows containing at least one result. The x-axis shows categories of average sunspot number: low, medium, high, and all years.

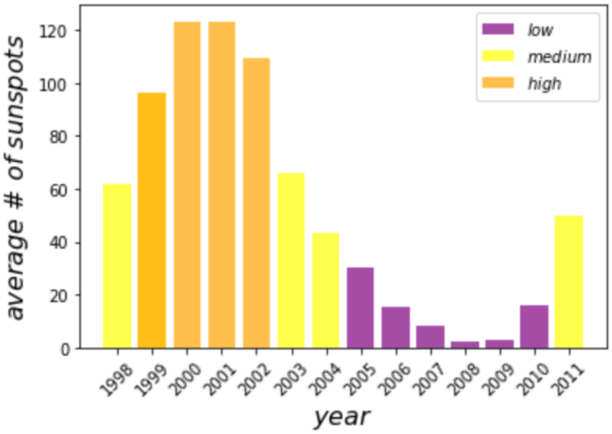

Figure 3.5: Solar activity during the 14 years of ACE/SWICS data analyzed (as measured by average yearly sunspot number).

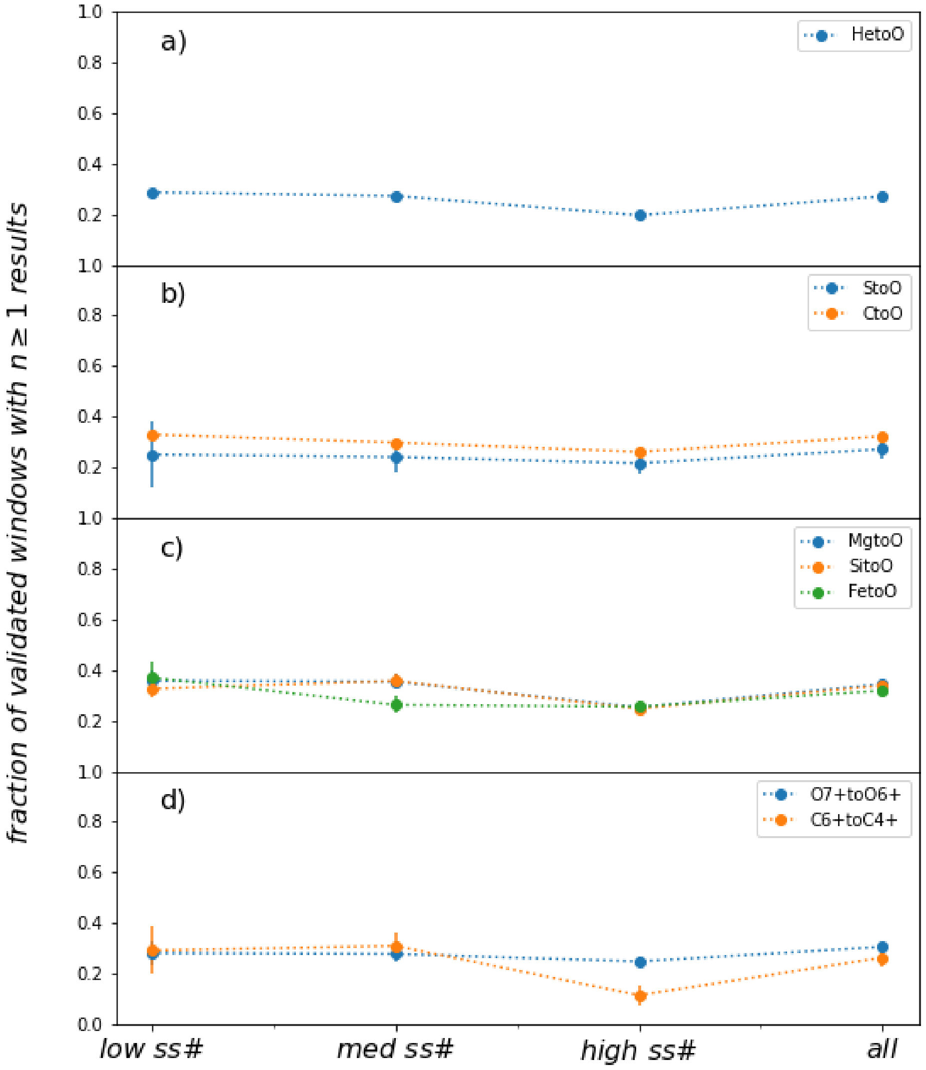

Figure 3.6: Solar cycle dependence of the fraction of validated windows that contained at least one statistically significant result passing both the harmonic F-test and amplitude test at a 90% confidence level. The result rates are fairly consistent throughout the solar cycle for all composition and charge-state abundances. The error bars represent 1σ of the bootstrapped distributions. The number of validated windows and results was low for the years corresponding to low solar activity, and thus the error bars are large.

3.4 Discussion

We have, for the first time, presented here occurrence distributions of statistically significant periodic structures identified in the elemental and charge state composition of the solar wind. As in the statistical studies of proton density structures in the solar wind (*Kepko et al.*, 2020; *Viall et al.*, 2008), we see that periodic structures also exist at statistically significant levels in the elemental composition and charge state relative to the expected false positives rate for our spectral analysis procedure (see Figures 3.1-3.4). The same figures also show that characteristic frequencies are present in most occurrence distributions (as evidenced by the peaks rising $\geq 1\sigma$ above the smoothed histograms). Mesoscale periodic structures, in general, are strongly associated with the formation and release of the solar wind. Periodic structures in elemental composition and charge states are particularly important tracers of these processes as they are determined in the solar atmosphere and do not evolve en route to the observing instrument.

Figures 3.1-3.4 also show that the low-FIP, intermediate-FIP and charge state distributions have a wider range of significant frequencies, extending to lower values, and exhibiting different shapes than the high-FIP (He/O) distribution. Among the low-FIP distributions, Fe/O stands out from Mg/O and Si/O in that, rather than exhibiting a continuous range of statistically significant frequencies, it shows three narrower bands at approximately 0.3, 0.4 and 0.6 mHz. Mg/O and Si/O look very similar to each other and all three low-FIP distributions have a similar number of total results. The differences observed for Fe/O are likely due to gravitational settling as Fe has a much higher mass than either Mg or Si. Gravitational setting in large, closed magnetic loops may introduces mass-dependent effects due to heavy ions sinking and lighter elements escaping first (*Weberg et al.*, 2012).

Figure 3.7 shows a summary of the periodic structures identified for low-FIP, intermediate-FIP, high-FIP and charge state ratios. Significant frequencies are shown for the full data set, as well as for high, medium and low sunspot number year groupings. Statistically significant frequencies ($\geq 2\sigma$ above the expected false positives rate line in Figures 3.1-3.4) are shown as color-coded circles, in a different color for each ratio. Characteristic frequencies ($\geq 1\sigma$ above the KDE curve for the distributions in 3.1-3.4) are marked with an "x". Results with large statistical uncertainty are grayed out. Though there was not a strong dependence on solar activity in the number of validated windows with one or more results, the values of significant and characteristic frequencies do seem to exhibit some dependence. For example, the 0.35 mHz band seems to be most prevelant in low sunspot number years, declining in medium, and not present much in high sunspot number years. The opposite is true of the 0.55 mHz band. He/O ratio exhibits a different shape from the other abundances, likely due to the fact that He is governed by different drivers than are the other elements (*Laming*, 2015; *Laming et al.*, 2019). The high-FIP (He/O) and intermediate-FIP (C/O) ratio significant frequencies are fairly stable for the four categories of solar activity. The low-FIP statistically significant results seem to vary erratically. This is likely due to the fact the He and C abundances are much more prevalent in the solar wind and that the statistics available for the heavier ions are marginal during periods of low solar activity. The distributions used to generate this summary chart are given in Appendix A.

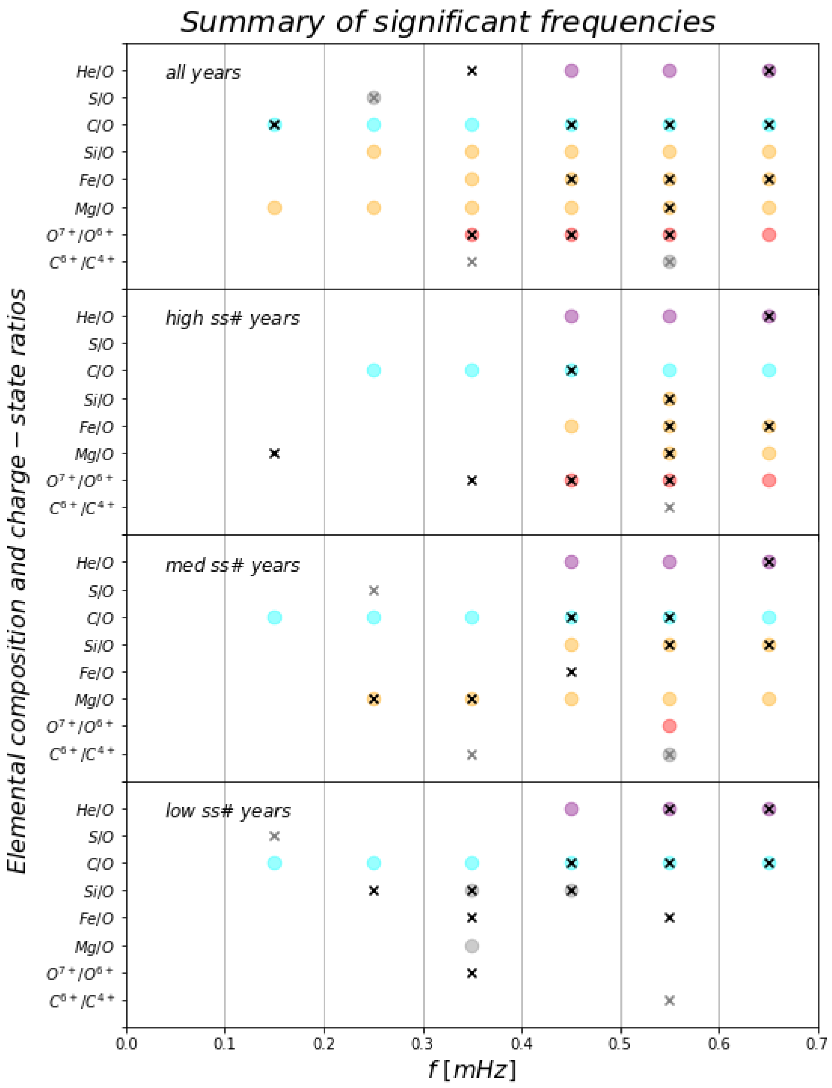

Figure 3.7: Summary of statistically significant and characteristic frequencies found for all elemental composition and charge-state ratios in the 14 years of ACE/SWICS data analyzed. Results are shown for the full data set, as well as for high, medium and low sunspot number year groupings.

In this study, we have only been able to cover the frequency range below 0.6 mHz, the lower band of frequencies examined in the proton density structure studies reported by *Kepko et al.* (2020); *Viall et al.* (2008). This is due to the fact that heavy ions are present in trace amounts in the solar wind and therefore require longer instrument accumulation times, and thus a lower temporal resolution, in order to acquire sufficient counts than do protons. Thus we are only able to characterize the largest scales considered in the studies of proton periodic density structures.

The ∼0.5–0.6 mHz frequency band is a characteristic scale for several elemental composition ratios and also appears in the charge state. This is a result that has been reported about periodic mesoscale proton density structures as well as about magnetospheric oscillations (*Kepko et al.*, 2020; *Viall et al.*, 2008; *Kepko and Spence*, 2003; *Lyons et al.*, 2002; *Lessard et al.*, 2003). *Kepko and Spence* (2003) identifies this as one of the frequency bands for which magnetic field oscillations observed to be directly driven by proton periodic density structures in the solar wind, indicating that this is an important frequency band for connecting solar wind observations to magnetospheric oscillations. The ∼0.5–0.6 mHz frequency band was also identified in event studies of solar wind elemental composition and charge state *Kepko et al.* (2016); *Gershkovich et al.* (2022). *Kepko et al.* (2002b) and *Villante et al.* (2001) report a 0.7 mHz frequency result with significant power in magnetic field oscillations driven by proton periodic density structures and ground magnetometer data respectively. This frequency is limited by the Nyquist frequency of the ACE/SWICS data, but we do observe power in the frequency range 0.6 mHz in the composition data as well the charge state.

We have divided the 1998-2011 ACE/SWICS data into segments consisting of several years each and divided by average sunspot number in order to study the impact of solar activity on the number and types of periodic structures observed. Figure 3.6 shows that the fraction of segments that we were able to validate which contained one or more significant periodicities for the elemental abundance ratios and charge state. The figure shows that the result rates were fairly constant for low, medium and high average sunspot numbered year groupings, as well as when all years were analyzed together. This is consistent with what was observed by *Kepko et al.* (2020) in the study of proton periodic density structures and their dependence on solar activity.

3.5 Conclusion

In this chapter we have expanded upon previously conducted statistical studies of solar wind periodic density structures by extending the analysis from proton data to high-resolution elemental composition and charge state measurements. Variations in composition are an important tool for understanding how the solar wind connects to its sources on the Sun, how it is formed and how it is released. This is because composition is established at the Sun and cannot evolve en route. We provide occurrence distributions of statistically significant periodic structures found in low-FIP, intermediate-FIP, high-FIP and charge state abundance ratios and shown that there is a characteristic scale as some frequencies occur more often then others throughout the 14 years. We show that the width of the statistically significant frequency bands for each distribution is dependent on FIP and that the Fe/O distribution differs substantially from the other low-FIP ratio distributions (Mg/O and Si/O), likely due to gravitational settling effects dominating the heavy Fe ions for some solar process (*Weberg et al.*, 2012). The ∼0.5–0.6 mHz characteristic scale observed is associated with observations of magnetospheric oscillations that were previously linked to proton density structures in the solar wind. Finally, in line with the proton statistical study findings of *Kepko et al.* (2020), we have determined that the number of validated windows, for all ratios considered in the analysis, containing at least one result do not exhibit a dependence on solar activity.

Future work will be to apply the methods and techniques presented here to higher-resolution data sets, covering observations from a large range of orbital distances, measured by new instruments such as Solar Orbiter's Heavy Ion Sensor.

CHAPTER IV

Periodic Density Structures in Early SO-HIS Heavy Ion Composition Data

4.1 Background

The Solar Orbiter mission, launched on February 9, 2020, aims to link physical processes occurring in the Sun and within the solar corona to properties of the solar wind observed remotely and *in situ* at the location of the spacecraft (*Owen et al.*, 2020). Due to the uniqueness of its orbit, Solar Orbiter will make unprecedented measurements of the solar wind in the inner heliosphere, coming as close to the Sun as 0.28 AU, as well as taking measurements in and up to 30° above the ecliptic plane. To accomplish its science goals, Solar Orbiter is equipped with the Solar Wind Analyzer (SWA) suite of instruments. This suite contains an Electron Analyzer System (EAS), a Proton and Alpha particle Sensor (PAS) and a Heavy Ion Sensor (HIS). This suite of instruments will characterize the majority of the ions and electrons of the solar wind as well as determine the charge state and elemental abundances of the heavy ion populations. Linking observed solar wind properties to features, sources and mechanisms on the Sun is critical to understanding the fundamental physics involved. It is also key to advancing our understanding of space weather events and mitigating their impact on our increasingly technological society.

Of particular interest to us in this work is the SO-HIS instrument and its high-resolution heavy ion composition measurements as this work is focused on investing mesoscale periodic structures now known to be present in the composition of the solar wind (*Gershkovich et al.*, 2022; *Kepko et al.*, 2016; *Viall et al.*, 2009b). As discussed in previous chapters, periodic structures observed in the solar wind's elemental and charge state composition are particularly important in constraining the physical processes responsible for the formation, release and acceleration of the solar wind. This is because composition is determined in the solar atmosphere and does not evolve as the solar wind advects towards the point of observation, allowing us to make the critical connections between *in situ* properties of the observed solar wind and source regions on the Sun. Never before have periodic structures in the solar wind's elemental and charge state composition been observed *in situ* in the inner heliosphere, and never before has an instrument measured heavy ion abundances with such high temporal resolution. We present early results in this chapter as the instrument is still being tuned.

4.2 Methodology

4.2.1 Overview

We examine thirty-three 24-hour windows covering the time period from January 19, 2022 to March 10, 2022, during which HIS was operational and moving from an orbital distance of 0.92 AU to 0.46 AU. We also examine the corresponding SO-PAS and SO-MAG data segments in order to provide context. At this time, the SO-HIS data are still preliminary, and thus we only use combinations of the most robustly validated ions as proxies for low-FIP (Fe/O) and high-FIP (He/O) elemental abundance ratios. The ions included in the study are O^{6+}, O^{7+}, He^{2+}, and Fe^{8+}–Fe^{12+}. These are the dominant charge-states of these elements in the solar wind and should be representative of the full elemental abundance ratios when integrated. We analyze the O^{7+}/O^{6+} charge-state ratio in order to make determinations about the relationships between variations in the charge-state ratios and the elemental abundances. Each 24-hour time series is prepared for spectral analysis and analyzed as described in 4.2.2. The results of the spectral analysis runs are summarized and plotted as a function of time and orbital distance. For each time window, we also examined the SO-PAS proton density, bulk solar wind speed and solar wind temperature data as well as Solar Orbiter's magnetometer (MAG) data in order to constrain the bulk properties of the solar wind and to connect these to potential source regions on the Sun. Several windows of interest containing statistically significant periodic density structures are selected and discussed in detail.

4.2.2 Spectral Analysis

The general spectral analysis technique used in this study is similar to what was described in Section 1.8. This technique is designed specifically to extract periodic signals from astrophysical time series. Each nominally 24-hour-long time series segment is prepared for spectral analysis by making sure that it is resampled to a 10-minute time stamp, contains at least 90% validated data points and no more than 3 missing data points in a row. Each data point must meet a minimum instrument count threshold of 25 in order to be validated. Once processed, each 24-hour segment is run through the spectral analysis method (*Di Matteo et al.*, 2020, 2021) reviewed in Section 1.8. For this analysis, we require that each result pass the amplitude test and the F-test at a 95% confidence level.

4.2.3 The HIS Instrument

The Solar Orbiter Heavy Ion Sensor (SO-HIS) is a triple-coincidence ion mass spectrometer. It is designed to measure the ionic and elemental composition and 3D velocity distribution functions of the heavy ions (He to Fe) in the bulk solar wind beween 0.5 and 18 KeV/e (*Owen et al.*, 2020). SO-HIS has a Field of View (FOV) that spans 96° in the ecliptic and scans a ±17° range of elevations above and below the ecliptic. It provides the first *in situ* solar wind composition measurements from within the inner heliosphere. When fully operational, the instrument measures at rates as fast as every 4 seconds in Burst Mode, 30 seconds in Normal Mode and 300 seconds in Normal Mode (Low Cadence). The resolution is constrained by the amount of time that it takes to scan all energies between 0.5 and 80 keV/e in 64 steps and all elevation angles in 16 steps. Currently, only data accumulated to a 10-minute time step has been fully processed and validated and is therefore what is used in this study.

4.3 Results

Figure 4.1 shows the elemental composition and charge state time series for the periods analyzed, panels a-c), plotted with the bulk plasma diagnostic parameters: d) proton density, e) proton speed and He^{2+} speed, f) temperature, g) magnitude of the magnetic field and h) the components of the magnetic field in the Radial Tangential Normal (RTN) spacecraft-centered coordinate system. Typical fast (coronal hole) and slow (streamer) wind values are plotted in blue and red respectively. There are data gaps in the time series during which the instrument was not operational. We analyze the segments for which there are sufficient counts and sufficient continuity to produce robust spectral analysis results. The data are validated according to the criteria stated in Section 4.2.

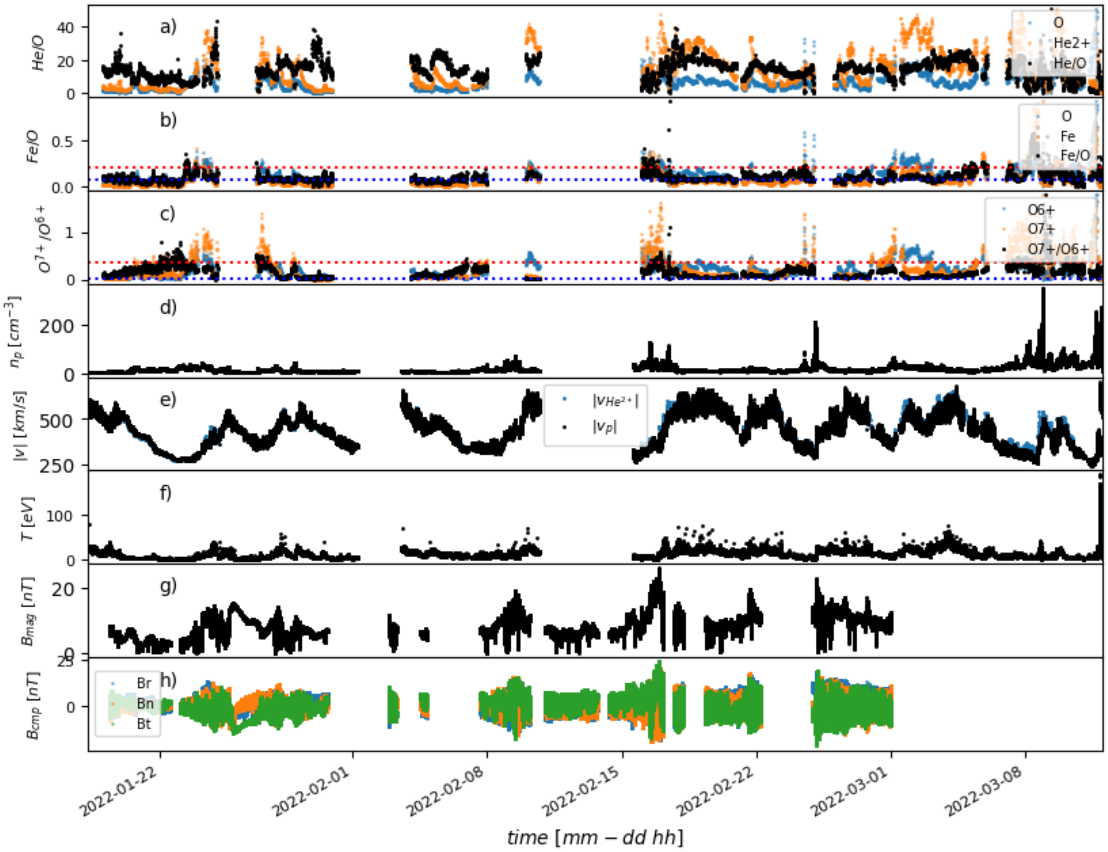

Figure 4.1: Time series covering the full preliminary HIS data set span.

We begin by validating the heavy ion data by comparing the heavy ion abundance and charge state ratio versus velocity distributions to the corresponding ACE/SWICS distributions, as this has not been done before. Figure 4.2 shows the relationships between Fe/O and O^{7+}/O^{6+} and the He^{2+} speed. Here, the He^{2+} speed is a proxy for the the solar wind bulk speed. The figure also shows results from ACE/SWICS data reported by *Stakhiv et al.* (2016) for comparison [Left]. Both data sets show an anti-correlation between solar wind speed and O^{7+}/O^{6+} but not Fe/O. The Fe/O data in both data sets exhibits similar spread.

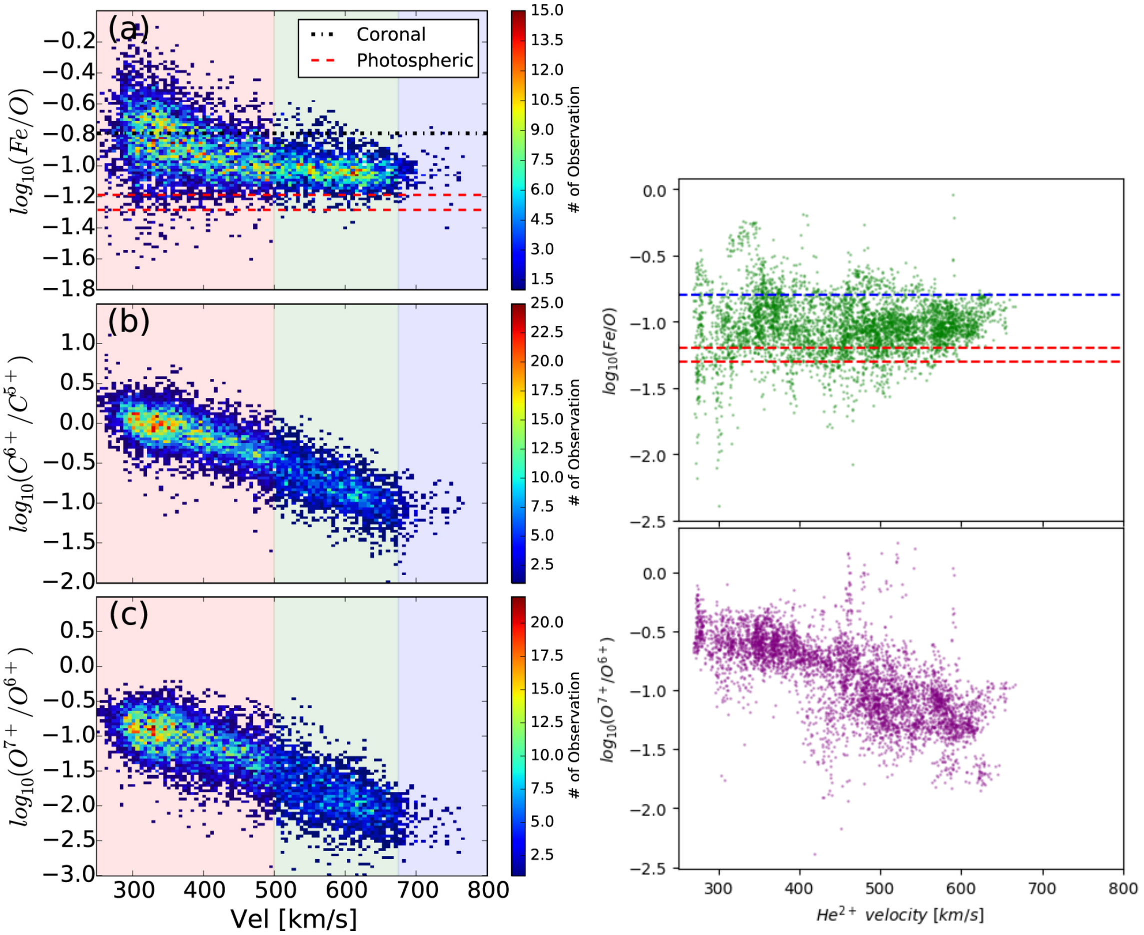

Figure 4.2: Fe/O and O^{7+}/O^{6+} abundance ratio values as a function of solar wind velocity for ACE/SWICS [Left] and for the SO-HIS preliminary data [Right].

After confirming that Fe/O and O^{7+}/O^{6+} behave generally as expected, we begin our spectral analysis of the data segments. Figure 4.3 shows a summary plot of the spectral analysis results for each 24-hour segment of the data set. The x-axis (bottom) shows the median orbital distance during the course of the segment. Each segment is labeled at its beginning – on the right side. The date of the beginning of each segment is labeled on the top x-axis. Results are shown for He/O (purple), Fe/O (yellow) and O^{7+}/O^{6+} (red) as color-coded, vertical lines positioned at a distance that is proportional to the frequency (0 if on the left edge of the segment and 0.8 mHz if on the right edge) from the line that marks the beginning of the segment. The top panel summarizes results that pass, at the 95% confidence level, the amplitude test only. The bottom panel summarizes results that pass both the amplitude test and the F-test at the 95% confidence level. Each significant frequency on the bottom panel is labeled with its value in mHz.

During the date range of 20 February 2022 – 1 March 2022 (0.67–0.57 AU), both the top panel and the bottom panel exhibit a gap during which statistically significant periodic structures were sparse or not evident. The bottom panel (showing the amplitude + F-test results) shows two segments (5 February 2022 and 19 February 2022) during which the Fe/O and O^{7+}/O^{6+} abundance ratios exhibited periodicity while the He/O ratio did not and two segments during which the He/O exhibited periodic density structures while Fe/O and O^{7+}/O^{6+} did not, 3 March 2022 and 7 March 2022 (at 0.5 AU and 0.49 AU). The time series and spectral analysis results for 5 February 2022, 19 February 2022 and 7 March 2022 are presented below.

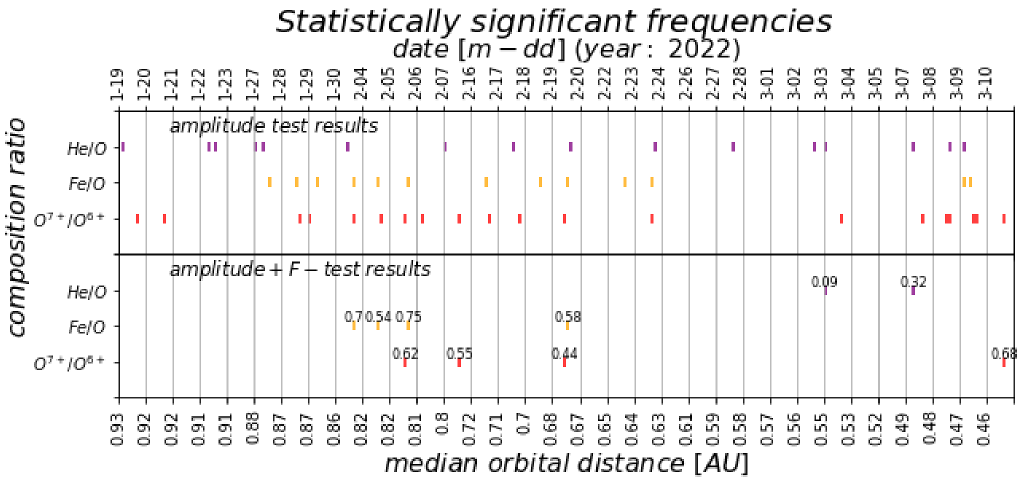

Figure 4.3: Summary chart showing statistically significant and characteristic frequencies found in the SO-HIS data set as a function of the mean orbital distance of the spacecraft during each validated 24-hour segment.

Figure 4.4 [Left] shows the a) He/O, b) Fe/O, c) O^{7+}/O^{6+}, d) proton number density, e) solar wind speed and d) temperature time series for the 5 February 2022 (median orbital distance: 0.82 AU) 24-hour segment. The typical coronal hole (fast) and streamer (slow) values for each ratio are shown as blue and red dotted lines, respectively. The Fe/O and O^{7+}/O^{6+} stay at typical coronal hole levels throughout the duration of the segment. There is an enhanced proton density, with a corresponding He/O dropout and dip in solar wind speed. This occurs in the first two hours of the segment. The solar wind speed is at the boundary between what is typically considered fast and what is typically considered slow in the historical, bi-modal model. SO-MAG magnetometer data was unavailable for this segment of time.

Figure 4.4 [Right] shows the spectral analysis results for the elemental composition and charge state ratios. The red triangles in panels a), c) and e) indicate F-test results at the 95% confidence level and the dashed red line indicates this level. In panels b), d) and f), the solid red curve shows the background model and the dashed curve indicates the 95% confidence level. Purple circles show results that pass the amplitude test and a black "x" indicates that the result passed the F-test as well. In

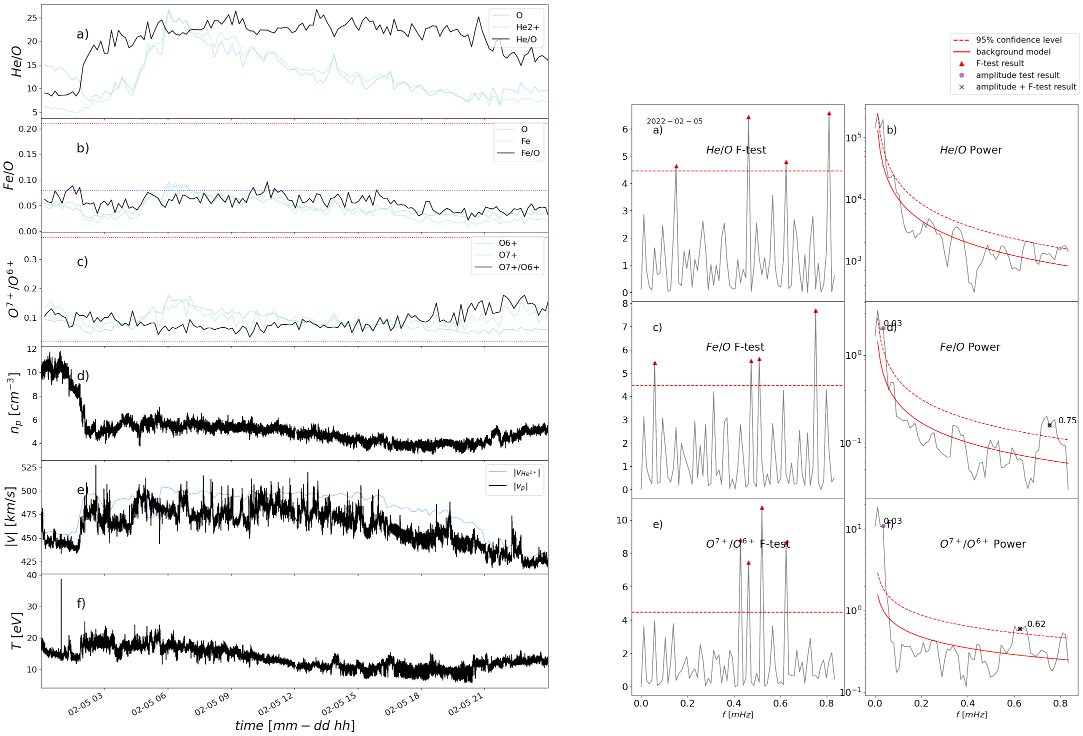

Figure 4.4: **Left:** Composition and bulk plasma time series for the 5 February 2022 SO-HIS 24-hour segment. **Right:** Spectral analysis results for the 5 February 2022 SO-HIS 24-hour segment.

this case, both the Fe/O and O^{7+}/O^{6+} ratios show a significant frequency, passing both the amplitude above background and harmonic F-test, in the upper range of the frequency space (at 0.75 mHz for Fe/O and 0.62 mHz for O^{7+}/O^{6+}. Both of these ratios also exhibit a 0.03 mHz amplitude test result, but this is in a region of the frequency space more prone to false positives as demonstrated in our Monte Carlo simulations (*Di Matteo et al.*, 2021). The He/O time series does not contain periodic structures.

Figure 4.5 [Left] shows the a) He/O, b) Fe/O, c) O^{7+}/O^{6+}, d) proton number density, e) solar wind speed and d) temperature time series for the 19 February 2022 (median orbital distance: 0.68 AU) 24-hour segment. The typical coronal hole (fast) and streamer (slow) values for each ratio are again shown as blue and red dotted lines, respectively. The Fe/O and O^{7+}/O^{6+} stay at typical coronal hole levels throughout the duration of the segment as well. The solar wind speed is at the boundary between what is typically considered fast and what is typically considered slow in the historical, bi-modal model. SO-MAG magnetometer data was unavailable for the first 8 hours of this segment.

Figure 4.5 [Right] shows the spectral analysis results for the elemental composition and charge state ratios. The red triangles in panels a), c) and e) indicate F-test results at the 95% confidence level and the dashed red line indicates this level. In panels b), d) and f), the solid red curve shows the background model and the dashed curve indicates the 95% confidence level. Purple circles show results that pass the amplitude test and a black "x" indicates that the result passed the F-test as well. Here, both the Fe/O and O^{7+}/O^{6+} ratios show a significant frequency, passing both the amplitude above background and harmonic F-test, in the middle range of the frequency space (at 0.58 mHz for Fe/O and 0.44 mHz for O^{7+}/O^{6+}. The He/O time series shows a result passing the amplitude test, but without a corresponding F-test signal.

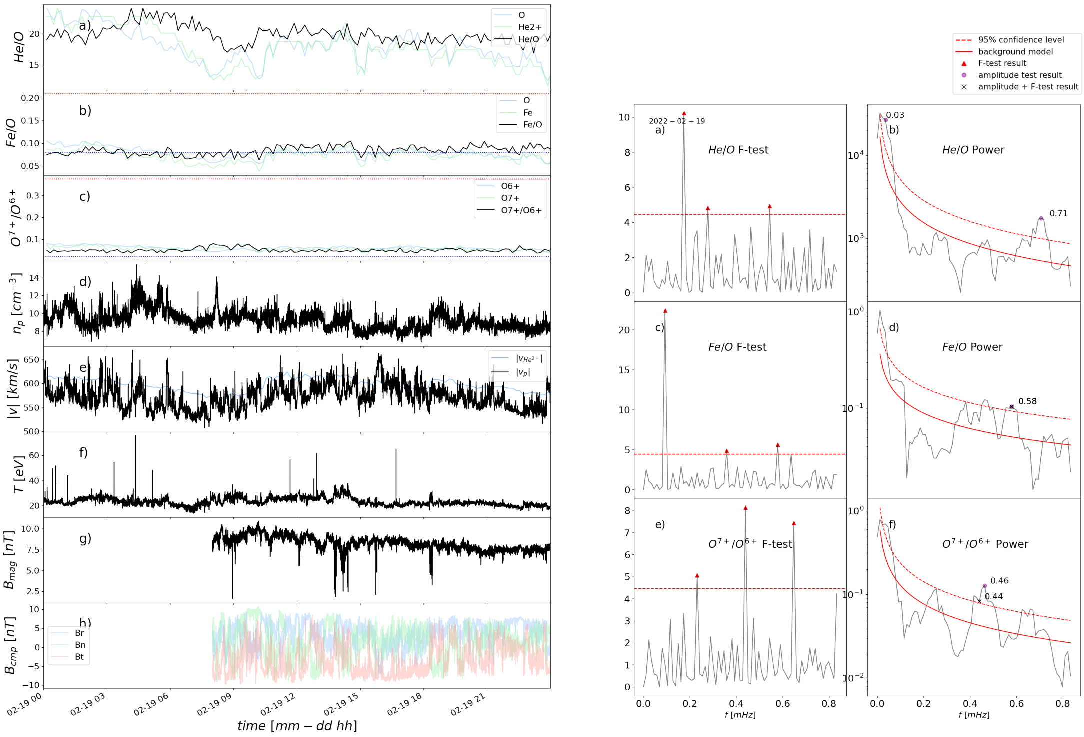

Figure 4.5: **Left:** Composition and bulk plasma time series for the 19 February 2022 SO-HIS 24-hour segment. **Right:** Spectral analysis results for the 19 February 2022 SO-HIS 24-hour segment.

Figure 4.6 [Left] shows the a) He/O, b) Fe/O, c) O^{7+}/O^{6+}, d) proton number density, e) solar wind speed and d) temperature time series for the 7 March 2022 (median orbital distance: 0.49 AU) 24-hour segment. In this segment, O^{7+}/O^{6+} stays at a typical streamer level throughout. The Fe/O ratio, however, exhibits an approximately 12-hour long drop to a typical coronal hole value from 03-07 06 to 03-07 21. This drop coincides with a slight drop in the proton speed and rise in temperature. The He^{2+} speed differs from the proton speed throughout the segment. The solar wind speed is below 500 km/s and well within the slow category. SO-MAG magnetometer data was unavailable for this segment.

Figure 4.6 [Right] shows the spectral analysis results for the elemental composition and charge state ratios for this segment. Here, both the Fe/O and O^{7+}/O^{6+} ratios show an amplitude test result close to the Nyquist frequency which are likely to be spurious (*Di Matteo et al.*, 2021). The 0.06 mHz result for the charge state is also marginal and has been removed from the summary chart. The He/O time series shows a result passing both the amplitude test and the F-test at 0.32 mHz as well as a 0.29 amplitude test result.

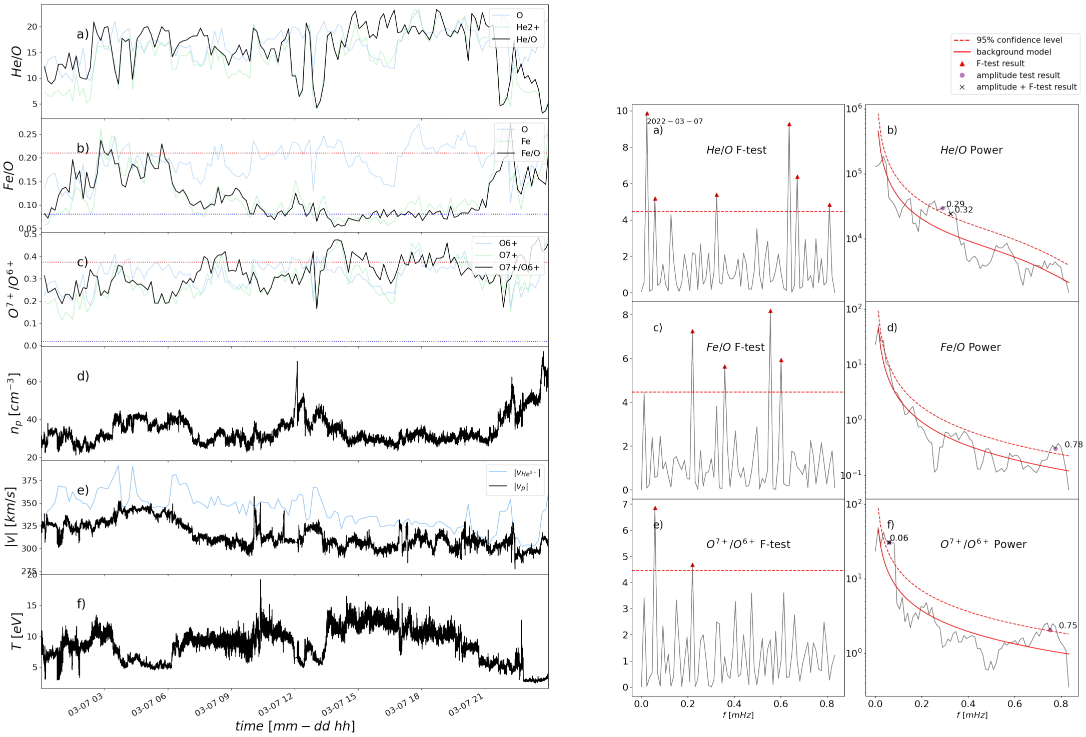

Figure 4.6: **Left:** Composition and bulk plasma time series for the 7 March 2022 SO-HIS 24-hour segment. **Right:** Spectral analysis results for the 7 March 2022 SO-HIS 24-hour segment.

4.4 Discussion

The data used here is preliminary as the instrument is still undergoing its verification. Figure 4.3 shows the full data set considered in this analysis, showing all abundance ratios in the study, proton density, proton speed and helium speed, temperature, magnetic field magnitude and RTN magnetic field vector components. We begin by confirming the relationship between Fe/O and O^{7+}/O^{6+} ratios and the solar wind speed. We find that the trends match results previously reported for ACE/SWICS data (*Stakhiv et al.*, 2016) and show that low-FIP abundances and charge states do not always behave according to the historical bi-modal fast/slow solar wind model. Instead, there is a continuum of solar wind states and likely winds on the boundaries of closed magnetic loops and coronal holes interact in more complex ways, creating a "boundary wind" category (*Stakhiv et al.*, 2015, 2016; *Zurbuchen et al.*, 2002). Figure 4.2 shows that the O charge state exhibits a negative correlation with solar wind speed while Fe/O does not. *Stakhiv et al.* (2016) suggests that solar wind travelling at a speed of less than 500 km/s could be composed of two parts: wind released from closed loops via magnetic reconnection with open magnetic field lines on the Sun, and a smaller population of coronal-hole wind traveling at speeds slower than 500 km/s that can be identified by its low Fe/O ratio, higher differential streaming (between protons and alpha particles), and higher differential temperatures (between O^{6+} and protons).

Though the data is preliminary and not continuous over the period from 19 February 2022 to 10 March 2022, we have been able to validate and analyze 33 24-hour segments at different orbital distances ranging from 0.92 AU and 0.46 AU. This is the first time *in situ* measurements of heavy ions have been performed in the inner heliosphere and analyzed for periodicity. We identify statistically significant frequencies for all ratios in the study (Fe/O, He/O and O^{7+}/O^{6+}). Results passing the amplitude test only are common and show a relationship between orbital distance and the number of results observed for each ratio. There is a period between 20 February 2022 and 5 March 2022 (0.67–0.52 AU) during which the occurrence rate of statistically significant frequencies drops out for all ratios. This may be due to the specific plasma conditions observed by the spacecraft during this pass and not a fundamental relationship. Further observations are needed.

We focus on signals that not only pass the amplitude test but that are also verified by a corresponding F-test result (labeled in the bottom panel of Figure 4.3), which also show a low occurrence rate of periodic density structures during this period. The segments that do contain periodicities show Fe/O and O^{7+}/O^{6+} exhibiting similar periodicities in two segments (5 February 2022 and 19 February 2022) during which He/O does not contain periodic structures. We also observe two segments during which He/O contained significant periodic density structures while Fe/O and O^{7+}/O^{6+} did not (3 March 2022 and 7 March 2022). Though these are only two segments, this behavior is consistent with the ACE statistical results wherein He exhibited different frequencies than did the Fe/O.

The S-Web model (*Antiochos et al.*, 2011) predicts that interchange reconnection occurs at the magnetic open-closed boundary between closed loops and magnetic field lines open to the heliosphere. These results indicate that the structures may have formed due to periodic interchange reconnection (*Fisk*, 2003; *Antiochos et al.*, 2011; *Crooker et al.*, 2002) events between closed magnetic loops, in active and quiet Sun regions, where low-FIP elements and charge states are enhanced relative to photospheric levels, and open field lines emanating from coronal holes where these ratios are at average photospheric levels. Interchange reconnection has been posited a candidate mechanism for how these periodic density structures enter the solar wind previously (*Kepko et al.*, 2016; *Viall et al.*, 2009b; *Réville et al.*, 2020; *Di Matteo et al.*, 2019; *Viall and Vourlidas*, 2015b; *Higginson and Lynch*, 2018; *Gershkovich et al.*, 2022). Segments during which only Fe/O or only O^{7+}/O^{6+} exhibit periodicities may be due to the fact that the solar wind fractionation and release processes are complex and that FIP effect and charge state do not always behave identically, as seen in their relationships to the solar wind velocity (Figure 4.2), producing a continuum of solar wind states (*Stakhiv et al.*, 2015, 2016; *Zurbuchen et al.*, 2002). This is partially due to the fact that charge state is determined by processes occurring high in the corona (up to $\sim$5 $R_\odot$), and thus may evolve even after the interchange reconnection events occur, whereas the FIP is set in the chromosphere.

Of the three 24-hour segments described in detail in Section 4.3, two (5 February 2022 and 17 February 2022) showed Fe/O and charge state at typical photospheric levels throughout, indicating that they originated primarily from coronal holes on the Sun's surface. The 7 March 2022 segment revealed disparities between the behavior of Fe/O and charge state. O^{7+}/O^{6+} remained at typical streamer, slow wind values, while Fe/O undergoes a 12-hour-long dip to coronal hole, fast wind average values. Such "dropouts" of Fe have been reported by *Weberg et al.* (2012) and are likely due to gravitational settling, a mass-dependent effect that causes heavy elements to gravitationally settle in large coronal loops and override the influences of the FIP effect.

Due to the fact that the SO-HIS plasma spectrometer is still undergoing verification, all results must be confirmed through further measurements. However, these early results are promising as they are consistent with previous observations and models (*Kepko et al.*, 2016; *Viall et al.*, 2009b; *Réville et al.*, 2020; *Di Matteo et al.*, 2019; *Viall and Vourlidas*, 2015b; *Higginson and Lynch*, 2018; *Gershkovich et al.*, 2022; *Stakhiv et al.*, 2015, 2016) while also providing new insights into periodic density structures in solar wind composition and their possible dependence on orbital distance.

4.5 Summary

In this chapter, we have characterized and summarized some of the earliest SO-HIS heavy ion data from a 33-day period during which the Solar Orbiter spacecraft was travelling from 0.92 to 0.46 AU. We have confirmed the relationship between Fe/O and solar wind speed as well as the relationship between the O^{7+}/O^{6+} charge-state ratio and the solar wind speed by comparing their 2D distributions to similar distributions from the ACE/SWICS mission (*Stakhiv et al.*, 2016). Furthermore, we have examined each validated 24-hour segment for periodicity and found a preliminary relationship between the median orbital distance of the spacecraft and the significant frequencies observed in the He/O, Fe/O and O^{7+}/O^{6+} composition ratios for the events in this data set. We have presented early indications that there is a FIP bias and charge-state bias present as the Fe/O low-FIP ratio and the O^{7+}/O^{6+} ratio exhibited similar behaviour in frequency space which differed from the behaviour of He/O for results passing both the amplitude-above-background and the harmonic F-test. Matching variations in low-FIP and charge-state ratios indicate that interchange reconnection may be the mechanism responsible. These variations are determined in the Sun and cannot evolve en route to the spacecraft, so they preserve clues to the processes that form and release them, as well as provide information about their likely source regions on the Sun.

The data used here is preliminary, and the results need further confirmation. The SO-HIS instrument is in the early stages of its mission, and data validation is ongoing. Even though this analysis uses the highest resolution heavy ion data to date (a 10-minute cadence) once fully validated, HIS will be able to provide data sampled at rates as high as every 4 seconds in Burst Mode and every 90 seconds in Normal Mode. Future work will be to analyze long series of segments with better continuity, use full elemental abundance ratios rather than proxies, remove transients such as CMEs, and to identify synergies with Parker Solar Probe observations.

CHAPTER V

Conclusions and Future Work

5.1 Conclusions

The science questions addressed in this work are all motivated by the aims of understanding how the solar wind is formed, to connect the *in situ* solar wind to its source regions on the Sun and to understand how the solar wind is released and accelerated.

Towards these ends, Chapter II presented research that expanded greatly upon previous reports of mesoscale periodic density structures found in the elemental and ionic composition of the solar wind (*Kepko et al.*, 2016; *Viall et al.*, 2009b). It examined more elements and validated heavy ion abundance data segments than all previous studies and found variations in the relative abundance of low-FIP elements, mass dependencies, and charge states which could have only been determined at the Sun. These variations provide clues to temporal or spatial variations in solar source regions and put important constraints on the solar wind formation mechanisms that produce them.

Chapter III presented the results of the first statistical study of mesoscale periodic density structures in the solar wind's heavy ion abundances. It examined 14 years of ACE/SWICS elemental and charge state composition data for periodicity and provided the first occurence distributions of significant frequency bands for low-

FIP (Fe/O, Mg/O and Si/O), intermediate-FIP (C/O and S/O), high-FIP (He/O) and charge state (O^{7+}/O^{6+} and C^{6+}/C^{4+}) abundance ratios. It found statistically significant frequency bands present in the distributions and that some frequencies occurred more often than others, rising above the smoothed shape of the distributions. Thus it demonstrated that there are characteristic scales associated with elemental and charge state periodic density structures as there are for proton density structures (*Kepko et al.*, 2020; *Viall et al.*, 2009a, 2008). No solar cycle dependence on the number of segments containing one or more significant results per validated segment was observed. This is consistent with what has been reported about periodic density structures in the proton number density (*Kepko et al.*, 2020). The significant and characteristic frequencies observed did exhibit a dependence on sunspot number, however, which is also consistent with the prior work.

Both Chapter II and Chapter III identified a prevalent and significant ∼0.6 mHz frequency band. This is a result that has been reported about periodic mesoscale proton density structures as well as about magnetospheric oscillations (*Kepko et al.*, 2020; *Viall et al.*, 2008; *Kepko and Spence*, 2003; *Lyons et al.*, 2002; *Lessard et al.*, 2003). *Kepko and Spence* (2003) identifies this as one of the frequency bands for which magnetic field oscillations are observed to be directly driven by proton periodic density structures in the solar wind. Further work is needed to connect this specific power enhancement to the physical mechanism that drives it.

Chapter IV characterized and presented some of the earliest SO-HIS data. It confirmed the relationships between the Fe/O and O^{7+}/O^{6+} ratios and solar wind speed reported by *Stakhiv et al.* (2016) on the established ACE/SWICS observations. It presented statistically significant frequencies found in the He/O, Fe/O and O^{7+}/O^{6+} abundance time series and found a relationship between the number of results observed and orbital distance during the duration of the available data set. It demonstrated that the observations were consistent with interchange reconnection being the mechanism responsible for the formation and release of the structured solar wind. Furthermore, by examining variations in the abundance of He/O, Fe/O and charge state, which are determined near the Sun and connected to the source regions and mechanisms local to the solar environment, we link the solar wind observed to its likely source type on the solar surface.

5.2 Future Work

Future work will focus on further validating the SO-HIS data set in order to identify and remove transient events such as coronal mass ejections, to verify more heavy ion data so that full elemental abundance ratios can be derived and analyzed (rather than relying on proxies as we did here) and to look at longer periods of continuous data in order to robustly track the evolution of these periodic density structures. When HIS data is fully validated, it will provide data sampled at unprecedented rates (every 90 seconds in Normal Mode) and allow for the study of higher frequency ranges. This is necessarily limited by the low densities of heavy, low-FIP elements such as Fe and Mg in the solar wind and the integration times required to accumulate a statistically significant level of instrument counts.

Additionally, future work will include combining statistical and event study characterizations with a clustering categorization of solar wind types. This work is already in progress and will better link spectral analysis findings to the continuum of states that represent the solar wind.

Exploring synergies between SO-HIS and Parker Solar Probe data and combining remote observations with *in situ* measurements in order to trace parcels of solar wind back to their sources at the Sun is a necessary direction for future work. Connecting more periodic structures observed *in situ* to structures observed in coronal images, and vice versa, would be particularly significant. As SO-HIS is able to collect more data over the course of at least one solar cycle, it will critical to conduct statistical studies of the periodic structures present and compare the results to those from the ACE/SWICS study of Chapter III.

The solar wind is structured at many different scales (*Viall et al.*, 2021b), both temporal and spatial, spanning orders of magnitude. Combining data from future missions featuring a distributed array of instruments specifically designed to coordinate is urgently needed for gaining a more complete picture of plasma interactions within the heliosphere. This, in turn, is necessary to gaining a more complete understanding of the fundamental physics governing the solar wind and the processes that form, release and accelerate it. The techniques presented in this work are highly applicable to high-resolution data from such future missions. Additionally, the following observational advances are necessary:

1. Comprehensive magnetic field measurements (backside and polar regions) in order to better locate the HCS and the regions on the Sun to which the instrument is connected to
2. Continuous monitoring of temperature, magnetic field, and flow velocity in the middle corona to help link processes in the low corona (observed by EUV imagers) to the solar wind and heliosphere
3. Improved spectroscopy, on and off disk, of elements with a variety of FIPs, is important for making direct connections to *in situ* observations

Necessary future modeling advances include:

1. Fully 3D time-dependent models of source regions and acceleration mechanisms to help link observations to fundamental processes at the Sun
2. An accurate quiescent background model of the solar wind is needed. Future modeling needs to go beyond the large-scale fast/slow solar wind structure to capture phenomena at the “meso” scales.

APPENDIX

APPENDIX A

ACE/SWICS Statistical Study Distributions for LOW, MEDIUM, HIGH and ALL Sunspot Number Year Groupings

This appendix provides occurrence distribution plots in support of the Results and Discussion sections in Chapter III. For all plots:

The x-axis shows frequency in mHz. The y-axis represents the number of occurrences. Error bars that represent 2σ of the bootstrapped distribution are shown as solid purple vertical lines. The occurrence distribution is shown in gray and the expected false-positive rate for the method is shown as a dotted purple horizontal line. Significant frequencies are defined to rise 2σ above the expected false-positive rate. These are marked on the plot by a red dot and the numerical value of the corresponding bin center. Characteristic frequencies are marked by a blue "x". The extreme low and high frequency ranges shaded in red on each plot indicate frequency bins prone to false positives, according to Monte-Carlo simulations (*Di Matteo et al.*, 2021), and are therefore not considered as statistically significant results. The Rayleigh (f_{Ray}) frequency is 0.01 mHz and the Nyquist frequency (f_{Nyq}) is 0.69 mHz. The bin width is $3f_{Ray}$.

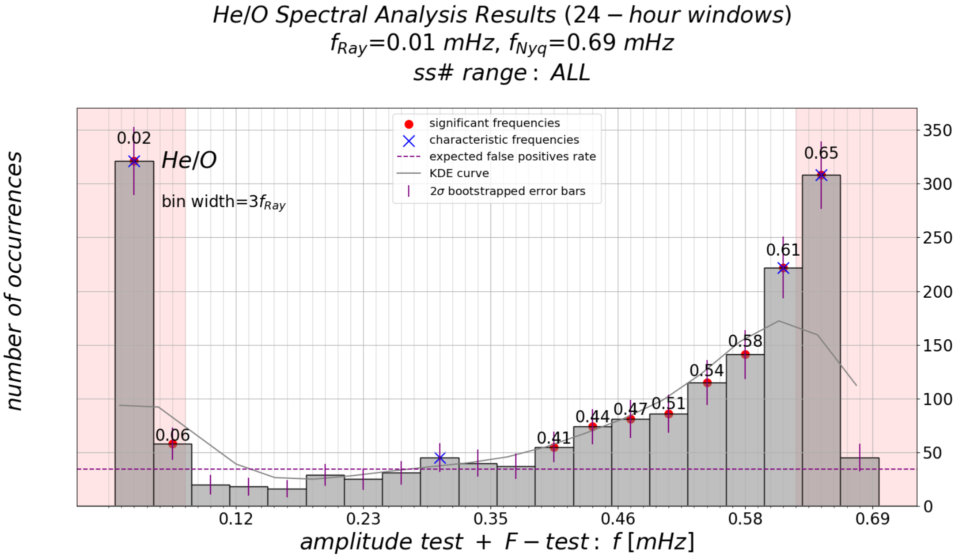

Figure A.1: He/O distribution for the ALL year grouping.

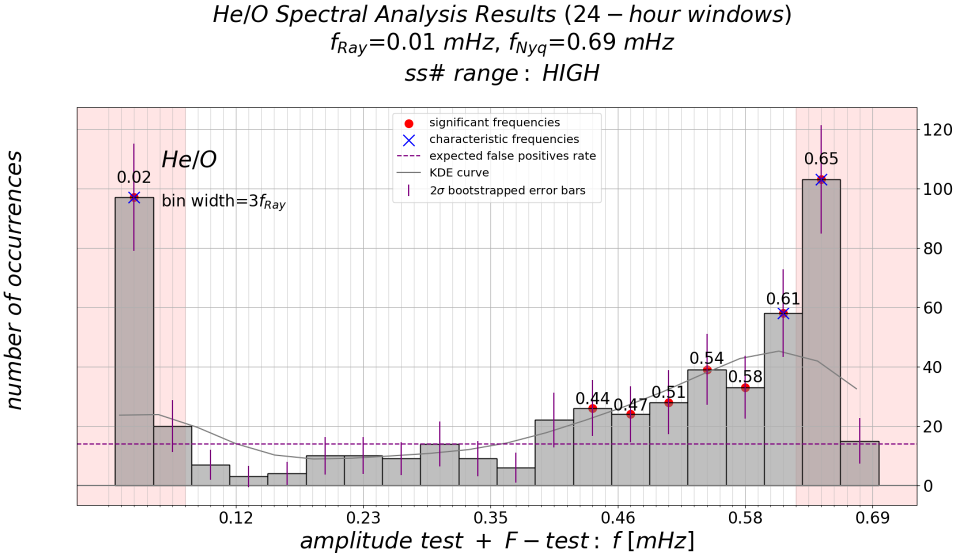

Figure A.2: He/O distribution for the HIGH year grouping.

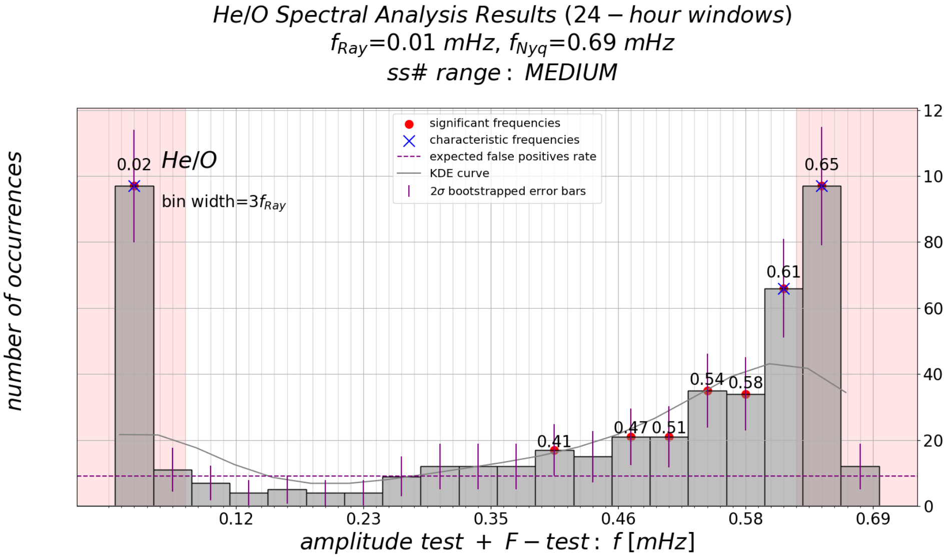

Figure A.3: He/O distribution for the MEDIUM year grouping.

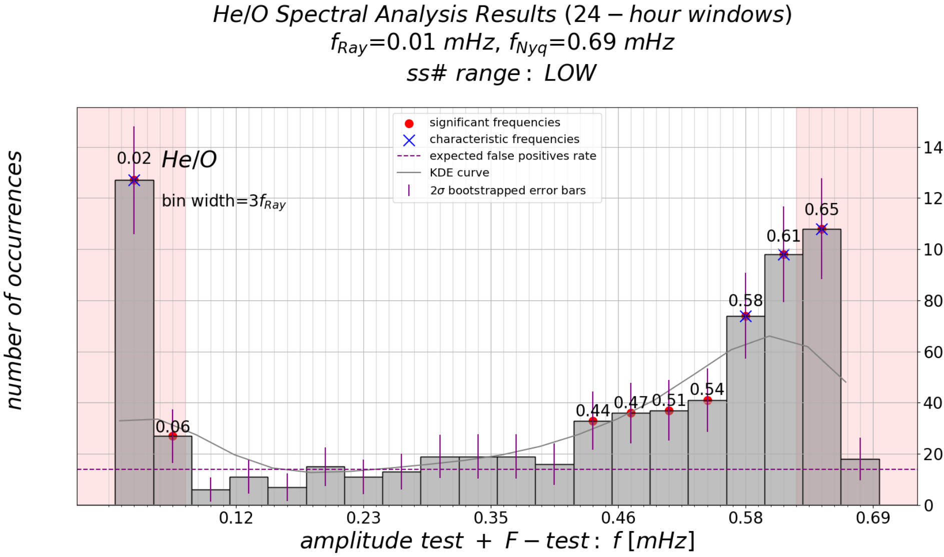

Figure A.4: He/O distribution for the LOW year grouping.

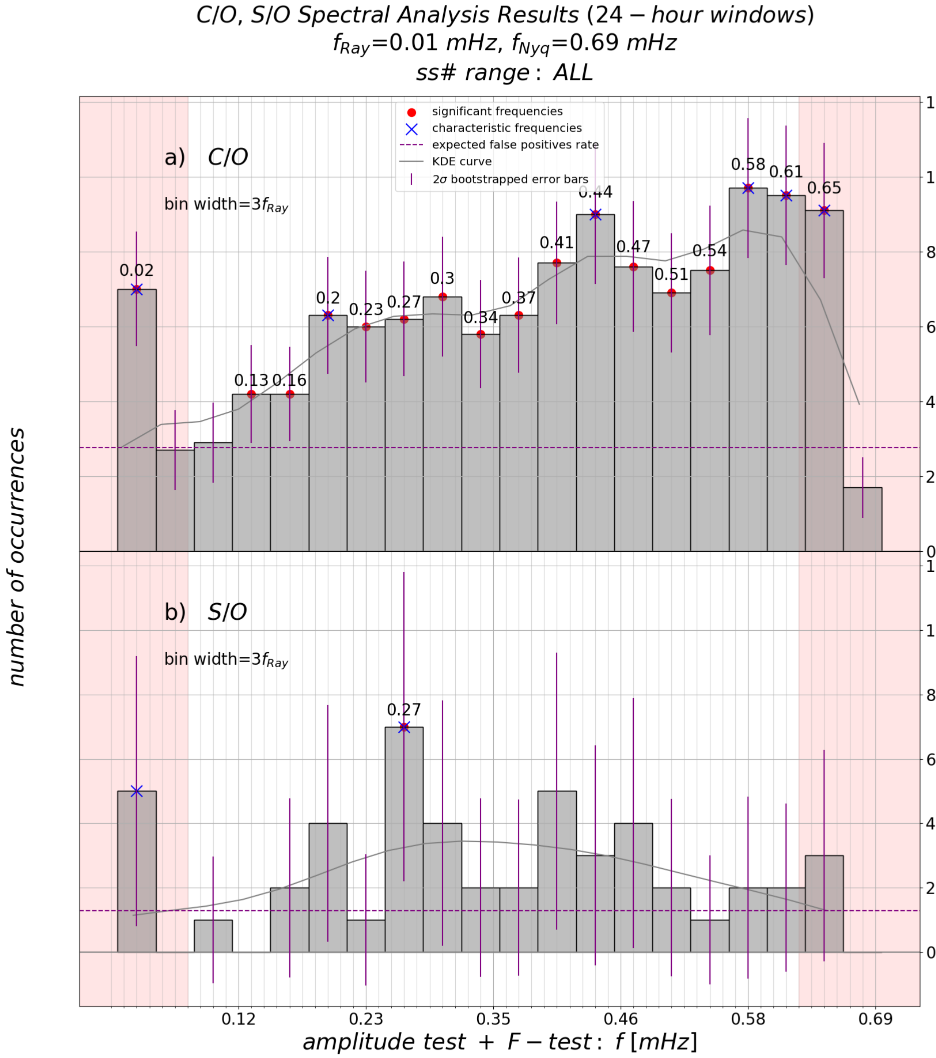

Figure A.5: C/O and S/O distributions for the ALL year grouping.

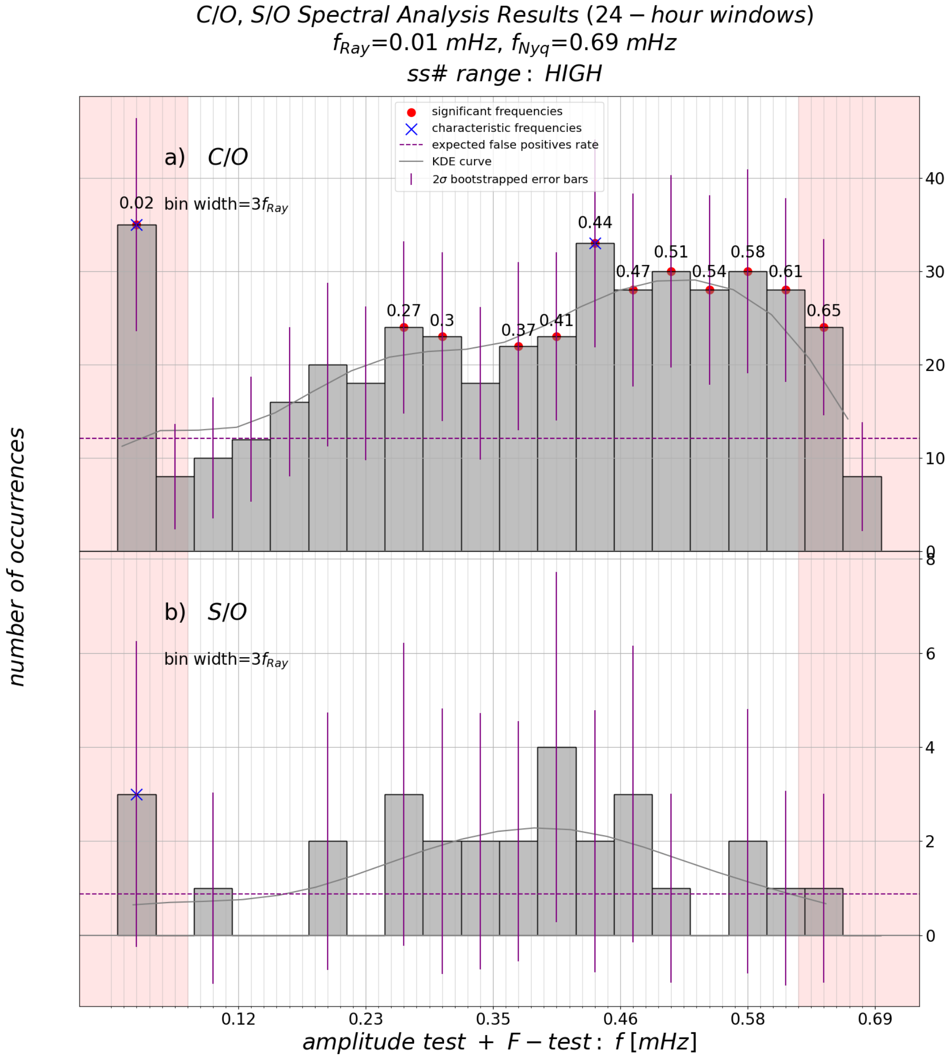

Figure A.6: C/O and S/O distributions for the HIGH year grouping.

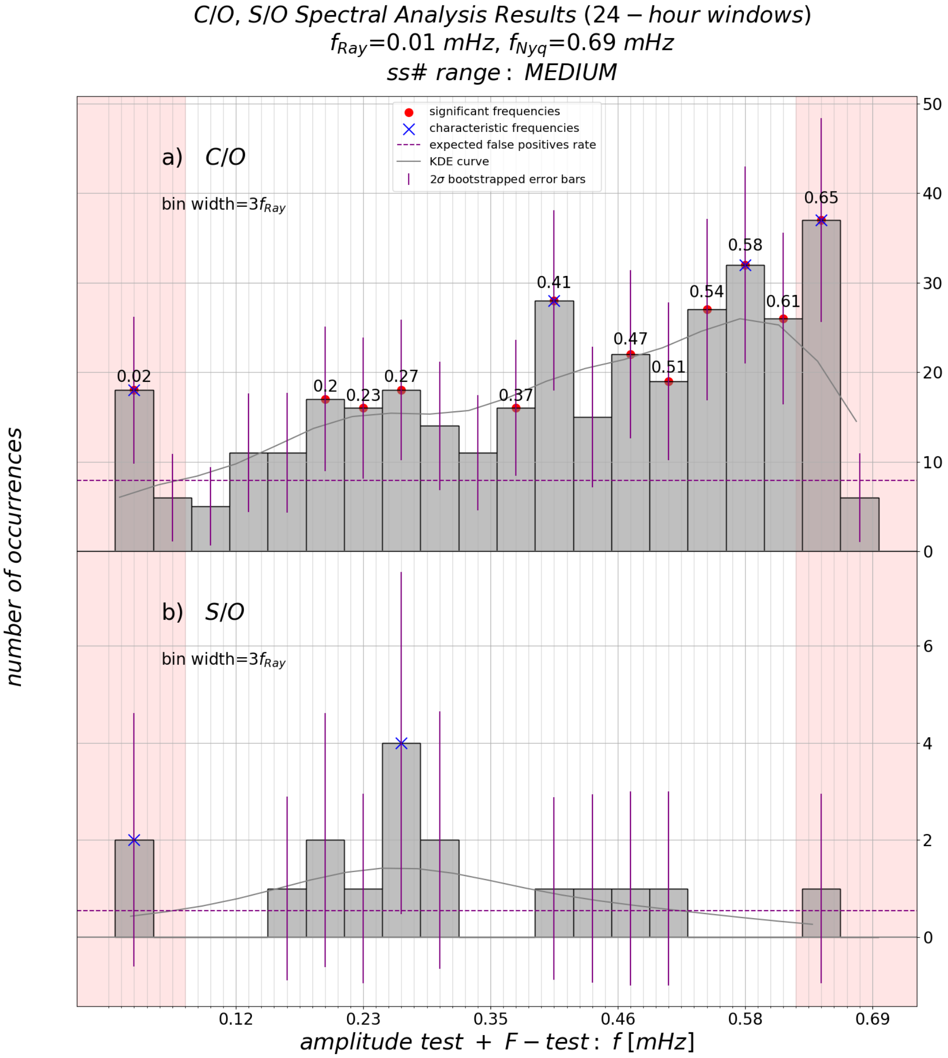

Figure A.7: C/O and S/O distributions for the MEDIUM year grouping.

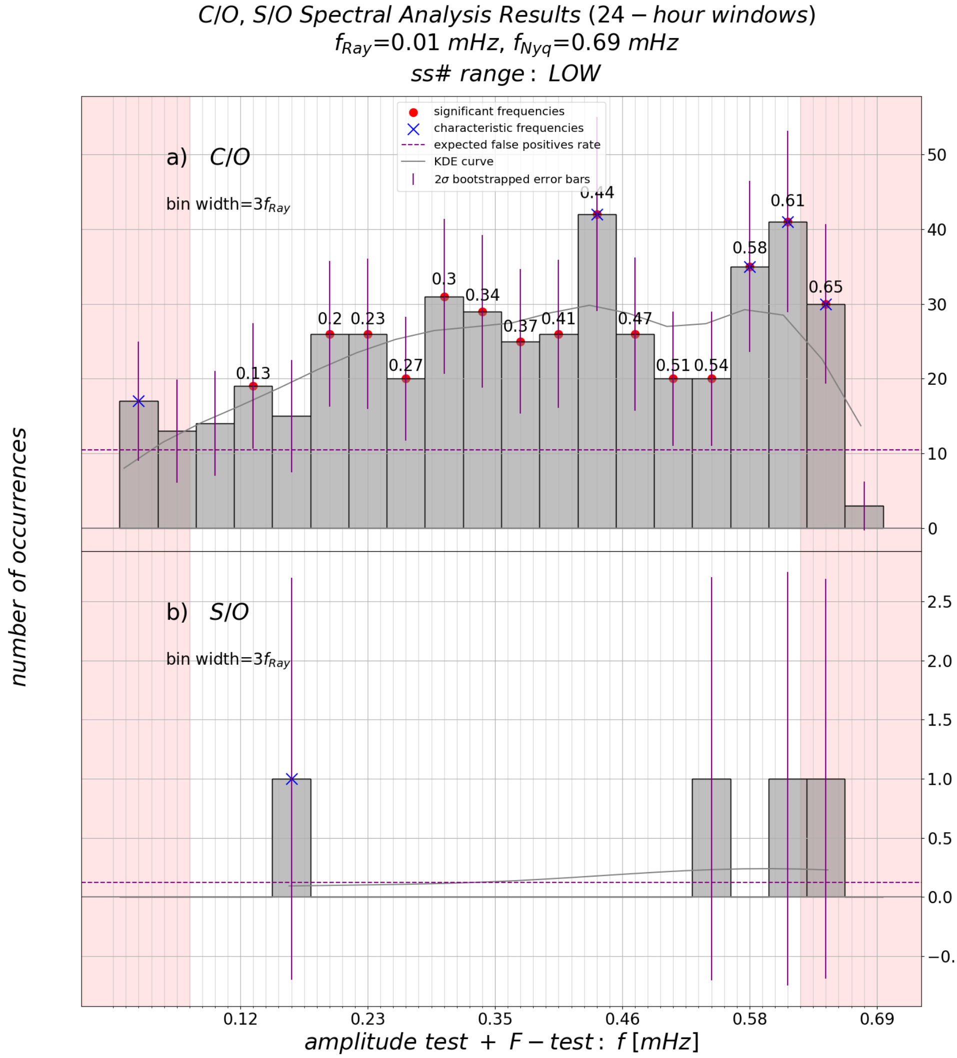

Figure A.8: C/O and S/O distributions for the LOW year grouping.

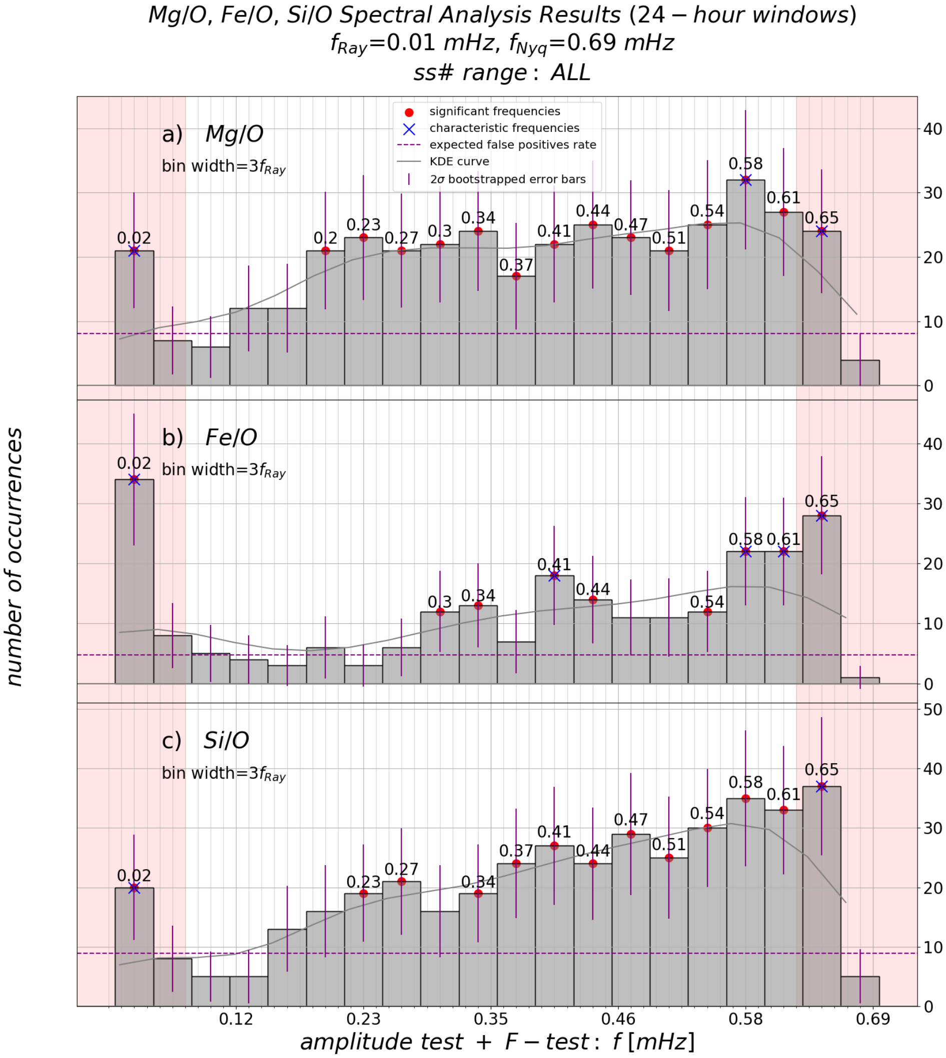

Figure A.9: Mg/O, Fe/O and Si/O distributions for the ALL year grouping.

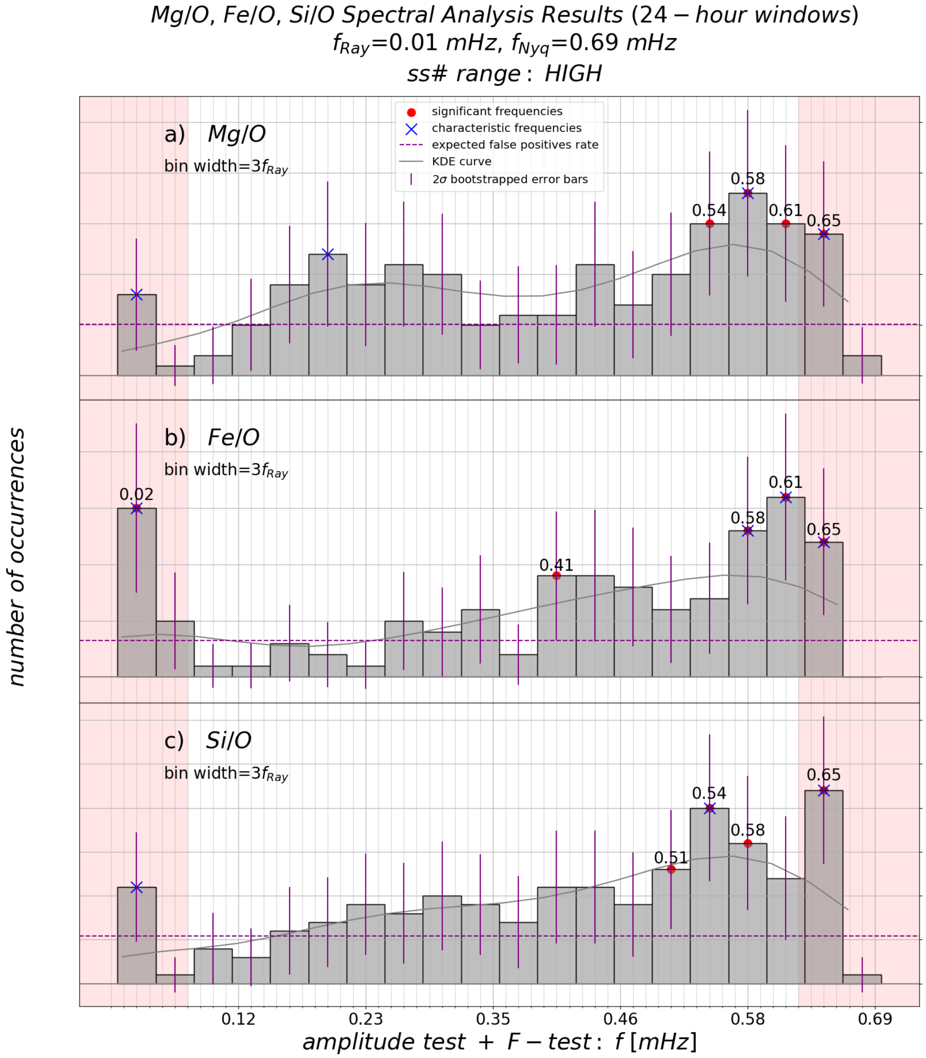

Figure A.10: Mg/O, Fe/O and Si/O distributions for the HIGH year grouping.

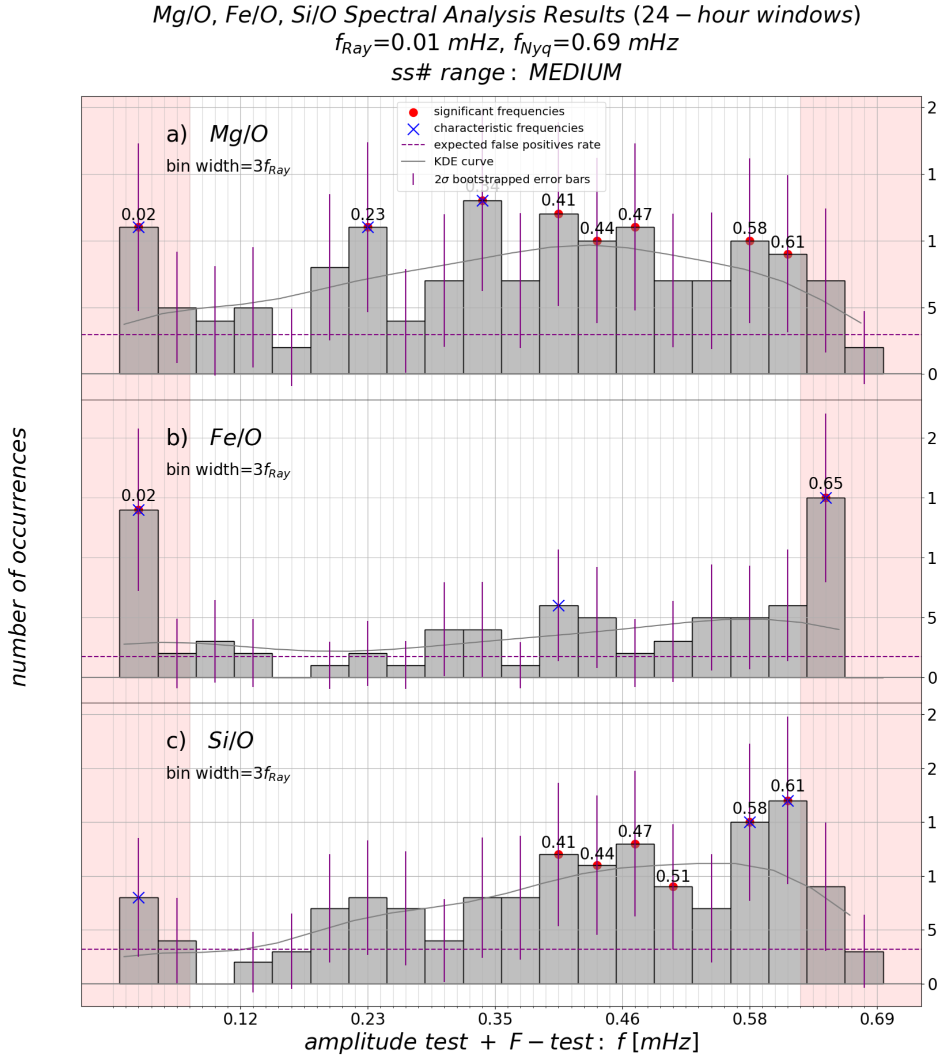

Figure A.11: Mg/O, Fe/O and Si/O distributions for the MEDIUM year grouping.

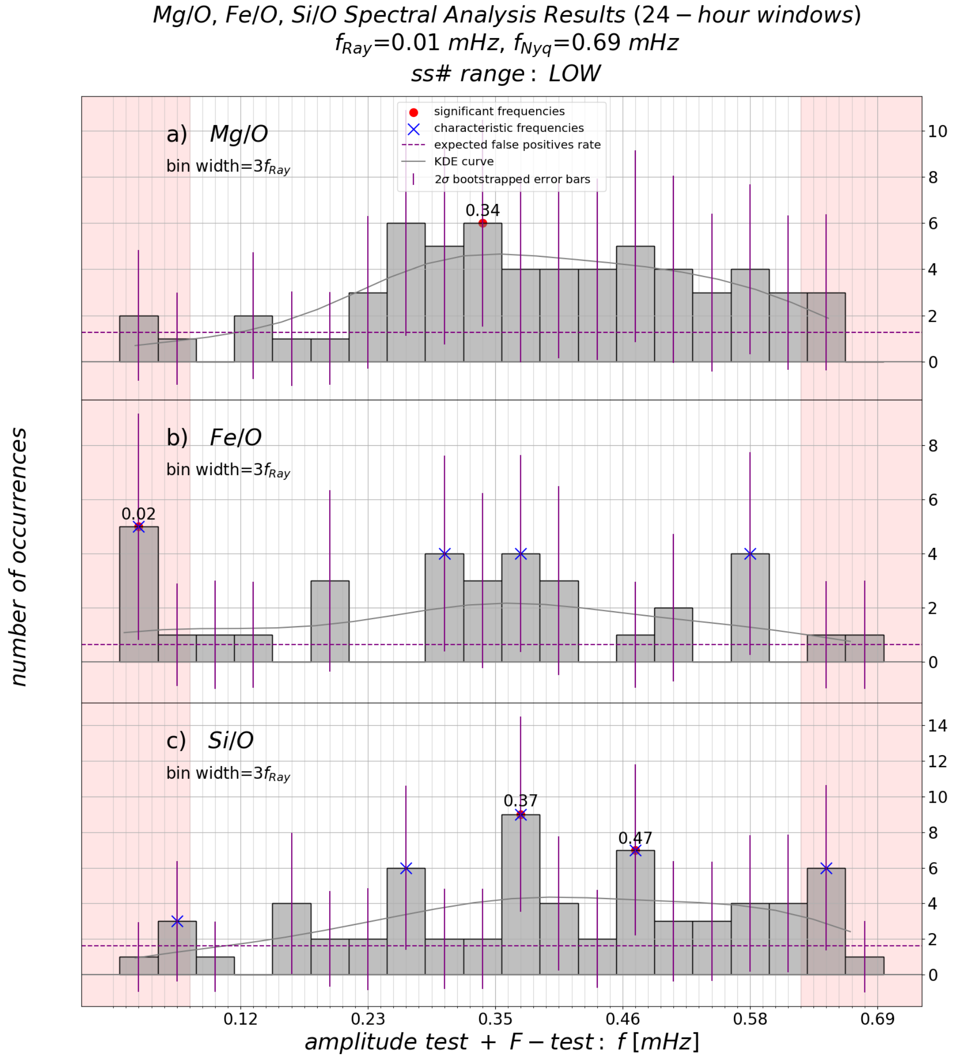

Figure A.12: Mg/O, Fe/O and Si/O distributions for the LOW year grouping.

BIBLIOGRAPHY

BIBLIOGRAPHY

Antiochos, S., Z. Mikić, V. Titov, R. Lionello, and J. Linker (2011), A model for the sources of the slow solar wind, *The Astrophysical Journal*, *731*(2), 112.

Bame, S., J. Asbridge, W. Feldman, M. Montgomery, and P. Kearney (1975), Solar wind heavy ion abundances, *Solar Physics*, *43*(2), 463–473.

Baumjohann, W., and R. A. Treumann (2012), *Basic space plasma physics*, World Scientific.

Borovsky, J. E. (2008), Flux tube texture of the solar wind: Strands of the magnetic carpet at 1 au?, *Journal of Geophysical Research: Space Physics*, *113*(A8).

Borrini, G., J. Gosling, S. Bame, W. Feldman, and J. Wilcox (1981), Solar wind helium and hydrogen structure near the heliospheric current sheet: A signal of coronal streamers at 1 au, *Journal of Geophysical Research: Space Physics*, *86*(A6), 4565–4573.

Brooks, D. H., et al. (2020), The drivers of active region outflows into the slow solar wind, *The Astrophysical Journal*, *894*(2), 144.

Crooker, N., M. Burton, G. Siscoe, S. Kahler, J. Gosling, and E. Smith (1996), Solar wind streamer belt structure, *Journal of Geophysical Research: Space Physics*, *101*(A11), 24,331–24,341.

Crooker, N., J. Gosling, and S. Kahler (2002), Reducing heliospheric magnetic flux from coronal mass ejections without disconnection, *Journal of Geophysical Research: Space Physics*, *107*(A2), SSH–3.

Crooker, N., et al. (1999), Cir morphology, turbulence, discontinuities, and energetic particles, *Corotating Interaction Regions*, pp. 179–220.

DeForest, C., W. Matthaeus, N. Viall, and S. Cranmer (2016), Fading coronal structure and the onset of turbulence in the young solar wind, *The Astrophysical Journal*, *828*(2), 66.

DeForest, C., R. A. Howard, M. Velli, N. Viall, and A. Vourlidas (2018), The highly structured outer solar corona, *The Astrophysical Journal*, *862*(1), 18.

Di Matteo, S., N. M. Viall, L. Kepko, S. Wallace, C. N. Arge, and P. MacNeice (2019), Helios Observations of Quasiperiodic Density Structures in the Slow Solar Wind at 0.3, 0.4, and 0.6 AU, *Journal of Geophysical Research: Space Physics*, *124*(2), 837–860, doi:10.1029/2018JA026182.

Di Matteo, S., N. Viall, and L. Kepko (2020), Spd_mtm: a spectral analysis tool for the spedas framework, `https://zenodo.org/record/3703168`.

Di Matteo, S., N. M. Viall, and L. Kepko (2021), Power spectral density background estimate and signal detection via the multitaper method, *Journal of Geophysical Research: Space Physics*, *126*(2), e2020JA028,748.

Di Matteo, S., U. Villante, N. Viall, L. Kepko, and S. Wallace (2022), On differentiating multiple types of ulf magnetospheric waves in response to solar wind periodic density structures, *Journal of Geophysical Research: Space Physics*, *127*(3), e2021JA030,144, doi:https://doi.org/10.1029/2021JA030144.

Dyrud, L., R. Behnke, E. Kepko, M. Sulzer, and S. Zafke (2008), Ionospheric ulf oscillations driven from above arecibo, *Geophysical research letters*, *35*(14).

Efron, B., and R. J. Tibshirani (1994), *An introduction to the bootstrap*, CRC press.

Endeve, E., Ø. Lie-Svendsen, V. H. Hansteen, and E. Leer (2005), Release of helium from closed-field regions of the sun, *The Astrophysical Journal*, *624*(1), 402.

Feldman, U. (1992), Elemental abundances in the upper solar atmosphere, *Physica Scripta*, *46*(3), 202.

Feldman, U. (1998), On the unresolved fine structures of the solar atmosphere. iii. elemental abundances consideration, *The Astrophysical Journal*, *507*(2), 974.

Feldman, U., and J. Laming (2000), Element abundances in the upper atmospheres of the sun and stars: update of observational results, *Physica Scripta*, *61*(2), 222.

Feldman, U., and K. Widing (2003), Elemental abundances in the solar upper atmosphere derived by spectroscopic means, *Space Science Reviews*, *107*(3), 665–720.

Fenrich, F., and C. Waters (2008), Phase coherence analysis of a field line resonance and solar wind oscillation, *Geophysical Research Letters*, *35*(20).

Fisk, L. (2003), Acceleration of the solar wind as a result of the reconnection of open magnetic flux with coronal loops, *Journal of Geophysical Research: Space Physics*, *108*(A4).

Geiss, J., G. Gloeckler, and R. Von Steiger (1995), Origin of the solar wind from composition data, *Space Science Reviews*, *72*(1-2), 49–60.

Gershkovich, I., S. T. Lepri, N. M. Viall, S. Di Matteo, and L. Kepko (2022), Periodic solar wind structures observed in measurements of elemental and ionic composition in situ at l1, *The Astrophysical Journal*, *933*(2), 198.

Gilly, C. R., and S. R. Cranmer (2020), The effect of solar wind expansion and nonequilibrium ionization on the broadening of coronal emission lines, *The Astrophysical Journal*, *901*(2), 150.

Gloeckler, G., T. H. Zurbuchen, and J. Geiss (2003), Implications of the observed anticorrelation between solar wind speed and coronal electron temperature, *Journal of Geophysical Research: Space Physics*, *108*(A4).

Gloeckler, G., et al. (1992), The solar wind ion composition spectrometer, *Astronomy and Astrophysics Supplement Series*, *92*, 267–289.

Gloeckler, G., et al. (1998), Investigation of the composition of solar and interstellar matter using solar wind and pickup ion measurements with swics and swims on the ace spacecraft, *The advanced composition explorer mission*, pp. 497–539.

Heber, B., and M. Potgieter (2006), Cosmic rays at high heliolatitudes, *Space Science Reviews*, *127*(1), 117–194.

Higginson, A. K., and B. J. Lynch (2018), Structured slow solar wind variability: streamer-blob flux ropes and torsional alfvén waves, *The Astrophysical Journal*, *859*(1), 6.

Hundhausen, A., H. Gilbert, and S. Bame (1968), Ionization state of the interplanetary plasma, *Journal of Geophysical Research*, *73*(17), 5485–5493.

Hundhausen, A. J., H. E. Gilbert, and S. J. Bame (1968), Ionization State of the Interplanetary Plasma, *J. Geophys. Res.*, *73*, 5485–5493.

Inglis, A., J. Ireland, and M. Dominique (2015), Quasi-periodic pulsations in solar and stellar flares: Re-evaluating their nature in the context of power-law flare fourier spectra, *The Astrophysical Journal*, *798*(2), 108.

Ipavich, F., R. Lundgren, B. Lambird, and G. Gloeckler (1978), Measurements of pulse-height defect in au si detectors for h, he, c, n, o, ne, ar, kr from 2 to 400 kev/nucleon, *Nuclear Instruments and Methods*, *154*(2), 291–294.

Ipavich, F., L. Masung, and G. Gloeckler (1982), Measurements of energy loss of h, he, c, n, o, ne, s, ar, fe, and kr passing through thin carbon foils, *Tech. rep.*, Tech. rep.

Kasper, J. C., M. L. Stevens, A. J. Lazarus, J. T. Steinberg, and K. W. Ogilvie (2007), Solar wind helium abundance as a function of speed and heliographic latitude: Variation through a solar cycle, *The Astrophysical Journal*, *660*(1), 901.

Kepko, L., and H. E. Spence (2003), Observations of discrete, global magnetospheric oscillations directly driven by solar wind density variations, *Journal of Geophysical Research: Space Physics*, *108*(A6).

Kepko, L., and N. Viall (2019), The source, significance, and magnetospheric impact of periodic density structures within stream interaction regions, *Journal of Geophysical Research: Space Physics*, *124*(10), 7722–7743.

Kepko, L., H. E. Spence, and H. Singer (2002a), Ulf waves in the solar wind as direct drivers of magnetospheric pulsations, *Geophysical Research Letters*, *29*(8), 39–1.

Kepko, L., H. E. Spence, and H. Singer (2002b), Ulf waves in the solar wind as direct drivers of magnetospheric pulsations, *Geophysical Research Letters*, *29*(8), 39–1.

Kepko, L., N. Viall, S. Antiochos, S. Lepri, J. Kasper, and M. Weberg (2016), Implications of l1 observations for slow solar wind formation by solar reconnection, *Geophysical Research Letters*, *43*(9), 4089–4097.

Kepko, L., N. M. Viall, and K. Wolfinger (2020), Inherent length scales of periodic mesoscale density structures in the solar wind over two solar cycles, *Journal of Geophysical Research: Space Physics*, *125*(8), e2020JA028,037.

Kilpua, E., H. E. Koskinen, and T. I. Pulkkinen (2017), Coronal mass ejections and their sheath regions in interplanetary space, *Living Reviews in Solar Physics*, *14*(1), 1–83.

Laming, J. M. (2015), The fip and inverse fip effects in solar and stellar coronae, *Living Reviews in Solar Physics*, *12*(1), 1–76.

Laming, J. M., et al. (2019), Element abundances: A new diagnostic for the solar wind, *The Astrophysical Journal*, *879*(2), 124.

Landi, E., R. Alexander, J. Gruesbeck, J. Gilbert, S. T. Lepri, W. Manchester, and T. H. Zurbuchen (2011), Carbon ionization stages as a diagnostic of the solar wind, *The Astrophysical Journal*, *744*(2), 100.

Landi, E., J. Gruesbeck, S. T. Lepri, T. H. Zurbuchen, and L. Fisk (2012), Charge state evolution in the solar wind. ii. plasma charge state composition in the inner corona and accelerating fast solar wind, *The Astrophysical Journal*, *761*(1), 48.

Lepri, S., E. Landi, and T. Zurbuchen (2013), Solar wind heavy ions over solar cycle 23: Ace/swics measurements, *The Astrophysical Journal*, *768*(1), 94.

Lessard, M., J. Hanna, E. Donovan, and G. Reeves (2003), Evidence for a discrete spectrum of persistent magnetospheric fluctuations below 1 mhz, *Journal of Geophysical Research: Space Physics*, *108*(A3).

Lyons, L., E. Zesta, Y. Xu, E. Sánchez, J. Samson, G. Reeves, J. Ruohoniemi, and J. Sigwarth (2002), Auroral poleward boundary intensifications and tail bursty flows: A manifestation of a large-scale ulf oscillation?, *Journal of Geophysical Research: Space Physics*, *107*(A11), SMP–9.

Mann, M. E., and J. M. Lees (1996), Robust estimation of background noise and signal detection in climatic time series, *Climatic change*, *33*(3), 409–445.

Meyer, J.-P. (1985a), The baseline composition of solar energetic particles, *The Astrophysical Journal Supplement Series*, *57*, 151–171.

Meyer, J.-P. (1985b), Solar-stellar outer atmospheres and energetic particles, and galactic cosmic rays, *The Astrophysical Journal Supplement Series*, *57*, 173–204.

Moses, J. D., et al. (2020), Global helium abundance measurements in the solar corona, *Nature Astronomy*, *4*(12), 1134–1139.

Murphy, A. K., R. M. Winslow, N. A. Schwadron, N. Lugaz, W. Yu, C. J. Farrugia, and J. T. Niehof (2020), A survey of interplanetary small flux ropes at mercury, *The Astrophysical Journal*, *894*(2), 120.

Ogilvie, K., P. Bochsler, J. Geiss, and M. Coplan (1980), Observations of the velocity distribution of solar wind ions, *Journal of Geophysical Research: Space Physics*, *85*(A11), 6069–6074.

Owen, C., et al. (2020), The solar orbiter solar wind analyser (swa) suite, *Astronomy & Astrophysics*, *642*, A16.

Papadakis, I., and A. Lawrence (1993), Improved methods for power spectrum modelling of red noise, *Monthly Notices of the Royal Astronomical Society*, *261*(3), 612–624.

Peres, G., and G. Vaiana (1990), X-ray observations, scaling laws and magnetic fields, *Memorie della Societa Astronomica Italiana*, *61*, 401–430.

Pottasch, S. R. (1963), The lower solar corona: Interpretation of the ultraviolet spectrum., *The Astrophysical Journal*, *137*, 945.

Protassov, R., D. A. Van Dyk, A. Connors, V. L. Kashyap, and A. Siemiginowska (2002), Statistics, handle with care: detecting multiple model components with the likelihood ratio test, *The Astrophysical Journal*, *571*(1), 545.

Pylaev, O., T. Zaqarashvili, A. Brazhenko, V. Melnik, A. Hanslmeier, and M. Panchenko (2017), Oscillation of solar radio emission at coronal acoustic cut-off frequency, *Astronomy & Astrophysics*, *601*, A42.

Réville, V., M. Velli, A. P. Rouillard, B. Lavraud, A. Tenerani, C. Shi, and A. Strugarek (2020), Tearing instability and periodic density perturbations in the slow solar wind, *The Astrophysical Journal Letters*, *895*(1), L20.

Richardson, I. G. (2018), Solar wind stream interaction regions throughout the heliosphere, *Living reviews in solar physics*, *15*(1), 1–95.

Richardson, I. G., and H. V. Cane (2010), Near-earth interplanetary coronal mass ejections during solar cycle 23 (1996–2009): Catalog and summary of properties, *Solar Physics*, *264*(1), 189–237.

Roberts, D. A. (2010), Demonstrations that the solar wind is not accelerated by waves or turbulence, *The Astrophysical Journal*, *711*(2), 1044.

Roberts, D. A., H. Karimabadi, T. Sipes, Y.-K. Ko, and S. Lepri (2020), Objectively determining states of the solar wind using machine learning, *The Astrophysical Journal*, *889*(2), 153.

Rouillard, A., et al. (2010), Intermittent release of transients in the slow solar wind: 1. remote sensing observations, *Journal of Geophysical Research: Space Physics*, *115*(A4).

Rouillard, A. P., et al. (2020), Relating streamer flows to density and magnetic structures at the parker solar probe, *The Astrophysical Journal Supplement Series*, *246*(2), 37.

Rouillard, A. P., et al. (2021), The solar wind, *Solar Physics and Solar Wind*, pp. 1–33.

Saba, J. (1995), Spectroscopic measurements of element abundances in the solar corona: Variations on the fip theme, *Advances in Space Research*, *15*(7), 13–22.

Sanchez-Diaz, E., A. Rouillard, B. Lavraud, E. Kilpua, and J. Davies (2019a), In situ measurements of the variable slow solar wind near sector boundaries, *The Astrophysical Journal*, *882*(1), 51.

Sanchez-Diaz, E., A. Rouillard, B. Lavraud, E. Kilpua, and J. Davies (2019b), In situ measurements of the variable slow solar wind near sector boundaries, *The Astrophysical Journal*, *882*(1), 51.

Scott, D. W. (2015), *Multivariate density estimation: theory, practice, and visualization*, John Wiley & Sons.

Shearer, P., R. von Steiger, J. M. Raines, S. T. Lepri, J. W. Thomas, J. A. Gilbert, E. Landi, and T. H. Zurbuchen (2014), The solar wind neon abundance observed with ace/swics and ulysses/swics, *The Astrophysical Journal*, *789*(1), 60.

Stakhiv, M., E. Landi, S. T. Lepri, R. Oran, and T. H. Zurbuchen (2015), On the origin of mid-latitude fast wind: Challenging the two-state solar wind paradigm, *The Astrophysical Journal*, *801*(2), 100.

Stakhiv, M., S. T. Lepri, E. Landi, P. Tracy, and T. H. Zurbuchen (2016), On solar wind origin and acceleration: Measurements from ace, *The Astrophysical Journal*, *829*(2), 117.

Stansby, D., and T. Horbury (2018), Number density structures in the inner heliosphere, *Astronomy & Astrophysics*, *613*, A62.

Suess, S., Y.-K. Ko, R. Von Steiger, and R. Moore (2009), Quiescent current sheets in the solar wind and origins of slow wind, *Journal of Geophysical Research: Space Physics*, *114*(A4).

Thomson, D. J. (1982), Spectrum estimation and harmonic analysis, *Proceedings of the IEEE*, *70*(9), 1055–1096.

Tracy, P. J. (2016), In-situ plasma analysis of ion kinetics in the solar wind and hermean magnetosphere, Ph.D. thesis, University of Michigan.

Vaughan, S. (2010), A bayesian test for periodic signals in red noise, *Monthly Notices of the Royal Astronomical Society*, *402*(1), 307–320.

Verscharen, D., K. G. Klein, and B. A. Maruca (2019), The multi-scale nature of the solar wind, *Living Reviews in Solar Physics*, *16*(1), 1–136.

Viall, M., Nicholeen, I. De Moortel, C. Downs, J. Klimchuk, S. Parenti, and F. Reale (2020), The coronal heating problem.

Viall, N., L. Kepko, and H. E. Spence (2008), Inherent length-scales of periodic solar wind number density structures, *Journal of Geophysical Research: Space Physics*, *113*(A7).

Viall, N., L. Kepko, and H. E. Spence (2009a), Relative occurrence rates and connection of discrete frequency oscillations in the solar wind density and dayside magnetosphere, *Journal of Geophysical Research: Space Physics*, *114*(A1).

Viall, N., I. De Moortel, C. Downs, J. A. Klimchuk, S. Parenti, and F. Reale (2021a), The heating of the solar corona, *Solar Physics and Solar Wind*, pp. 35–82.

Viall, N., C. Deforest, and L. Kepko (2021b), Mesoscale structure in the solar wind, *Frontiers in Astronomy and Space Sciences*, p. 139.

Viall, N. M., and J. E. Borovsky (2020), Nine outstanding questions of solar wind physics, *Journal of Geophysical Research: Space Physics*, *125*(7), e2018JA026,005.

Viall, N. M., and A. Vourlidas (2015a), Periodic density structures and the origin of the slow solar wind, *The Astrophysical Journal*, *807*(2), 176.

Viall, N. M., and A. Vourlidas (2015b), Periodic density structures and the origin of the slow solar wind, *The Astrophysical Journal*, *807*(2), 176.

Viall, N. M., H. E. Spence, and J. Kasper (2009b), Are periodic solar wind number density structures formed in the solar corona?, *Geophysical Research Letters*, *36*(23).

Viall, N. M., H. E. Spence, A. Vourlidas, and R. Howard (2010), Examining periodic solar-wind density structures observed in the secchi heliospheric imagers, *Solar Physics*, *267*(1), 175–202.

Villante, U., and P. Tiberi (2016), Occurrence and characteristics of nighttime ulf waves at low latitude: The results of a comprehensive analysis, *Journal of Geophysical Research: Space Physics*, *121*(5), 4300–4315.

Villante, U., P. Francia, and S. Lepidi (2001), Pc5 geomagnetic field fluctuations at discrete frequencies at a low latitude station, in *Annales Geophysicae*, vol. 19, pp. 321–325, Copernicus GmbH.

Villante, U., P. Francia, M. Vellante, P. Di Giuseppe, A. Nubile, and M. Piersanti (2007), Long-period oscillations at discrete frequencies: A comparative analysis of ground, magnetospheric, and interplanetary observations, *Journal of Geophysical Research: Space Physics*, *112*(A4).

Von Steiger, R., J. Geiss, and G. Gloeckler (1997), Composition of the solar wind, *Cosmic winds and the heliosphere*, p. 581.

Von Steiger, R., N. Schwadron, L. Fisk, J. Geiss, G. Gloeckler, S. Hefti, B. Wilken, R. Wimmer-Schweingruber, and T. Zurbuchen (2000), Composition of quasi-stationary solar wind flows from ulysses/solar wind ion composition spectrometer, *Journal of Geophysical Research: Space Physics*, *105*(A12), 27,217–27,238.

Weberg, M. J., T. H. Zurbuchen, and S. T. Lepri (2012), Ace/swics observations of heavy ion dropouts within the solar wind, *The Astrophysical Journal*, *760*(1), 30.

Winterhalter, D., M. Neugebauer, B. E. Goldstein, E. J. Smith, S. J. Bame, and A. Balogh (1994), Ulysses field and plasma observations of magnetic holes in the solar wind and their relation to mirror-mode structures, *Journal of Geophysical Research: Space Physics*, *99*(A12), 23,371–23,381.

Zurbuchen, T., L. Fisk, G. Gloeckler, and R. Von Steiger (2002), The solar wind composition throughout the solar cycle: A continuum of dynamic states, *Geophysical research letters*, *29*(9), 66–1.

Zurbuchen, T. H., S. Hefti, L. Fisk, G. Gloeckler, and R. v. Steiger (1999), The transition between fast and slow solar wind from composition data, *Coronal Holes and Solar Wind Acceleration*, pp. 353–356.